



*d – wave* **Superconductivity and antiferromagnetism in strongly correlated systems by a new variational approach**

Thesis submitted for the degree of  
*Doctor Philosophiæ*

**Candidate:**

Massimo Lugas

**Supervisors:**

Prof. Sandro Sorella

Dr Federico Becca

October 2007



# Contents

<b>Introduction</b>	<b>1</b>
<b>1 General Properties of High <math>T_c</math> Superconductor</b>	<b>7</b>
1.1 Introduction . . . . .	7
1.2 Experimental Results . . . . .	10
1.3 The Hubbard and the $t-J$ models . . . . .	16
1.3.1 Definitions and simple properties . . . . .	16
1.3.2 Large- $U$ limit: $t-J$ and Heisenberg model . . . . .	19
1.4 Resonating Valence Bond theories . . . . .	21
1.5 The RVB concept within the variational approach . . . . .	23
1.6 Long-range correlations: The Jastrow factor . . . . .	26
<b>2 Numerical Methods</b>	<b>31</b>
2.1 Lanczos . . . . .	32
2.2 Variational Monte Carlo . . . . .	35
2.2.1 The Metropolis algorithm for quantum problems . . . . .	37
2.3 The minimization algorithm . . . . .	39
2.4 Green's Function Monte Carlo . . . . .	45
2.4.1 Basic Principles: importance sampling . . . . .	45
2.4.2 Statistical implementation of the power method by the many walker formulation . . . . .	46
2.4.3 Fixed node and Gamma Correction . . . . .	50
2.4.4 Forward walking technique . . . . .	52
<b>3 Phase Separation in the <math>2D</math> <math>t-J</math> model</b>	<b>55</b>
3.1 Introduction . . . . .	55

3.2	Maxwell construction for Phase Separation . . . . .	58
3.3	The $t - J$ model: variational approach . . . . .	62
3.3.1	Variational wave function: RVB projected WF . . . . .	63
3.3.2	Improved variational wave function: PfaffianWF . . . . .	65
3.4	Results: Properties of the PfaffianWF and Phase Separation . . . . .	67
3.4.1	Half-filled case . . . . .	67
3.4.2	Doped region . . . . .	71
3.5	Conclusion . . . . .	80
<b>4</b>	<b>Magnetism and superconductivity in the <math>t-t'-J</math></b>	<b>83</b>
4.1	Introduction . . . . .	83
4.2	Model and Method . . . . .	86
4.3	Results . . . . .	88
4.3.1	Phase separation . . . . .	88
4.3.2	Antiferromagnetic properties . . . . .	91
4.3.3	Superconducting properties . . . . .	99
4.4	Conclusion . . . . .	105
	<b>Conclusions and perspectives</b>	<b>107</b>
<b>A</b>	<b>Pfaffian wave function</b>	<b>111</b>
A.1	Definition and properties of the Pfaffian . . . . .	111
A.2	Variational Monte Carlo implementation of the Pfaffian wave func- tion . . . . .	112
	<b>Bibliography</b>	<b>115</b>

# Introduction

Ceramic materials are expected to be insulators, certainly not superconductors, but that is just what Georg Bednorz and Alex Muller found when they studied the conductivity of a Lanthanum-Barium-Copper oxide ceramic in 1986 [1]. Its critical temperature of  $30K$  was the highest which had been measured to date, but their discovery started a surge of activity which discovered superconducting behavior as high as  $125K$ . Indeed, from that day since now, the field of high-temperature superconductivity (HTSC) evolved very rapidly, due to the improvement in the quality of the samples and in experimental techniques, providing a great amount of results. The discovery of HTSC in cuprate compounds has been one of the most fascinating issues in modern condensed matter theory for two main reasons. The first one is merely applicative, namely the possibility that new technologies may take advantage of these materials, opening new possibilities for superconducting devices with commercial applications. The second reason is the theoretical interest in the microscopic mechanism behind superconductivity, since there is a strong evidence that the pairing mechanism is completely different from the standard one, described by the old theory proposed by Bardeen, Cooper, and Schrieffer (BCS) [2]. In this respect, despite the great effort spent to understand the remarkable physical properties of these ceramic materials, a consistent microscopic theory is still lacking and this fascinating problem remains still unsolved.

The transition metal oxides represent prototype examples of materials in which the strong electron-electron and strong electron-phonon interactions lead to phases with a very poor electrical conductivity, or even an insulating behavior. For example,  $Ti_2O_3$  and  $VO_2$  are dimerized insulating materials,  $Ti_4O_7$  and  $V_4O_7$  are charged ordered insulators,  $CrO_2$  is a ferromagnetic metal,  $MnO$  and  $NiO$  are Mott insulators with antiferromagnetic order. In this context, the discovery of HTSC gives rise to a renewed interest into this class of materials, opening a new

era of unconventional superconductivity. Cuprates are layered materials with a complex perovskite chemical structure: Copper-oxide planes  $\text{CuO}_2$  are alternated with insulating blocks of rare and/or alkaline earth and Oxygen atoms. At the stoichiometric composition, cuprates are insulators with antiferromagnetic order of the spins localized on the Copper atoms. The richness of the phase diagram of these materials depends upon the fact that the electron density can be varied by substituting the rare earths with lower valence elements or by adding Oxygen atoms in the insulating blocks. It is widely accepted that the  $\text{CuO}_2$  layers play a fundamental role in determining the physical properties of these materials. Therefore, the two important ingredients that must be taken into account in any microscopic theory are the strong-coupling character of the electron-electron interaction, due to the narrow bands determined by the  $d$  orbitals of the Copper atoms, and the low dimensionality induced by the presence of the  $\text{CuO}_2$  layers.

Since the early days from the discovery of these materials, it became clear that many of their properties are unusual and a proper understanding should have required new concepts. Certainly, the more striking behavior is found in the normal (i.e., non-superconducting) regime, where many anomalies suggest that the metallic phase, above the critical temperature  $T_c$ , cannot be described by the celebrated Landau theory of Fermi liquids [3], used to describe usual metals. Within this picture, though the interaction between the electrons can be very strong and long range (i.e., through the Coulomb potential), it is possible to describe, at low energy, the whole system with weakly interacting quasi-particles, adiabatically connected to the non-interacting system. The Landau theory breaks down when there is a spontaneous symmetry breaking, e.g., if the gas of quasi-particles is unstable against pairing or magnetism. This is the basis of the mechanism to the ordinary low-temperature superconductivity: if the net interaction between quasi-particles is attractive in some angular momentum channel, it drives the system towards the superconducting state. Another interesting way to break the Landau theory, is when the residual interactions among quasi-particles are sufficiently strong that it is no longer possible to use a description of a weakly interacting gas. The anomalies detected in cuprate materials are usually interpreted as the existence of a non-Fermi liquid behavior. In particular, the linear behavior in temperature of the electrical resistivity down to  $T_c$  led many authors to suggest novel concepts for describing the metallic phase, like for instance the marginal-Fermi liquid [4].

The proximity between superconductivity and an insulating state has been considered fundamental by several authors; in this respect, spin fluctuations can be a natural generalization of phonons for the onset of electronic pairing. Moreover, the strong correlation can also induce huge density fluctuations, leading either to charge instabilities, like phase separation or charge-density waves, or to superconductivity [5].

On the other side, the superconducting state seems to be more conventional and it is associated to pairing of electrons, inducing a gap at the Fermi level. The difference with the conventional superconductors, where the gap opens isotropically along the Fermi surface, is that, for HTSC, the gap has a strong angular dependence, with a  $d_{x^2-y^2}$  symmetry. However, the existence of a *pseudogap* in the single-particle excitation spectrum also in the metallic phase above  $T_c$  clearly marks a spectacular difference with standard BCS theory and could indicate the predominant role of phase fluctuations of the order parameter [6]. By contrast, one of the great advantage of the low-temperature superconductors is that the critical temperature is mainly determined by the amplitude fluctuations of the order parameter, and the mean-field approach of the BCS theory gives an excellent description also very close to the transition.

The theoretical approach is complicated by a large number of effects (like for instance, strong electronic correlation, antiferromagnetism, electron-phonon coupling, polaronic effects, and disorder) that cooperate in determining the physics of these materials. A full understanding of all the experimental phenomenology is practically impossible and, as a consequence, it is extremely important to study simple theoretical models, that are able to reproduce the main features of cuprate materials and especially superconductivity. In this respect, assuming that the strong correlation is the dominant ingredient, the so-called  $t-J$  model in two spatial dimensions can represent a very good starting point. Mean-field solutions are often misleading due to important quantum fluctuations, which are far from being negligible, while perturbative calculations are inadequate, being the relevant physics related to the strong-coupling regime. Therefore, in the last years, correlated electrons have been deeply and successfully studied by numerical approaches. These methods allow one to evaluate ground-state properties of finite-size systems, without assuming a small electron-electron correlation. As an example, Lanczos method, though in two dimensions is restricted to extremely

small cluster sizes, allows to compute exact static and dynamical properties of a model Hamiltonian. The restriction to fairly small clusters is due to the huge dimension of the Hilbert space, that increases exponentially with the size of the lattice. In order to overcome this problem, alternative approaches are necessary, like for instance the ones based upon statistical approaches, i.e., Monte Carlo techniques. In this thesis, we have used variational Monte Carlo methods, which allow us to study ground-state properties of strongly correlated systems (in our case, the  $t-J$  model), making also possible to afford calculations on large sizes and extrapolate very accurate thermodynamic properties.

The art of the variational approach is based on the physical intuition and the ability to find a trial wave function for the ground state. Then all the physical properties, like the energy and the correlation functions, can be calculated by stochastic methods, based upon Markov chains. Moreover, the stability of the variational state can be checked by using more advanced Monte Carlo techniques, that can iteratively project out the high-energy components from the trial wave function, eventually filtering out the ground state.

In this thesis, we consider an improved variational wave function that contains both the antiferromagnetic and the d-wave superconducting order parameters, by considering also a long-range spin-spin Jastrow factor in order to reproduce the correct behavior of the spin fluctuations at small momenta. In this way, we obtain the most accurate state available so far for describing the  $t-J$  model at low doping. Using this wave function, the quantum Monte Carlo simulations clarify several problems raised in this introduction: among them, the role of the phase separation in the physics of the HTSC and the relation between antiferromagnetism and superconductivity. We mainly focus our attention on the physically relevant region  $J/t \sim 0.4$  and find that, contrary to all previously reported but much less accurate variational ansatz, this state is stable against phase separation for small hole doping. Moreover, by performing projection Monte Carlo methods based on the fixed-node approach, we obtain a clear evidence that the  $t-J$  model does not phase separate for  $J/t \lesssim 0.7$  and the compressibility remains finite close to the antiferromagnetic insulating state.

After that, we consider the effect of a next-nearest-neighbor hopping in the antiferromagnetic and superconducting properties. We present a systematic study of the phase diagram of the  $t-t'-J$  model by using the projection Monte Carlo

technique, implemented within the fixed-node approximation. This enables us to study the interplay between magnetism and pairing, comparing the Monte Carlo results with the ones obtained by the simple variational approach. The pair-pair correlations have been accurately calculated for the first time within Green's function Monte Carlo by using the so-called forward walking technique, that allows us to consider true expectation values over an approximate ground state. In the case of  $t' = 0$ , there is a large region with a coexistence of superconductivity and antiferromagnetism, that survives up to  $\delta_c \sim 0.1$  for  $J/t = 0.2$  and  $\delta_c \sim 0.15$  for  $J/t = 0.4$ . The presence of a finite  $t'/t < 0$  induces a strong suppression of both magnetic (with  $\delta_c \lesssim 0.03$ , for  $J/t = 0.2$  and  $t'/t = -0.2$ ) and pairing correlations. In particular, the latter ones are depressed both in the low-doping regime and around  $\delta \sim 0.25$ , where strong size effects are present.

## Overview

The thesis is organized as follows:

- In Chapter 1, we introduce the physics of the HTSC, starting with an historical overview of the problem and describing some experimental results that characterize these materials. Subsequently, we introduce the  $t-J$  model, which allows a microscopic description of the HTSC and we introduce the Resonating Valence Bond (RVB) wave function.
- In Chapter 2, we will describe the numerical techniques used for obtaining the results of our thesis. We start from the Lanczos method, that enable us to obtain exact results for small cluster size and then we enter in the topic of the quantum Monte Carlo technique. We describe the variational Monte Carlo method, the optimization algorithm and we will introduce the Green's function Monte Carlo and fixed-node approximation, that improve the variational results.
- In Chapter 3, we will introduce our new variational wave function which generalizes the RVB state we show our results on the charge fluctuations (phase separation problem) for the two-dimensional  $t-J$  model. The main results of this chapter has been published in Physical Review B [7].
- In Chapter 4, we will study the magnetic and superconducting properties of the two-dimensional  $t-J$  and  $t-t'-J$  model, trying to understand the role of the next-nearest-neighbor hopping term on the magnetic and superconducting phases. We will show a phase diagram of the magnetic and superconducting correlations, which qualitatively reproduce the actual phase diagram of HTSC and gives some indication on the origin of the electronic pairing. The main results of this chapter were submitted to Physical Review B [8].

# Chapter 1

## General Properties of High $T_c$ Superconductor

### 1.1 Introduction

Twenty years ago, Bednorz and Muller [1] discovered high-temperature superconductivity (HTSC) in Sr-doped  $\text{La}_2\text{CuO}_4$ , a class of transition-metal oxides that shows a wide range of phase transitions. Subsequently, HTSC has been found in a large variety of cuprate compounds, also stimulating synthesis of new materials, with unconventional electronic properties. Even if several physical details, such as the critical temperature  $T_c$ , are not universal, there are properties which are common to all these materials. In this respect, important examples are the crystal structure, the presence of strong electron-electron interactions, and the closeness to an insulating phase. Moreover, it turns out that the metallic phase cannot be described in general by the usual Landau theory of the Fermi liquids, and shows many anomalous properties, like a linear temperature behavior of the resistivity down to  $T_c$  [9].

The High  $T_c$  compounds have a layered structure made up of one or more  $\text{CuO}_2$  planes per unit cell; the Copper atoms lie inside a cage of Oxygen atoms, forming octahedra, see Fig. 1.1. These planes are separated by blocks containing for instance rare-earth elements or Oxygen atoms. The presence of  $\text{CuO}_2$  layers in all HTSC compounds led to the belief that a lot of the important physics is contained in these two-dimensional structures. This is also supported by the fact

that the Cu–O in-plane bond is more than three times smaller than the distance between planes, so that, at first approximation, the interlayer coupling can be neglected. Therefore, it is usually assumed that all the important physics is governed by processes occurring in the  $\text{CuO}_2$  planes, while the other blocks, called charge reservoirs, are almost inert and simply provide charge carriers [10, 11].

One of the most celebrated examples of HTSC materials is found by doping  $\text{La}_2\text{CuO}_4$ , i.e., by partially substituting La by Sr, leading to  $\text{La}_{2-x}\text{Sr}_x\text{CuO}_4$ . For  $x = 0$ , there is an odd number of electrons per unit cell and, therefore, from general principles, a metallic behavior should be expected. In fact, band structure calculations (based on the so-called Local-Density Approximation) predict that the Fermi level lies within a band mainly constructed from the  $d_{x^2-y^2}$  orbital of Copper atoms. On the contrary,  $\text{La}_2\text{CuO}_4$  is a Mott insulator, with antiferromagnetic order below the Neel temperature  $T_N \approx 300\text{K}$ . This is one of the most spectacular example in which the single-electron picture fails and the electron-electron correlation is important to determine the physical properties of the system. The fact is that  $3d$ -orbital wave functions are confined more closely to the nucleus than  $s$  or  $p$  states with comparable energy, implying a small overlap between neighboring atomic sites and a tiny bandwidth. On the other hand, the Coulomb repulsion between electrons occupying the same orbital with opposite spins (the so-called Hubbard  $U$ ) can be very large, even when including screening effects. These two aspects determine a competition between itineracy and localization, that can lead to an insulating behavior when a metal should be expected. The antiferromagnetic properties also arise from the strong effective Coulomb interaction, that generates a super-exchange coupling between Copper atoms [12].

The antiferromagnetic order of the undoped compound is suppressed by doping and eventually superconductivity, with a high-transition temperature, emerges. The behavior of  $T_c$  with doping exhibits a characteristic dome-like shape. For instance,  $\text{La}_{2-x}\text{Sr}_x\text{CuO}_4$  undergoes a transition from an antiferromagnetic insulator to a paramagnetic metal at  $x \approx 0.03$  and the superconducting transition temperature has a maximum of about  $40\text{K}$  around  $x_m \sim 0.15$ , called optimal doping. Above the superconducting transition temperature, the metallic phase shows unusual properties in the underdoped region  $x < x_m$ , whereas it becomes more Fermi-liquid-like when moving towards the overdoped region, i.e.,  $x > x_m$ . It should be mentioned that there are two ways to inject charge carriers: either re-

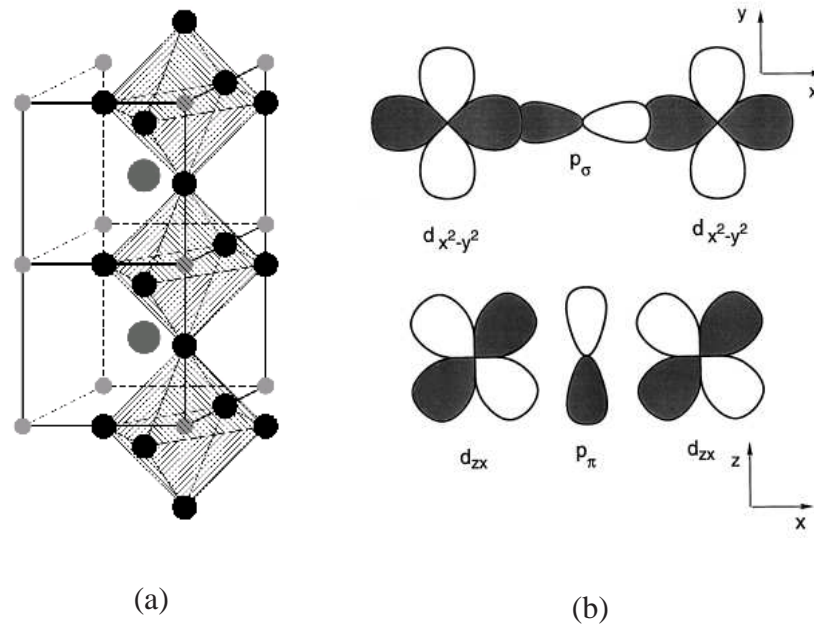


Figure 1.1: (a) Typical cubic perovskite structure of transition-metal compounds. Transition-metal atoms are the small grey spheres, at the center of Oxygen octahedra (dark spheres). (b) Different arrangements of  $d$  (on top  $e_g$  orbitals, at the bottom  $t_{2g}$  orbitals) and  $p$  orbitals in transition-metal oxides.

moving electrons from the  $\text{CuO}_2$  planes (like for instance substituting La with Sr in  $\text{La}_2\text{CuO}_4$ ) or adding electrons to the planes (like or inserting further Oxygen atoms in  $\text{La}_2\text{CuO}_4$  or substituting Nd with Ce in  $\text{Nd}_2\text{CuO}_4$  [13]). In Fig. 1.2, we show the phase diagrams of two compounds, prototypes for the hole-doped and electron-doped material. While electron and hole doped HTSC share many common features, they do exhibit significant differences, like for instance the stability of the antiferromagnetic phase upon doping.

There is enough evidence suggesting that superconductivity in cuprate materials is fundamentally different from the one described by the standard BCS theory, valid for alkaline metals. For instance, in HTSC the isotope effect is absent (or very small); this fact indicates that probably the actual mechanism leading to Cooper pairs is different from the standard electron-phonon one. Moreover, in a BCS superconductor the gap has s-wave symmetry, i.e., isotropic in the momentum space, while there is now a wide consensus that in high- $T_c$  superconductors

pairing occurs with a  $d_{x^2-y^2}$  symmetry [14–18]. These facts, together with the proximity of a magnetic phase, induced many authors to search for alternative mechanisms for superconductivity, not based on the electron-phonon coupling.

All the unusual observations stimulated an enormous amount of experiments, as well as theoretical works on HTSC, which gave important insight into these fascinating compounds. In addition, new sophisticated analytical and numerical techniques have been developed and now they provide us with a partial understanding of correlation effects in electronic systems.

## 1.2 Experimental Results

The discovery of the HTSC stimulated the development of several experimental techniques. Here, we expose some key experimental facts concerning these materials, without entering in the details that are available in literature [17, 19, 20].

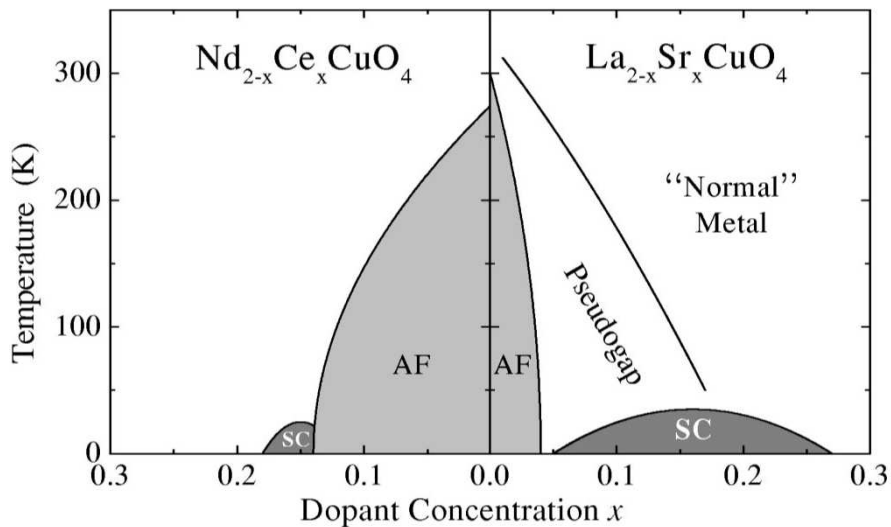


Figure 1.2: Schematic phase diagram for hole-doped (right side) and electron-doped (left side) high-temperature superconductors.

In general, the attention is restricted to the hole-doped compounds, partly because they are better characterized and more extensively investigated, but also

because, in the underdoped regime, the hole-doped HTSC show the very interesting *pseudogap phase*, in which the system does not have a superconducting long-range order, but still presents a large and anisotropic gap in the excitation spectrum [18, 21–23]. The onset temperature of the pseudogap decreases linearly with doping and disappears in the overdoped regime. The origin of the pseudogap is one of the most controversial topics in the HTSC field. Moreover, its relationship with other important features, such as the presence of a Nernst phase [24, 25], charge inhomogeneities [26], the neutron scattering resonance [27], or disorder [28] is still unclear. In the following, we will briefly describe some results from angle resolved photo-emission spectroscopy (ARPES), scanning tunneling microscopy (STM) and nuclear magnetic resonance (NMR): these techniques have seen significant advances in recent years and provided us with important insight into the nature of the low-energy excitations in the metallic and superconducting samples.

By measuring the energy and momentum of photo-electrons, ARPES techniques provide useful information about the single particle spectral function  $A(k, \omega)$ , that is related to the electron Green's function by  $A(k, \omega) = -\frac{1}{\pi} \text{Im}G(k, \omega)$ . As a consequence, it is possible to obtain the Fermi surface and the gap of the system under study. We will briefly summarize some key results from ARPES that any theory of HTSC has to address. For an extensive discussion and a general review about experimental details one can see, for instance, the papers by Damascelli and collaborators [19] and by Campuzano and collaborators [29].

Fig. 1.3 shows a schematic picture of the Fermi surface of cuprates in the first quadrant of the first Brillouin zone. It can be obtained by ARPES scans along different angles  $\phi$  by looking at the minimum energy of the photo-electron along a given direction in momentum space. A typical energy distribution curve, that is given by the photo-emission intensity as a function of energy at fixed momentum, is shown in Fig. 1.4. The figure shows the photo-emission intensity at the  $(\pi, 0)$  point of a photo-electron in the superconducting and in the normal state. Below  $T_c$ , we observe the characteristic peak-dip-hump structure, the peak being associated with a coherent quasiparticle; on the other hand, above  $T_c$ , coherence is lost and the sharp peak disappears.

Immediately after the discovery of HTSC, it was unclear if the pairing symmetry were isotropic (i.e., s-wave) as in conventional phonon-mediated super-

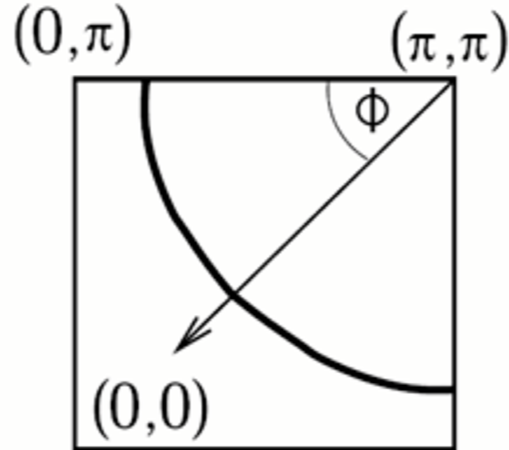


Figure 1.3: A schematic picture of the two-dimensional Fermi surface (thick black line) of cuprates in the first quadrant of the first Brillouin zone. The lattice constant  $a$  is set to unity and  $\phi$  indicates the Fermi surface angle.

conductor, or anisotropic. But later experiments have consistently confirmed an anisotropic gap with d-wave symmetry [14, 15]. The angular dependence of the gap function can be clearly seen in ARPES measurements on HTSC, which accurately determine the superconducting gap  $\Delta_k$  along the Fermi surface of the normal state. As shown in Fig. 1.5, the gap vanishes for  $\phi = 45^\circ$  (nodal point) while it is maximum at  $\phi = 0^\circ, 90^\circ$  (antinodal points). There are, however, other experimental data that support s-wave (or even more complicated types of symmetries, like d+s, d+is) [30]. Very recently, Muller and collaborators gave some indication in favor of the existence of two gaps in  $\text{La}_{1.83}\text{Sr}_{0.17}\text{CuO}_4$ : a large gap with d-wave symmetry and a smaller one with s-wave symmetry [31].

Unlike conventional superconductor, HTSC exhibits a strong deviation from the BCS-ratio of  $2\Delta/k_B T_c \approx 4.3$  for the superconductor with a d-wave gap function [where  $\Delta$  is the gap at  $k = (\pi, 0)$ ]. Moreover, in HTSC, this ratio is strongly doping dependent and becomes quite large for underdoped samples. Indeed, whereas the critical temperature decreases approaching the Mott insulator, the magnitude of the superconducting gap increases. An additional information that can be extracted from ARPES data is the doping dependence of the spectral

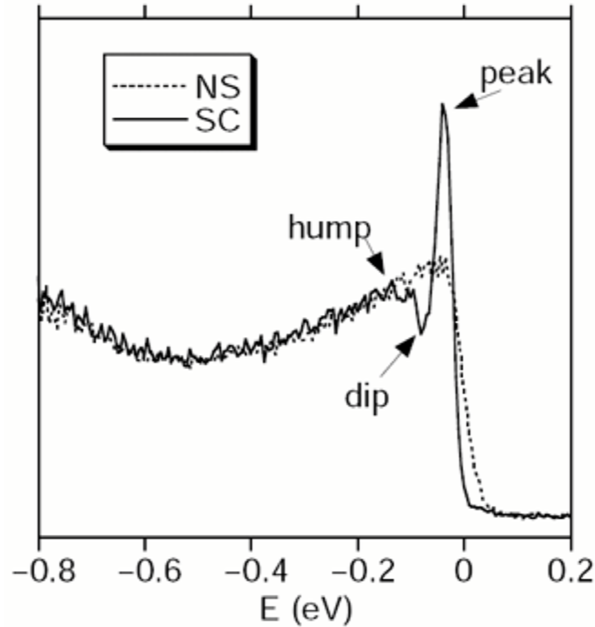


Figure 1.4: Energy distribution curve at fixed momentum  $k = (\pi, 0)$  for an overdoped  $\text{Bi}_2\text{Sr}_2\text{CaCu}_2\text{O}_{8+\delta}$  sample in the normal state (NS) and superconducting state (SC).

weight of the coherent quasiparticle peak, that strongly decreases with decreasing doping and finally vanishes close to the Mott insulator [32, 33].

Probably, the most interesting feature seen in ARPES experiments is the shrinking of the Fermi surface above  $T_c$  in the underdoped regime, i.e., the opening at  $T^*$  of a pseudogap in the normal phase. Indeed, by decreasing the temperature, more and more states around the antinodal region become gapped and the Fermi surface becomes smaller and smaller with continuity. Instead of a closed Fermi surface, the system exhibits Fermi arcs [22, 23] that finally collapses to single nodal Fermi points at  $T = T_c$ , see Fig. 1.6. Interestingly, the opening of the pseudogap at  $T^*$  seems to be related to the magnitude of the superconducting gap  $\Delta$ . For a detailed discussion on this and related ARPES observations, one can see for instance reviews in the literature [19, 29]. This is a striking difference with the conventional BCS superconductors. While, in the overdoped regime, the HTSC materials behave as a reasonably conventional metal with a large Fermi surface,

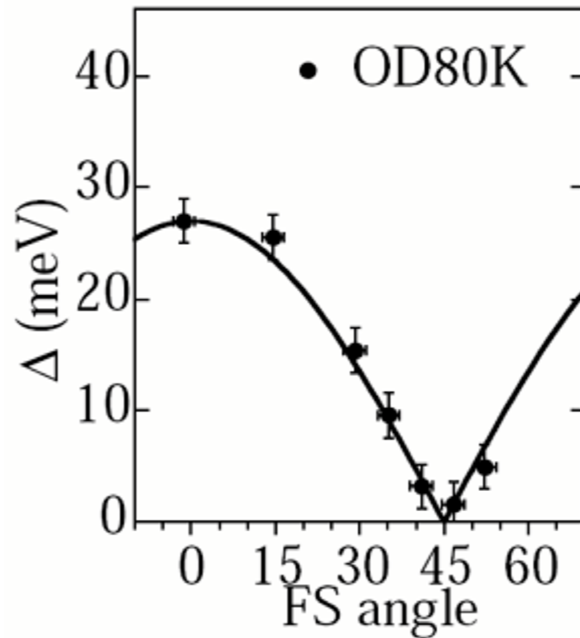


Figure 1.5: Momentum dependence of the spectral gap  $\Delta$  along the Fermi surface in the superconducting state of an overdoped  $\text{Bi}_2\text{Sr}_2\text{CaCu}_2\text{O}_{8+\delta}$  sample from ARPES. The black line is a fit to the data. For a definition of the angle  $\phi$  see Fig. 1.3.

the underdoped regime is highly anomalous, having the disconnected Fermi arcs described above. A fundamental question, is to understand if there is a phase transition that could change the topology of the Fermi surface. It should be mentioned that, very recently, measurements of quantum oscillations in the electrical resistance revealed the possibility that the Fermi arcs are just portions of small pockets around  $(\pi/2, \pi/2)$ . The fact that ARPES only see a segment of these hole pockets could be due to the fact that the other portion has a very low intensity, not measurable at present [34].

A complementary experimental technique to ARPES is given by STM, that is a momentum integrated probe. Its ability to measure the local density of occupied as well as unoccupied states with an high-energy resolution gives valuable insight into the properties of HTSC. A key advantage of STM is the possibility to obtain spatial information: STM experiments allow for the investigation of local

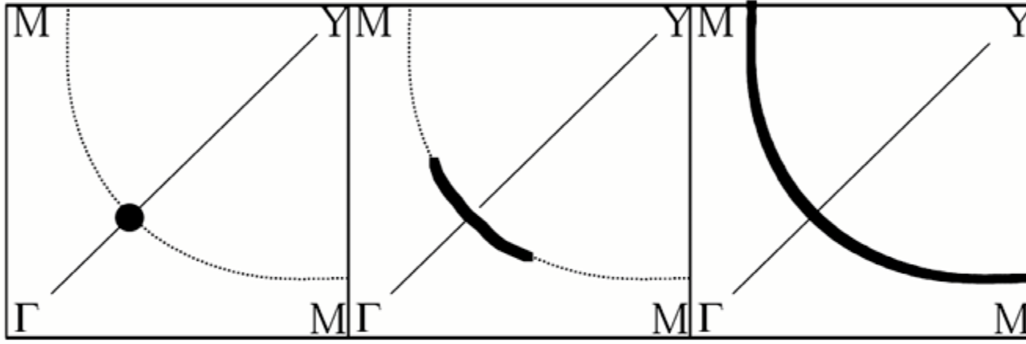


Figure 1.6: Schematic illustration of the temperature evolution of the Fermi surface in underdoped cuprates as observed by ARPES. The  $d$  - wave node below  $T_c$  (left panel) becomes a gapless arc above  $T_c$  (middle panel) which expands with increasing  $T$  to form the full Fermi surface at  $T^*$  (right panel).

electronic structure around impurities [35–37] and around vortex cores [38–40] in the superconducting state. Two interesting features recently reported by STM are the possibility to have a checkerboard-like charge-density wave [41, 42] and the existence of spatial variation in the superconducting gap [43]. The origin of these observations is currently being debated intensely.

Several authors [44, 45] suggested that superconductivity could be connected with the tendency toward charge segregation of electrons and holes in the  $\text{CuO}_2$  layers. For instance, phase separation was observed in the Oxygen doped compounds  $\text{La}_2\text{CuO}_{4+\delta}$ , by using Neutron Powder diffraction [46] and NMR [47]. The experimental data obtained with these two techniques showed that the system is separated in an Oxygen rich and in an Oxygen poor regions. Instead, no evidence of phase separation has been found in other hole-doped compounds, like  $\text{La}_{2-x}\text{Sr}_x\text{CuO}_4$ .

Through Neutron scattering and NMR experiments it is possible to carefully analyze the change of the magnetic properties of the HTSC materials upon doping. Measurements of the Neutron scattering cross section provide information on the spin-spin structure factor. As a consequence of the antiferromagnetic long-range order, the undoped compound shows a sharp peak in the spin-spin structure factor at the wave vector,  $Q = (\pi, \pi)$ . In the case of  $\text{La}_{2-x}\text{Sr}_x\text{CuO}_4$ , this peak broadens and disappears at  $x > 0.05$ , where incommensurate spin fluctuations

arise at  $(\pi, \pi \pm 2\epsilon\pi)$  and  $(\pi \pm 2\epsilon\pi, \pi)$  [48]. The dependence of the incommensurability  $\epsilon$  with doping is linear for  $0.05 < \delta < 0.12$  and then saturates [48]. A striking feature is that the angular coefficient of the linear relation between the incommensurability and the doping fraction is exactly  $2\pi$ . X-ray diffraction measurements [49] has shown that similar incommensurate peaks also occur in the charge structure factor but close to the  $\Gamma = (0, 0)$  point, with an incommensurability which is twice the spin structure one. This behavior has been explained by a domain walls ordering of holes in the  $\text{CuO}_2$  layers. Half-filled hole stripes separate antiferromagnetic region, which are correlated with a  $\pi$  shift across a domain wall. The modulation connected with the charge is then at small momenta, close to the  $\Gamma$  point, while the spin-spin structure factor presents a spin density wave at incommensurate momenta close to the antiferromagnetic wave vector [50].

### 1.3 The Hubbard and the $t-J$ models

Since the earliest days of the HTSC era, it was realized that any theoretical model willing to describe superconductivity had necessarily to include strong electronic correlation. In this regard, the Hubbard model is the simplest example of a microscopic Hamiltonian that takes into account the electron interaction and its competition with the kinetic energy. It was independently introduced by Hubbard [51], Gutzwiller [52] and Kanamori [53] in 1963 in order to understand magnetism in transition metals. In the recent past, the Hubbard model, together with its strong-coupling limit, the so-called  $t-J$  model, was widely considered in order to clarify the possibility that superconductivity arises from strong electronic correlation.

#### 1.3.1 Definitions and simple properties

The one-band Hubbard Hamiltonian is defined on a lattice of  $L$  sites and can be written as:

$$H = -t \sum_{\langle i,j \rangle, \sigma} (c_{i\sigma}^\dagger c_{j\sigma} + h.c.) + U \sum_j n_{j\uparrow} n_{j\downarrow} \quad , \quad (1.1)$$

where  $\langle i, j \rangle$  denotes nearest-neighboring sites  $i$  and  $j$ ,  $c_{i\sigma}^\dagger$  ( $c_{i\sigma}$ ) creates (destroys) an electron with spin  $\sigma$  on site  $i$  and  $n_{j\sigma} = c_{j\sigma}^\dagger c_{j\sigma}$  is the occupation number operator. The term *one-band* refers to the assumption that only one Wannier state

per site is considered. This approximation is valid when the Fermi energy lies within a single conduction band, implying an irrelevant contribution of the other bands. Since only one atomic level per atom is considered, each lattice site can appear in four different quantum states:

$$\begin{aligned} &|0\rangle_j \text{ empty site,} \\ &|\uparrow\rangle_j = c_{j\uparrow}^\dagger |0\rangle \text{ site } j \text{ occupied by an } \uparrow \text{ electron,} \\ &|\downarrow\rangle_j = c_{j\downarrow}^\dagger |0\rangle \text{ site } j \text{ occupied by a } \downarrow \text{ electron,} \\ &|\uparrow\downarrow\rangle_j = c_{j\uparrow}^\dagger c_{j\downarrow}^\dagger |0\rangle \text{ site } j \text{ doubly occupied.} \end{aligned}$$

The first term in Eq. (1.1) expresses the kinetic part  $\mathcal{K}$ , which *delocalizes* the  $N$  electrons in the lattice. The hopping parameter  $t$  controls the bandwidth of the system and depends on the overlap between neighboring orbitals:

$$t_{i,j} = \int dr \phi_i^*(r) \left( \frac{\nabla^2}{2m} + V_{ion} \right) \phi_j(r) , \quad (1.2)$$

where  $\phi_j(r)$  is a Wannier orbital centered on site  $j$  and  $V_{ion}$  is the potential created by the positive ions forming the lattice. In translationally invariant systems,  $t_{ij}$  depends only upon the distance among the sites  $i$  and  $j$  and in Eq. (1.1) we have considered only a nearest-neighbor hopping  $t$ . The kinetic term  $\mathcal{K}$  can be diagonalized in a single-particle basis of Bloch states:

$$\mathcal{K} = \sum_{k,\sigma} \epsilon_k c_{k\sigma}^\dagger c_{k\sigma} \quad \epsilon_k = -2t \sum_{j=1}^d \cos(k_j) , \quad (1.3)$$

where  $c_{k,\sigma}^\dagger = \frac{1}{\sqrt{L}} \sum_j e^{ikj} c_{j\sigma}^\dagger$  and a simple  $d$ -dimensional cubic lattice has been considered.

The Hubbard  $U$  comes from the Coulomb repulsion of two electrons sharing the same orbital:

$$U = \int dr_1 dr_2 |\phi_j(r_1)|^2 \frac{e^2}{|r_1 - r_2|} |\phi_j(r_2)|^2 . \quad (1.4)$$

Of course, this term is only an approximation of the true Coulomb interaction, since it completely neglects the long-range components which are present in realistic systems. Nevertheless, in spite of its simplicity, the Hubbard model is far from being trivial and the exact solution is known only in the one-dimensional case [54]. Its phase diagram, depends on the electron density  $n = N/L$  and the

ratio  $U/t$ . Moreover, different lattice geometries and the addition of longer-range hopping terms could influence the resulting phase diagram.

The form of the Hubbard Hamiltonian given in Eq. (1.1) immediately suggests that its phase space comes out from two competing tendencies: from one side, the hopping term tends to delocalize the electrons in the crystal and, from the other side, the interaction term encourages electrons to occupy different sites, otherwise the system must pay an energy cost  $U$  per each doubly occupied site. Whenever the electron density is away from half filling, i.e.,  $n \neq 1$ , the number of holes or doubly occupied sites is different from zero and charge fluctuations are possible without a further energy cost. In this case, the ground state of the system is predicted to be metallic for any value of  $U/t$ , unless for special charge-density wave instabilities at particular wave vectors, that could happen for small dopings and weak correlations [55]. Moreover, the possible occurrence of superconductivity in the Hubbard model for  $n \neq 1$  has been widely investigated and there are now important evidences that superconductivity emerges at finite doping [56]. Instead, at half filling (i.e., for  $n = 1$ ), there are no extra holes (or double occupancies) and each site is (in average) singly occupied. The two tendencies of delocalizing and localizing the system are strictly dependent on the value of  $U/t$ , according to the two limiting cases:

- for  $U/t = 0$  (*band limit*) the system is a non-interacting metal;
- for  $t/U = 0$  (*atomic limit*) the system is an insulator with no charge fluctuations.

The presence of different phases, for the two limiting values of  $U/t$ , suggests the existence of a phase transition, which is purely driven by the correlation: the *Mott metal-insulator transition*. It should be stressed that the Mott transition is often accompanied by a magnetic ordering of the insulating phase. For instance, the ground state of the Hubbard model with nearest-neighbor hopping on the square lattice is insulating for any interaction  $U/t$ : at weak coupling, because of the so-called nesting property of the Fermi surface, that leads to a divergent susceptibility as soon as the interaction  $U$  is turned on; at strong coupling, because an effective super-exchange interaction is generated at the order  $t^2/U$ , giving rise to the anti-ferromagnetic long-range order. These two limits are adiabatically connected, implying that the ground state is always insulating with gapless spin excitations. In

the following, we will show the canonical transformation that allows one to derive an effective spin Hamiltonian, which describes the Hubbard model at strong coupling (i.e.,  $U/t \gg 1$ ) and acts on the Hilbert space without double occupancies. This defines the so-called  $t$ - $J$  model that is very useful to study superconducting and magnetic properties of correlated systems, since it focuses on low-energy properties, without considering high-energy processes of the order  $U/t$ . In particular, the pairing-pairing correlations could be very small and it would be very difficult to detect the superconducting signal within the original Hubbard model, containing huge charge fluctuations.

### 1.3.2 Large- $U$ limit: $t$ - $J$ and Heisenberg model

The  $t$ - $J$  Hamiltonian was pioneered by Anderson [57] and rederived by Zhang and Rice [58], starting from the three-band Hubbard model, in order to describe the low-energy properties of the  $\text{CuO}_2$  planes of HTSC. The general procedure for the derivation consists in looking for a Schrieffer-Wolff canonical transformation [59], which allows one to achieve a separation between low- and high-energy subspaces. In the Hubbard model at large  $U/t$ , these subspaces are characterized by a different number of double occupancies  $n_d$ . The operator that mixes these different sectors of the Hilbert space corresponds to the kinetic part (1.3), which can be rewritten as:

$$\mathcal{K} = H_t^+ + H_t^- + H_t^0, \quad (1.5)$$

where  $H_t^+$  ( $H_t^-$ ) increases (decreases) the number of doubly occupied sites by one and  $H_t^0$  corresponds to the hopping processes which do not change the number of double occupancies. The effective Hamiltonian is obtained through the rotation:

$$H_{eff} = e^{iS} H e^{-iS} = H + i[S, H] + \frac{i^2}{2}[S, [S, H]] + \dots, \quad (1.6)$$

where the generator  $S$  is chosen such that  $H_{eff}$  does not contain the operators  $H_t^+$  and  $H_t^-$ . In order to eliminate the terms which are first order in  $t$ , the generator  $S$  reads:

$$S = -\frac{i}{U}(H_t^+ - H_t^-), \quad (1.7)$$

and, to the order  $t^2/U$ , we obtain the effective  $t$ - $J$  model:

$$H_{t-J} = -t \sum_{\langle i,j \rangle, \sigma} [(1 - n_{i-\sigma}) c_{i\sigma}^\dagger c_{j\sigma} (1 - n_{j-\sigma}) + h.c.] +$$

$$+J \sum_{\langle i,j \rangle} \left( S_i \cdot S_j - \frac{n_i n_j}{4} \right) + \text{three sites term}, \quad (1.8)$$

where  $S_i = \frac{1}{2} \sum_{\sigma\sigma'} c_{i\sigma}^\dagger \tau_{\sigma\sigma'} c_{i\sigma'}$  is the spin operator for site  $i$  ( $\tau_{\sigma\sigma'}$  being the Pauli matrices) and  $J = 4t^2/U$  is a magnetic coupling that favors an antiferromagnetic alignment of spins. The first term of Eq. (1.8) describes hopping constrained on the space with no doubly occupied sites. The nature of the super-exchange coupling  $J$  is due to the possibility of a virtual hopping of antiparallel neighboring spins, which creates an intermediate doubly occupied site with an energy gain  $-t^2/U$ , see Fig. 1.7.

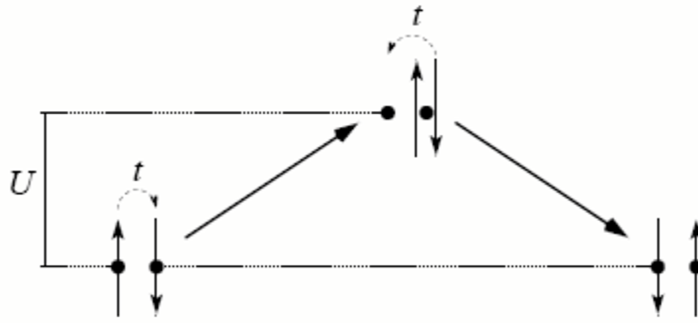


Figure 1.7: In second order of perturbation theory in  $t/U$ , if the spins of neighboring sites are antiparallel, they gain energy by a virtual process creating a double occupation.

Finally, the canonical transformation generates a three-sites term, which is proportional to the hole doping and usually neglected for simplicity. At half filling, the first term of Eq. (1.8) is zero, because every site is already occupied by one electron, and one obtains the Heisenberg model:

$$H_{Heis} = J \sum_{\langle i,j \rangle} S_i \cdot S_j, \quad (1.9)$$

The ground state of this Hamiltonian is obviously insulating and in 1988, by using Monte Carlo techniques, Reger and Young demonstrated that it has an antiferromagnetic long-range order with a magnetization reduced by 60% with respect to the classical value [60].

## 1.4 Resonating Valence Bond theories

Anderson suggested that a good variational ground state of the Heisenberg model of Eq. (1.9) could be represented as a resonating-valence bond (RVB) state, described as a liquid of spin singlets. One important consequence was that, once the system is doped, the holes inside the RVB liquid can move, possibly leading to superconductivity. This idea has led to a consistent theoretical framework to describe superconductivity in the proximity of a Mott transition. In this section, we will discuss possible realizations of RVB superconductors and give an outlook on the implementations of the RVB picture by BCS projected wave functions.

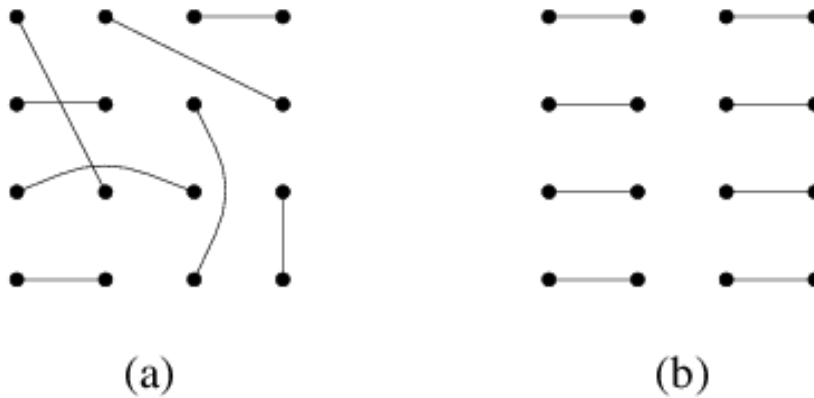


Figure 1.8: Schematic illustration of the RVB state. Sticks represent singlet bonds. (a) and (b) represent two particular Valence Bond (VB). An RVB state is superposition of different VB:  $|RVB\rangle = \sum_j a_j |VB_j\rangle$ . (a) A true spin liquid is a superposition of VB of this kind. (b) A non-magnetic RVB state with broken translational symmetry is a state where the dominant weights  $a_j$  associated to VB are of this kind.

In spite of a Neel state with a broken  $SU(2)$  symmetry, an RVB state is described by superposition of states in which two electrons of the lattice are paired to form a singlet, see Fig.1.8. Indeed, especially for small values of the spin, quantum fluctuations reduce the classical value of the order parameter, favoring a disordered ground state. Liang, Doucot, and Anderson [61] showed that the

RVB state regain some of the lost antiferromagnetic exchange energy by resonating among many different configurations, becoming, therefore, competitive with the Neel ordered state. The resonating singlet state is very similar to benzene ring with its fluctuating C–C links between a single and a double bond: this analogy motivated the term RVB. Such bonds can be either homogeneously distributed over the lattice, giving rise to a true spin-liquid with no broken symmetries [see Fig.1.8(a)] or they can be mostly arranged in some special pattern, which breaks some of the symmetries of the lattice [see Fig.1.8 (b)].

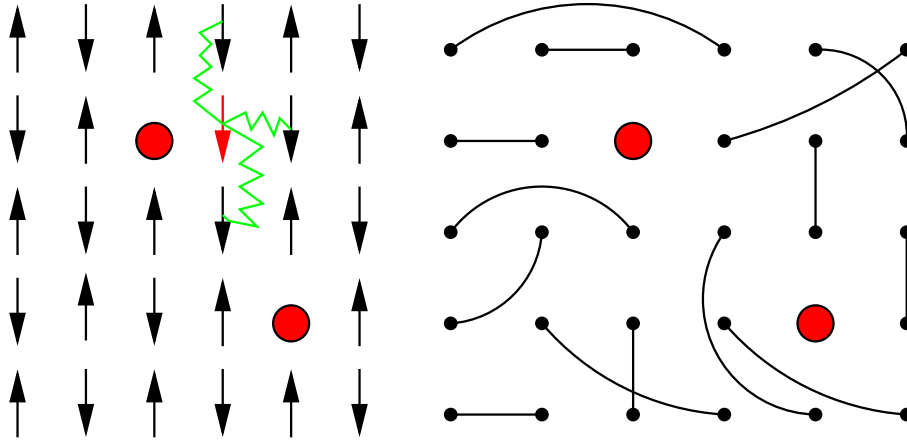


Figure 1.9: Left panel: Antiferromagnetic Neel state with some holes. The motion of a hole (bold circles) frustrates the antiferromagnetic order of the lattice. Right panel: A configuration of singlet pairs with some holes is shown. In this case the singlets can rearrange in order to avoid frustration.

Though an ordered state is realized in the undoped insulator [60], the antiferromagnetic order parameter melts with some percent of doped holes. To understand this, we can consider the example shown in Fig. 1.9. Moving holes naturally causes frustration in the antiferromagnetic order, and eventually it is better to have a paramagnetic background. The problem of a single hole moving in the background of a Neel state was studied extensively by several authors (see for example [11]); In particular, analytical calculations showed that the coherent hole motion is strongly renormalized by the interaction with the spin excitations [62, 63]. On the other hand, since singlets can easily rearrange, the presence of holes in an RVB background does not alter its nature and, therefore, in the presence of dop-

ing, the RVB state can be competitive with the Neel one, see Fig. 1.9. Moreover, the holes may condense and give rise to a superconducting state: hence, pairing could be due to RVB and not to antiferromagnetism. One of the most remarkable prediction of the RVB theory was the d-wave nature of the superconducting state. Indeed, a d-wave superconducting state was found by RVB studies as early as in 1988 [64–68], long before the pairing symmetry of HTSC was experimentally established. These early calculations also correctly described the vanishing of superconductivity above about 30% doping. By implementing the RVB idea by projected wave functions, one finds a natural explanation of the suppression of the Drude weight and of the superfluid density in the underdoped regime, as well as the particle hole asymmetry in the density of single particle states. Further successes of the RVB theory are the prediction of a weakly doping dependent nodal Fermi velocity and a quasiparticle weight that is strongly doping dependent (decreasing with doping in agreement with ARPES experiments). These effects can be understood by a decrease in the density of freely moving carriers at low doping, which results in a dispersion mainly determined by virtual hopping process proportional to the super-exchange  $J$ . In addition to the above key features of HTSC, RVB theory has also been successfully applied to several other phenomena such as charge density patterns [69–72], the interplay between superconductivity and magnetism [73–78], impurity problems [79], and vortex cores [80].

In conclusion, analytical and numerical results provide significant support to the RVB concept. Even if most RVB studies are restricted to zero temperature, as in our work, from the ground state obtained in this way it is possible to extract important information on the finite temperature properties, allowing a description of the finite temperature picture described above. However, extending the calculations to finite temperature is certainly an important and open problem in the theory of RVB superconductivity that should be addressed in the near future.

## 1.5 The RVB concept within the variational approach

In general, the variational approach offers a simple route to deal with strongly-correlated systems, since a good guess of the ground-state wave function allows one to derive the properties of the corresponding phases in a straightforward way. The variational approach starts from a guess on the functional form of the trial

wave function  $|\Psi_T(\{v_i, \Delta_i\})\rangle$ , which is supposed to be as close as possible to the true ground state. The trial wave function depends on a set of variational parameters  $\{v_i, \Delta_i\}$ , which are properly changed in order to minimize the expectation value of the variational energy  $E_V$ .

$$E_V = \frac{\langle \Psi_T(\{v_i, \Delta_i\}) | H | \Psi_T(\{v_i, \Delta_i\}) \rangle}{\langle \Psi_T(\{v_i, \Delta_i\}) | \Psi_T(\{v_i, \Delta_i\}) \rangle}. \quad (1.10)$$

The energy  $E_V$  gives an upper bound of the ground-state energy  $E_0$ , as a consequence of the variational principle that we will describe in some details in the next chapter.

A simple form for a correlated wave function can be given by:

$$|\Psi_{\mathcal{P}}\{v_i, \Delta_i\}\rangle = \mathcal{P}(\{v_i\})|D(\{\Delta_i\})\rangle, \quad (1.11)$$

where  $\mathcal{P}\{v_i\}$  is the correlation factor (or *projector*) and  $|D(\{\Delta_i\})\rangle$  is a mean-field Slater determinant. Indeed, for fermionic systems, the wave function generally must contain a determinantal part that ensures the correct antisymmetry when particles are interchanged. The correlation factor  $\mathcal{P}$  is commonly expressed as the exponential of a two-body operator, like density-density or spin-spin, whose explicit form will be specified in the following. At this level, it is important to stress that the projector inserts correlation into the wave function, whose remaining part corresponds to the mean-field Slater determinant  $|D\rangle$ . Notice that the term projector is often used in the context of spin models, where  $\mathcal{P}$  totally projects out the configurations with a finite number of double occupancies. In that case  $\mathcal{P}$  is denoted as *full projector*.

The Slater determinant generally corresponds to the ground state of a mean-field Hamiltonian. In the simplest case, it is the uncorrelated Fermi sea:

$$|FS\rangle = \prod_{\epsilon_k \leq \epsilon_F} c_{k\uparrow}^\dagger c_{k\downarrow}^\dagger |0\rangle, \quad (1.12)$$

which is the ground state of the free tight-binding Hamiltonian with energy dispersion  $\epsilon_k$ :

$$H_{FS} = \sum_{k\sigma} \epsilon_k c_{k\sigma}^\dagger c_{k\sigma}, \quad (1.13)$$

where  $\epsilon_k = -2t \sum_{j=1}^d \cos(k_j)$  and  $\epsilon_F$  is the Fermi energy. Nevertheless, also the determinant can be parametrized, for example it can be the ground state of the

BCS Hamiltonian:

$$H_{BCS} = \sum_{k,\sigma} \epsilon_k c_{k\sigma}^\dagger c_{k\sigma} + \sum_{i,j} \Delta_{ij} (c_{i\uparrow} c_{j\downarrow} + c_{j\downarrow}^\dagger c_{i\uparrow}^\dagger), \quad (1.14)$$

where  $\{\Delta_{ij}\}$  depend on the distance  $|i - j|$  and are chosen in order to minimize the expectation value of the energy. The BCS ground state is a singlet state that corresponds, in the case of total projection, to a particular RVB state with a given amplitude for the singlets. Another possible Slater determinant comes from the mean-field antiferromagnetic Hamiltonian:

$$H_{AF} = \sum_{k,\sigma} \epsilon_k c_{k,\sigma}^\dagger c_{k,\sigma} + \Delta_{AF} \sum_i (-1)^{r_i} (n_{i\uparrow} - n_{i\downarrow}), \quad (1.15)$$

with the variational antiferromagnetic parameter  $\Delta_{AF}$ . In this case, the corresponding Slater determinant breaks the translational and the spin SU(2) symmetries.

It should be stressed that, in general, the projector modifies only the amplitudes of each configuration, while the parameters inside the determinant are also responsible of the phases: the nodal structure of the trial wave function strongly depends upon the choice of the determinant.

The  $t$ - $J$  Hamiltonian is the best known model for studying RVB superconductivity, because it includes the super-exchange term explicitly, and this is the term which is responsible for the formation of singlets. In the following we start with the  $t$ - $J$  Hamiltonian as an appropriate microscopic model for HTSC. The wave function which is constructed by projecting out doubly occupied sites and fixing the number of particles from the ground state of the BCS Hamiltonian (1.14) provides an elegant and compact way to study the occurrence of superconductivity in the  $t$ - $J$  model:

$$|\Psi_{RVB}\rangle = \mathcal{P}_G \mathcal{P}_N |BCS\rangle, \quad (1.16)$$

where  $\mathcal{P}_G$  and  $\mathcal{P}_N$  are the Gutzwiller projector (that forbids doubly occupied sites) and the projector that fixes the number of particles to be equal to the number of sites, respectively;  $|BCS\rangle$  is the ground state of the BCS Hamiltonian (1.14). The form of this RVB wave function provides an unified description of the Mott insulating phase and the doped superconductor. Moreover, it immediately suggests the presence of singlet correlations in the undoped insulator and relates them to a superconducting state away from half filling.

In this thesis we will generalize the RVB wave function by considering a mean-field Hamiltonian which possesses both BCS pairing and antiferromagnetic order parameter. In particular, for obtaining the correct antiferromagnetic properties, we will consider the antiferromagnetic term in the  $x - y$  plane, together with a projector considering spin-spin correlations along the  $z$  axis. We anticipate that the eigenstate of this mean field Hamiltonian is something more complicated than the mean-field Slater determinant, since it is described by an algebraic object called *Pfaffian*. Moreover, we will apply to this object, projectors that fix the number of particles, forbid the double occupancy, and for enhancing the charge and spin correlations we will apply the Jastrow factors that we will describe in the following section. We will see in the next chapter how to calculate the variational energy and other interesting observables of a state by using variational techniques. Here, we will just say that the projected wave functions have the advantage that they can be studied both analytically, by considering the Gutzwiller approximation, and numerically, by using pure variational techniques and exact diagonalization. Since these wave functions provide a simple way to study different kind of correlations, they have been widely used in the literature.

## 1.6 Long-range correlations: The Jastrow factor

In this section we briefly discuss how projected states can be extended to study a wide variety of strongly correlated systems, by highly improving their accuracy. Apart from HTSC, these wave functions have been used for the description of Mott insulators [81], for the superconductivity in organic compounds [82, 83] and for the Luttinger liquid behavior in low-dimensional models [84, 85].

Historically, the Jastrow factor was introduced for continuum systems [86] in order to take into account correlation effects through a two-body term of the form:

$$\mathcal{P}_J = \exp \left[ \frac{1}{2} \sum_{i,j} v(r_{ij}) n_i n_j \right] , \quad (1.17)$$

where  $v(r_{ij}) = v(|r_i - r_j|)$  are variational parameters (which for homogeneous and isotropic systems depend only on the relative distance among the particles), and  $n_i$  is the particle density at position  $r_i$ . It is useful to consider also the Fourier

transformed Jastrow factor:

$$\mathcal{P}_J = \exp \left[ \frac{1}{2} \sum_q v_q n_q n_{-q} \right] , \quad (1.18)$$

where  $v_q = \sum_r v(r) e^{iqr}$  and  $n_q = \frac{1}{\sqrt{L}} \sum_r n_r e^{iqr}$  are the Fourier transformed Jastrow parameters and particle density, respectively. The exponential form (1.17) guarantees the size consistency of the wave function. For fermionic systems, the Jastrow factor is applied to a Slater determinant or to a Pfaffian  $|D\rangle$ , in order to recover the correct antisymmetric form:

$$|\Psi_J\rangle = \mathcal{P}_J |D\rangle . \quad (1.19)$$

The Jastrow wave function has been widely studied on continuum systems, with the employment of a large variety of analytic and numerical techniques. For instance, in a series of papers, Sutherland showed that the Jastrow wave function corresponds to the exact ground state of a family of one-dimensional Hamiltonians defined on the continuum [87]. The lattice version of the Sutherland's problem was found for a spin system by Shastry and Haldane [88, 89], who considered a spin 1/2 chain with a long-range  $1/r^2$  antiferromagnetic exchange. By using previous results by Metzner and Vollhardt on the exact spin properties of the fully-projected Gutzwiller state, they found the exact ground state of this model.

The most interesting analytic and numerical results concerning the properties of the Jastrow wave function come from its wide applications in Helium physics. In this field, starting from the very early approach of Mc Millan [90], who used a parametrization of the Jastrow term coming from the solution of the corresponding two-body problem, the form of the Jastrow factor has been subsequently fine tuned [91–94] in order to reproduce accurately the properties of the  $^4\text{He}$  liquid state. It turned out that, even if the ground-state energy is well approximated by using a short-range correlation term, the addition of a structure in the parameters  $v(r_{ij})$  at large distances is fundamental, in order to reproduce correctly the pair-distribution function and structure factor of the liquid.

The fact that the Jastrow factor involves many variational parameters, whose number grows with the lattice size, constitutes the main drawback for the application of this wave function. For this reason, in many calculations, a functional form of the Jastrow parameters is considered and fixed, hence reducing the number of

independent parameters. This implies an easy-to-handle wave function, which on the other hand could be biased by the choice of the functional form, spoiling the variational flexibility of Eq. (1.17). There are examples where a good guess for the functional form of the Jastrow parameters gives accurate results also for lattice models. Indeed, a long-range Jastrow wave function with a logarithmic form  $v_{ij} = \ln(r_i - r_j)$  turns out to be the correct ansatz which induces Luttinger-liquid correlations in the one dimensional  $t-J$  model [84]. In the one-dimensional Hubbard model an appropriate choice of the density-density Jastrow factor in momentum space allows to distinguish between metallic and insulating behavior [81]. In the two-dimensional  $t-J$  model, the Jastrow wave function is often used to improve the variational energy of a projected superconducting state [95, 96].

Moreover, the use of the spin-Jastrow factor on the Heisenberg model gave strong indications that a wave function of this type is very accurate for quantum-spin systems [97]. The spin-Jastrow factor has the following form:

$$\mathcal{P}_J^{S^z} = \exp \left[ \frac{1}{2} \sum_{i,j} v_{ij}^z S_i^z S_j^z \right] , \quad (1.20)$$

where  $S_j^z$  is the  $z$ -component of the spin associated to the particle on site  $j$ . In this case, the spin-Jastrow factor is applied to a classical ordered state and the long-range form of  $v_{ij}^z$ , deduced from analytic calculations, allows one to reproduce the correct spin-correlation functions in the quantum spin model [98, 99]. An appropriate spin-spin Jastrow factor can also create antiferromagnetic order in a non magnetic wave function. This fact can give us the idea of the ability of the Jastrow term to induce a new long-range order not present in the unprojected wave function.

However, there are also several cases in which a functional form of the Jastrow factor is not known a priori: in these cases a full optimization of all the independent parameters is needed. This is the strategy that will be used in this thesis, where we will use a numerical technique that allows us to optimize several variational parameters within the Monte Carlo approach (see next chapter). So the incorporation of Jastrow factor provides an additional powerful way to extend the class of projected wave function. Finally, we would like to remark that the spin-Jastrow factor is as often used as the density-density or the holon-doublon Jastrow terms. However, we will show in this thesis that the inclusion of the spin-

spin Jastrow factor is also very important when considering charge fluctuations in the  $t-J$  model.



# Chapter 2

## Numerical Methods

Monte Carlo methods allow one to evaluate, by means of a stochastic sampling, integrals over a multidimensional space. This is very useful for quantum many-body problems, where in general the calculation of expectation values cannot be handled analytically, since the wave function of the system cannot be factorized into one-particle states.

The core of all Monte Carlo methods is the Metropolis algorithm [100] which generates a Markov chain, i.e., a random walk in configuration space. The configurations sampled during the random walk are distributed, after a certain number of steps required to reach equilibrium, according to a given stationary probability distribution.

The variational Quantum Monte Carlo approach consists in the direct application of the Metropolis algorithm to sample the probability distribution given by the modulus squared of a given trial wave function.

Since the topic of Monte Carlo methods is covered by many textbooks we will not describe its general principles in this thesis. In the following, we will focus on the direct implementation of the Monte Carlo statistical method in our quantum variational problem. The general techniques used here are the variational quantum Monte Carlo and the Green's function Monte Carlo techniques. They allow us to describe remarkably large systems with a numerical method. Moreover, we will describe in some detail the stochastic reconfiguration algorithm which allows us to minimize the variational energy in presence of a large number of parameters. At the beginning we will also briefly describe the Lanczos method, which has

been used in this thesis for making a comparison of the exact energies for small system sizes ( $L \leq 26$ ), with the corresponding energy expectation values of our new improved variational wave function.

## 2.1 Lanczos

From a general point of view, the ground state  $|\Phi_0\rangle$  of an Hamiltonian  $H$  can be obtained by the *power method* from a trial wave function  $|\Psi_T\rangle$ , provided that  $\langle\Psi_T|\Phi_0\rangle \neq 0$  and that the ground state is unique, that we will assume in the following (simple extensions are possible). Indeed, if we define the operator  $G = \Lambda - H$ , with  $\Lambda$  a suitable constant chosen to allow us the convergence to the ground-state, we have that:

$$G^n|\Psi_T\rangle = (\Lambda - E_0)^n \left\{ a_0|\Phi_0\rangle + \sum_{i \neq 0} \left( \frac{\Lambda - E_i}{\Lambda - E_0} \right)^n a_i|\Phi_i\rangle \right\}, \quad (2.1)$$

where  $E_i$  and  $|\Phi_i\rangle$  are the eigenvalues and eigenvectors of  $H$  respectively, and  $a_i = \langle\Phi_i|\Psi_T\rangle$ . Therefore

$$\lim_{n \rightarrow \infty} G^n|\Psi_T\rangle \sim |\Phi_0\rangle, \quad (2.2)$$

that is, as  $n$  goes to infinity, the iteration converges to the ground-state of the Hamiltonian  $H$ , because  $\frac{\Lambda - E_i}{\Lambda - E_0} < 1$  for large enough  $\Lambda$ .

Starting from the power method, it is possible to define a much more efficient iterative procedure for the determination of the lowest eigenstate of Hermitian matrices, known as the Lanczos technique. Indeed, within the power method, the ground-state is approximated by a single state, i.e.  $|\Phi_0\rangle \sim G^n|\Psi_T\rangle$ , by contrast, the basic idea of the Lanczos method, is to use all the information contained in the powers  $G^i|\Psi_T\rangle$ , with  $i = 1, \dots, n$  to reconstruct the ground-state  $|\Phi_0\rangle$ , namely

$$|\Phi_0\rangle \sim \sum_{i=1, \dots, n} \alpha_i H^i |\Psi\rangle. \quad (2.3)$$

However, the vectors generated by the power method are not orthogonal, whereas within the Lanczos method a special orthogonal basis is constructed. This basis is generated iteratively. The first step is to choose an arbitrary vector  $|\Psi_1\rangle$  of the Hilbert space, the only requirement is that this vector has a non-zero overlap with

the true ground-state. If there is no *a priori* information about the ground-state, this requirement is satisfied by selecting random coefficients in the working basis, so that there is only a vanishing probability to be orthogonal. If some information about the ground-state is known, like its momentum, spin, or its properties under rotation, then it is useful to initialize the starting vector using these properties, choosing a vector that belongs to the particular subspace having the right quantum numbers.

The Lanczos procedure consists in generating a set of orthogonal vectors as follow: we normalize  $|\Psi_1\rangle$  and define a new vector by applying the Hamiltonian  $H$  to the initial state, and we subtract the projection over  $|\Psi_1\rangle$

$$\beta_2|\Psi_2\rangle = H|\Psi_1\rangle - \alpha_1|\Psi_1\rangle, \quad (2.4)$$

the coefficients  $\alpha_1$  and  $\beta_2$  are such that  $\langle\Psi_2|\Psi_2\rangle = 1$  and  $\langle\Psi_1|\Psi_2\rangle = 0$ , that is:

$$\alpha_1 = \langle\Psi_1|H|\Psi_1\rangle \quad (2.5)$$

$$\beta_2 = \langle\Psi_2|H|\Psi_1\rangle. \quad (2.6)$$

Then we can construct a new state, orthogonal to the previous ones as

$$\beta_3|\Psi_3\rangle = H|\Psi_2\rangle - \alpha_2|\Psi_2\rangle - \beta_2|\Psi_1\rangle, \quad (2.7)$$

with

$$\alpha_2 = \langle\Psi_2|H|\Psi_2\rangle \quad (2.8)$$

$$\beta_3 = \langle\Psi_3|H|\Psi_2\rangle. \quad (2.9)$$

In general the procedure can be generalized by defining an orthogonal basis recursively as

$$\beta_{n+1}|\Psi_{n+1}\rangle = H|\Psi_n\rangle - \alpha_n|\Psi_n\rangle - \beta_n|\Psi_{n-1}\rangle, \quad (2.10)$$

for  $n = 1, 2, 3, \dots$ , being  $|\Psi_0\rangle = 0$ ,  $\beta_1 = 0$  and

$$\alpha_n = \langle\Psi_n|H|\Psi_n\rangle \quad (2.11)$$

$$\beta_{n+1} = \langle\Psi_{n+1}|H|\Psi_n\rangle. \quad (2.12)$$

It is worth noting that, by construction, the vector  $|\Psi_n\rangle$  is orthogonal to all the previous ones, although we subtract only the projections of the last two. In this

basis the Hamiltonian has a simple tridiagonal form

$$H = \begin{pmatrix} \alpha_1 & \beta_2 & 0 & 0 & \dots \\ \beta_2 & \alpha_2 & \beta_3 & 0 & \dots \\ 0 & \beta_3 & \alpha_3 & \beta_4 & \dots \\ 0 & 0 & \beta_4 & \alpha_4 & \dots \\ \dots & \dots & \dots & \dots & \dots \end{pmatrix},$$

and once in this form, the matrix can be easily diagonalized by using standard library subroutines. In principle, in order to obtain the exact ground-state of the Hamiltonian, it is necessary to perform a number of iterations equal to the dimension of the Hilbert space. In practice, the greatest advantage of this method is that a very accurate approximation of the ground-state is obtained after a very small number of iterations, typically of the order of 100, depending on the model.

The main limitation of this technique is the exponential growing of the Hilbert space. Indeed, although the ground-state can be written with a great accuracy in terms of few  $|\Psi_n\rangle$  as

$$|\Phi_0\rangle \simeq \sum_{n=1}^{\sim 100} c_n |\Psi_n\rangle, \quad (2.13)$$

it is necessary to express the general vector of the Lanczos basis  $|\Psi_n\rangle$  in a suitable basis to which the Hamiltonian is applied. For example, for the  $t - J$  model, each site can be singly occupied by a spin up or down, or empty. In this way the Hilbert space needed for describe all possible configuration became enormous yet for small lattice sizes requiring an huge computer memory. In practice this problem can be alleviated by using the symmetries of the Hamiltonian. For example, in the case of periodic boundary condition (the ones that we use in our work), there is translational invariance and the total momentum of the system is a conserved quantity. Moreover, in a square lattices also discrete rotations of  $\pi/2$  and reflections with respect to a particular axis are defined and can give rise to good quantum numbers.

In principle the Lanczos procedure, as described in Eqs. (2.10), (2.11) and (2.12), can give information about both the ground-state energy and the ground-state vector. In practice, during the Lanczos matrix construction, only three vectors are stored, i.e.  $|\Psi_{n+1}\rangle$ ,  $|\Psi_n\rangle$  and  $|\Psi_{n-1}\rangle$  (by using an improved algorithm, it is possible to store only two vectors), because each element  $|\Psi_n\rangle$  of the basis

is represented by a large set of coefficients, when it is expanded in the basis selected to carry out the problem. Therefore, it is not convenient to store all the  $|\Psi_n\rangle$  vectors individually, since this procedure would demand a memory requirement equal to the size of the Hilbert space times the number of Lanczos steps. A possible solution of the problem is to run the Lanczos twice: in the first run we find the coefficient  $c_n$  of Eq. (2.13), in the second run the vectors  $|\Psi_n\rangle$  are systematically reconstructed one by one, multiplied by their coefficient and stored in  $|\Phi_0\rangle$ .

Within Lanczos and Variational Monte Carlo method, it is useful to consider not only the  $N \times N$  cluster, but also other tilted square lattices, which have axes forming non-zero angles with lattice axes. In general it is possible to construct square cluster with  $L = l^2 + m^2$ , being  $l$  and  $m$  positive integers. Only cluster with  $l = 0$  (or  $m = 0$ ) or  $l = m$  have all the symmetries of the infinite lattice, while clusters with  $l \neq m$  can have rotations but not reflections with respect to a given axis. In our work we used tilded cluster with  $l = m$  as we will show.

## 2.2 Variational Monte Carlo

One of the most useful properties of quantum mechanics is that the expectation value of an Hamiltonian  $H$  over any trial wave function  $|\Psi\rangle$  gives an upper bound to the ground-state energy  $E_0$

$$E = \frac{\langle \Psi | H | \Psi \rangle}{\langle \Psi | \Psi \rangle} \geq E_0. \quad (2.14)$$

This can be easily seen by inserting the complete set of the eigenfunction  $|\Phi_i\rangle$  of  $H$  with energy  $E_i$

$$\frac{\langle \Psi | H | \Psi \rangle}{\langle \Psi | \Psi \rangle} = \sum_i E_i \frac{|\langle \Phi_i | \Psi \rangle|^2}{\langle \Psi | \Psi \rangle} = E_0 + \sum_i (E_i - E_0) \frac{|\langle \Phi_i | \Psi \rangle|^2}{\langle \Psi | \Psi \rangle} \geq E_0. \quad (2.15)$$

In this way, if we have a set of different wave functions, we can choose the best approximation of the ground-state by looking for the lowest expectation value of the energy.

In general, due to the rapid growth of the Hilbert space with the lattice size, the variational expectation values (2.14) can be calculated exactly only for very small clusters unless the wave function is particularly simple like e.g. a Slater

determinant. On larger sizes only a Monte Carlo approach to evaluate Eq. (2.14) is possible for correlated wave functions. In order to show how statistical methods can be used to calculate this kind of expectation values, it is useful to introduce complete sets of states  $|x\rangle$ <sup>1</sup> in Eq. (2.14)

$$\frac{\langle \Psi | H | \Psi \rangle}{\langle \Psi | \Psi \rangle} = \frac{\sum_{x,x'} \Psi(x') H_{x',x} \Psi(x)}{\sum_x \Psi^2(x)}, \quad (2.16)$$

where  $\Psi(x) = \langle x | \Psi \rangle$ ,  $H_{x',x} = \langle x' | H | x \rangle$ , and for the sake of simplicity, we have restricted to real wave functions. Defining the *local energy*  $E_x$  as

$$E_x = \frac{\langle x | H | \Psi \rangle}{\langle x | \Psi \rangle} = \sum_{x'} \frac{\Psi(x')}{\Psi(x)} H_{x',x}, \quad (2.17)$$

Eq. (2.16) can be written as

$$E = \frac{\langle \Psi | H | \Psi \rangle}{\langle \Psi | \Psi \rangle} = \frac{\sum_x E_x \Psi^2(x)}{\sum_x \Psi^2(x)}. \quad (2.18)$$

The local energy  $E_x$  depends crucially on the choice of the wave function  $|\Psi\rangle$ , in particular, if  $|\Psi\rangle$  is an eigenstate of  $H$  with eigenvalue  $E$ , it comes out from Eq. (2.17) that  $E_x = E$ , and the Monte Carlo method is free from statistical fluctuations.

The evaluation of Eq. (2.18) can be done by generating a sample  $X$  of  $\mathcal{N}$  configurations  $x_i$  according to the probability distribution

$$P(x) = \frac{\Psi^2(x)}{\sum_{x'} \Psi^2(x')} \quad (2.19)$$

and then averaging the values of the local energy over these configurations

$$E \simeq \frac{1}{\mathcal{N}} \sum_{x \in X} E_x. \quad (2.20)$$

In practice, the simplest method to generate a set of configurations according to the probability distribution  $P(x)$  is the Metropolis algorithm [100]: given a

---

<sup>1</sup>For example, for the *spin*  $-\frac{1}{2}$  Heisenberg model, in which each site can have an up or a down spin, it is convenient to work in the Ising basis, where  $S_z$  is defined at every site, i.e. a generic element is given by  $|x\rangle = |\uparrow, \downarrow, \uparrow, \uparrow, \downarrow, \uparrow, \dots\rangle$ .

For the  $t - J$  model, each site can be singly occupied, by a spin up or down, or empty, and the generic elements reads  $|x\rangle = |\uparrow, \downarrow, 0, \uparrow, \downarrow, 0, 0, \uparrow, \dots\rangle$ .

configuration  $x$ , a new configuration  $x'$  is accepted if a random number  $\xi$ , between 0 and 1, satisfies the condition

$$\xi < \frac{P(x')}{P(x)} = \left[ \frac{\Psi(x')}{\Psi(x)} \right]^2, \quad (2.21)$$

otherwise the new configuration is kept equal to the old one,  $x' = x$ . We will explain in some more details the Metropolis algorithm in the following subsection.

Here we wish to note that, by using the variational Monte Carlo, it is possible to calculate any kind of expectation value, over a given wave function in a similar way as what was done for the energy:

$$\langle O \rangle = \frac{\langle \Psi | O | \Psi \rangle}{\langle \Psi | \Psi \rangle} = \frac{\sum_x O_x \Psi^2(x)}{\sum_x \Psi^2(x)}, \quad (2.22)$$

where

$$O_x = \frac{\langle x | O | \Psi \rangle}{\langle x | \Psi \rangle} = \sum_{x'} \frac{\Psi(x')}{\Psi(x)} O_{x',x}. \quad (2.23)$$

An important point is that the only rigorous result is the upper bound to the ground-state energy, and there are no criteria about the accuracy of other properties of the ground-state, such as  $\langle O \rangle$ .

### 2.2.1 The Metropolis algorithm for quantum problems

We have seen in Section 1.5 that the general form of a correlated wave function is constituted by a correlation term acting, in the fermionic case, on a Slater determinant, i.e.,  $|\Psi\rangle = \mathcal{P}|D\rangle$ . In the following, we show how the statistical evaluation of integrals containing the square modulus of this wave function is efficiently implemented.

The first step in the variational Monte Carlo algorithm consists in choosing the initial coordinates  $\{x_i\}_0$  for the  $N$  particles on the lattice, either randomly (with the condition that  $|\Psi(x)|^2 \neq 0$ ) or taking them from a previous Monte Carlo simulation. Then a new trial configuration  $\{x_i^T\}_0$  is chosen by moving one of the particles from its old position to another site. The Markov chain is then constructed following the Metropolis algorithm, as shown below. For any move from the  $n$ -th configuration of the Markov chain  $\{x_i\}_n$  to the new trial configuration

$\{x_i^T\}_n$ , the latter is accepted, i.e.,  $\{x_i\}_{n+1} = \{x_i^T\}_n$  with a probability equal to:

$$P = \min [1, \mathcal{R}] \quad \text{with} \quad \mathcal{R} = \frac{|\Psi(\{x_i^T\}_n)|^2}{|\Psi(\{x_i\}_n)|^2}, \quad (2.24)$$

where  $\Psi(\{x_i\}_n)$  is the wave function of the system associated to the configuration  $\{x_i\}_n$ . This is done in practice by extracting a positive random number  $0 < \eta \leq 1$ ; if  $\mathcal{R} \geq \eta$  then  $\{x_i\}_{n+1} = \{x_i^T\}_n$ , otherwise the proposed move is rejected and  $\{x_i\}_{n+1} = \{x_i\}_n$ . The calculation of the ratio  $\mathcal{R}$  would require, for fermions, the evaluation of two Slater determinants, which scale as  $N^3$ . The fact that the two configurations are related among each other by the displacement of one particle, allows us to perform a more efficient calculation, which for fermions corresponds to  $O(N)$  operations. Also the ratio among the correlation terms (Jastrow factors) can be performed in an efficient way, taking into account that only one particle changes its position.

After a certain number of steps, known as thermalization time, the configurations  $\{x_i\}_n$  generated at each step  $n$  in the Markov chain are independent from the initial condition  $\{x_i\}_0$  and are distributed according to the probability:

$$p_{\{x_i\}} = \frac{|\Psi(\{x_i\})|^2}{\sum_{\{x_i\}} |\Psi(\{x_i\})|^2}.$$

Notice that this algorithm does not require to know the normalization of the wave function, since it always deals with its ratios over different configurations. This is a big advantage of Monte Carlo methods, since in general the normalization constant is not known or it is difficult to compute.

Finally, the expectation value  $\langle O \rangle$  of any operator  $O$  reduces to average over the values assumed by  $O$  along the  $M$  steps of the Markov chain:

$$\bar{O} = \frac{1}{M} \sum_{n=1}^M O(\{x_i\}_n), \quad (2.25)$$

where  $O(\{x_i\}_n)$  is the observable  $O$  calculated for the configuration  $\{x_i\}_n$ . Indeed the central limit theorem ensures that:

$$\lim_{M \rightarrow \infty} \bar{O} = \langle O \rangle,$$

where  $\langle O \rangle$  is the true expectation value of  $O$  calculated from the probability  $p_x$ . The statistical error related to the fact that we are sampling a finite set of configurations can be deduced from the variance:

$$\sigma^2(\bar{O}) = (\bar{O} - \langle O \rangle)^2.$$

One can show that the statistical error scales as the square root of the inverse length  $M$  of the Markov chain, namely:

$$\sigma^2(\bar{O}) \simeq \frac{\tau}{M} \sigma^2(O),$$

where  $\sigma^2(O) = \langle (O^2 - \langle O \rangle^2) \rangle$  and  $\tau$  is the autocorrelation time, i.e., the number of steps of the Markov chain which separate two statistically independent configurations. Therefore, for large enough samplings, the average quantities calculated with the Metropolis algorithm give reliable estimates of the true expectation values of the system. In order to calculate expectation values among uncorrelated samplings, the *bin technique* is usually employed. This corresponds to average first among  $M_{bin}$  configurations, according to (2.25):

$$\bar{O}^{bin} = \frac{1}{M_{bin}} \sum_{n=1}^{M_{bin}} O(\{x_i\}_n) \quad (2.26)$$

In this way the quantities  $\bar{O}^{bin}$  are less correlated than the original  $O(\{x_i\}_n)$ . Then, the calculation of the expectation value follows:

$$\bar{O} = \frac{1}{N_{bin}} \sum_{n=1}^{N_{bin}} \bar{O}_n^{bin}, \quad (2.27)$$

where  $N_{bin} = M/M_{bin}$ . In this way we get  $\tau \simeq 1$ , hence  $\bar{O} = \langle O \rangle$  and the variance can be evaluated in the standard way as:

$$\sigma^2(O) = \frac{1}{(N_{bin} - 1)} \sum_{n=1}^{N_{bin}} (\bar{O}_n^{bin} - \langle O \rangle)^2 \quad (2.28)$$

## 2.3 The minimization algorithm

Consider the variational wave function  $|\Psi_T(\alpha)\rangle$ , where  $\alpha = \{\alpha_k\}$  generally corresponds to the set of variational parameters for both the correlation factor and

the Slater determinant/Pfaffian introduced in Section 1.5. The expectation value of the variational energy can be written as:

$$E_T(\alpha) = \frac{\langle \Psi_T(\alpha) | H | \Psi_T(\alpha) \rangle}{\langle \Psi_T(\alpha) | \Psi_T(\alpha) \rangle} = \frac{\sum_x |\langle x | \Psi_T(\alpha) \rangle|^2 e_L(x)}{\sum_x |\langle x | \Psi_T(\alpha) \rangle|^2} \geq E_0, \quad (2.29)$$

where  $E_0$  is the ground-state energy and the completeness relation  $\sum_x |x\rangle\langle x|$  over all possible configurations  $|x\rangle$  has been inserted.<sup>2</sup> The quantity  $e_L(x)$  is called *local energy* and is given by:

$$e_L(x) = \frac{\langle x | H | \Psi_T(\alpha) \rangle}{\langle x | \Psi_T(\alpha) \rangle}. \quad (2.30)$$

Eq.(2.29) shows that the expectation value of the energy corresponds to the mean value of the the local energy  $e_L(x)$  calculated among all possible configurations  $|x\rangle$ , each weighted according to the square modulus of the normalized wave function. As shown in the previous section, this can be done stochastically by means of a sum over the Markov chain in configuration space:

$$E_T(\alpha) = \frac{1}{M} \sum_{n=1}^M e_L(x_n).$$

Let us now explain how to vary the parameters  $\alpha = \{\alpha_k\}$  in order to minimize the variational energy, following the stochastic reconfiguration algorithm introduced in [101]. To this purpose consider the starting trial wave function  $|\Psi_T(\alpha^0)\rangle$ , where  $\alpha^0 = \{\alpha_k^0\}$  is the set of  $p$  initial variational parameters (where  $k = 1, \dots, p$ ).<sup>3</sup> In linear approximation the new wave function, obtained after a small change of the parameters, can be written as:

$$\begin{aligned} |\Psi_T(\alpha')\rangle &\simeq |\Psi_T(\alpha^0)\rangle + \sum_{k=1}^p \delta\alpha_k \frac{\partial |\Psi_T(\alpha^0)\rangle}{\partial \alpha_k} = \\ &= \left[ 1 + \sum_{k=1}^p \delta\alpha_k O_k \right] |\Psi_T(\alpha^0)\rangle, \end{aligned} \quad (2.31)$$

where the operators  $O_k$  are defined for any configuration  $|x\rangle$  as the logarithmic

<sup>2</sup>For simplicity we indicate with  $|x\rangle$  the configuration  $\{x_i\}$  for  $N$  particles.

<sup>3</sup>In the following let us assume for simplicity that  $|\Psi_T(\alpha^0)\rangle$  is normalized.

derivative of the wave function with respect to the parameters  $\alpha_k$ <sup>4</sup>:

$$O_k(x) = \frac{\partial \ln \Psi_T^\alpha(x)}{\partial \alpha_k} \quad (2.32)$$

and  $\Psi_T^\alpha(x) = \langle x | \Psi_T(\alpha) \rangle$ . Putting  $O_0 = 1$ ,  $\delta\alpha_0 = 1$  we can write:

$$|\Psi_T(\alpha')\rangle = \sum_{k=0}^p \delta\alpha_k O_k |\Psi_T(\alpha^0)\rangle. \quad (2.33)$$

In general  $\delta\alpha_0 \neq 1$ , due to the normalization of  $|\Psi_T(\alpha')\rangle$ , and one can redefine  $\delta\tilde{\alpha}_k = \frac{\delta\alpha_k}{\delta\alpha_0}$  for each variational parameter  $\alpha_k$ . In order to find  $|\Psi_T(\alpha')\rangle$  such that it approaches the ground state, one possibility resides in projection methods. A standard procedure of projection methods corresponds to filter out the exact ground-state wave function by iteratively applying the Hamiltonian operator to the trial ground state. Therefore, we can apply the *power method* to the starting wave function:

$$|\bar{\Psi}_T(\alpha^0)\rangle = (\Lambda - H)|\Psi_T(\alpha^0)\rangle, \quad (2.34)$$

where  $\Lambda$  is a positive constant, which ensures convergence to the ground state. The next step, in order to ensure that  $|\Psi_T(\alpha')\rangle$  has a lower energy with respect to  $|\Psi_T(\alpha^0)\rangle$ , corresponds to equate Eqs. (2.33) and (2.34) in the subspace spanned by the vectors  $\{O_k|\Psi_T(\alpha^0)\rangle\}$ .

Combining the r.h.s. of Eqs. (2.33) and (2.34) and projecting them on the  $k'$ -th component we get:

$$\langle \Psi_T(\alpha^0) | O_{k'} (\Lambda - H) | \Psi_T(\alpha^0) \rangle = \sum_{k=0}^p \delta\alpha_k \langle \Psi_T(\alpha^0) | O_{k'} O_k | \Psi_T(\alpha^0) \rangle. \quad (2.35)$$

In this way the quantities  $\delta\alpha_k$  correspond to the variations of the wave function parameters that lower the variational energy for  $\Lambda$  large enough that the linear approximation is correct. They can be calculated by solving the linear system of equations of the type given in (2.35). It is a system of  $(p + 1)$  equations, which can be written as:

$$f_{k'} = \sum_{k=0}^p \delta\alpha_k S_{kk'}, \quad (2.36)$$

---

<sup>4</sup>For example if  $\alpha_k = v_k$ , i.e., the Jastrow parameter associated to the distance  $k$ , the operator  $O_k$  is defined as  $O_k(x) = \sum_j n_j(x) n_{j+k}(x)$

where  $f_k$  are the *generalized forces*:

$$f_{k'} = \langle \Psi_T(\alpha^0) | O_{k'} (\Lambda - H) | \Psi_T(\alpha^0) \rangle \quad (2.37)$$

and  $S_{kk'}$  is the  $(p+1) \times (p+1)$  positive definite matrix given by:

$$S_{kk'} = \langle \Psi_T(\alpha^0) | O_{k'} O_k | \Psi_T(\alpha^0) \rangle. \quad (2.38)$$

The system can be reduced to  $p$  equations since  $\delta\alpha_0$  is related to the normalization of the wave function. Indeed, considering Eq.(2.35) for  $k' = 0$ , since we have put  $O_0 = 1$  in (2.33), the value of  $\delta\alpha_0$  reduces to:

$$\delta\alpha_0 = \Lambda - E_T(\alpha^0) - \sum_{k=1}^p \delta\alpha_k S_{k0}. \quad (2.39)$$

Substituting (2.39) in (2.35) we obtain the reduced system of equations:

$$\bar{f}_k = \sum_{k'=1}^p \delta\alpha_{k'} \bar{S}_{kk'}, \quad (2.40)$$

where:

$$\bar{f}_k = \langle \Psi_T(\alpha^0) | O_k | \Psi_T(\alpha^0) \rangle \langle \Psi_T(\alpha^0) | H | \Psi_T(\alpha^0) \rangle - \langle \Psi_T(\alpha^0) | O_k H | \Psi_T(\alpha^0) \rangle \quad (2.41)$$

and

$$\bar{S}_{kk'} = S_{kk'} - S_{k0} S_{k'0}. \quad (2.42)$$

Notice that the forces  $\bar{f}_k$  correspond to  $\bar{f}_k = \frac{\partial E_T(\alpha)}{\partial \alpha_k}$ . Since at equilibrium one has  $\bar{f}_k = 0$ , implying  $\delta\alpha_k = 0$ , this corresponds to satisfy the Euler equations for the variational minimum:<sup>5</sup>

$$\frac{\partial E_T(\alpha)}{\partial \alpha_k} = 0.$$

Moreover, from the definition (2.41), the fact that  $\bar{f}_k = 0$  implies that the variational wave function fulfills the same property of an exact eigenstate, namely:

$$\langle O_k H \rangle = \langle O_k \rangle \langle H \rangle, \quad (2.43)$$

---

<sup>5</sup>This is strictly valid in the case in which the Hamiltonian does not depend on the variational parameters, which is our case.

which suggests a good accuracy of the variational state also with respect to the expectation values of the operators  $O_k$ .

Let us remark that the stochastic reconfiguration method is very close to the steepest descent method. The main difference, which allows us to obtain a more stable algorithm, is that the stochastic reconfiguration method takes also into account the variation of the wave function. Indeed it is straightforward to show, by using the linear approximation (2.33), that Eq. (2.40) is equivalent to the Euler equation with the addition of a constraint related to the norm of the wave function, namely:

$$\frac{\partial [E_T(\alpha^0) - \lambda (\langle \Psi_T(\alpha^0) | \Psi_T(\alpha') \rangle - 1)]}{\partial \alpha_k^0} = 0, \quad (2.44)$$

where  $\lambda$  is a Lagrange multiplier that ensures that the norm of the two wave functions does not differ of a large quantity. The fact that we can change the parameters of a large amount, without changing notably the wave function, allows us to reach the minimum in a stable way, with fewer iterations.

Indeed, in the stochastic reconfiguration algorithm, the variations  $\delta\alpha_k$  are related not only to the forces, but also to the inverse covariance matrix  $\bar{S}^{-1}$ , namely, by writing Eq. (2.40) in vectorial notations:

$$\delta\alpha = \bar{S}^{-1} \bar{f}.$$

The diagonal elements of the reduced covariance matrix (2.42) give direct information about the fluctuations of the parameters  $O_k$ . The fact that each component of the force is multiplied by the inverse of the fluctuations allows us to move mainly along the directions where the variance of the corresponding operator  $O_k$  is small, i.e., where the signal-noise ratio is small. This avoids undesired instabilities due to the fluctuations of the stochastic system. Moreover, the presence of non-zero off-diagonal elements  $\bar{S}_{ij}$  allows us to move each parameter by taking into account all the other directions at the same time. Therefore, we reach the variational minimum being driven not only by the high-energy contributions, but also by the parameters which contribute at low energy.

The equations (2.40) are solved stochastically with the Monte Carlo algorithm. In practice, we perform  $M_{SR}$  Metropolis steps in order to calculate the expectation values of (2.41) and (2.42) and have small enough fluctuations. Then the linear system (2.40) is solved in order to find the variations  $\delta\alpha_k$ . Finally, once

the variations  $\{\delta\alpha_k\}$  are calculated, the variational parameters  $\{\alpha_k\}$  are modified according to:

$$\alpha'_k = \alpha_k^0 + \Delta \delta\alpha_k,$$

where  $\Delta$  is a number that can be tuned in order to control the change of the parameters. Generally one starts with a large  $\Delta$  in order to reach the minimum in few iterations, and consequently  $\Delta$  is decreased in order to reduce the fluctuations of the converged parameter. The new wave function  $|\Psi(\alpha')\rangle$  is then considered as the starting state  $|\Psi(\alpha^0)\rangle$  and the method is reiterated, until convergence is achieved.

Indeed, the stochastic nature of the system (2.40) implies that the forces  $\bar{f}_k$  are always determined with some statistical noise  $\eta_k$ , and by iterating the minimization procedure several times, even when the variational minimum is reached, the parameters will fluctuate around their mean values. Therefore, once convergence is reached, one must average over a certain number of iterations in order to find the optimal parameters that are close to the energy minimum. Indeed, in the case of a quadratic energy landscape, the averaged parameters correspond to the minimum energy. However, in many cases it is possible to have non-harmonic contributions, and the larger are the fluctuations, the larger is the bias that is introduced. Indeed, one can describe the evolution of the variational parameters during the minimization iterations by means of a standard Langevin dynamics. The statistical fluctuations are similar to the thermal noise of the Langevin equation:

$$\partial_t \alpha_k = f_k + \eta_k, \quad (2.45)$$

where the thermal noise is defined as:

$$\langle \eta_k(t) \eta_{k'}(t') \rangle = 2T_{noise} \delta(t - t') \delta_{k,k'}. \quad (2.46)$$

By increasing the number of sampled configurations  $T_{noise}$  diminishes, since the fluctuations are reduced, namely  $T_{noise} \propto M_{SR}^{-1}$ . Therefore, there is an optimal value of  $M_{SR}$ , which guarantees a fast convergence and avoids the parameters to be biased within the statistical accuracy of the sampling. Moreover, we find that the optimal  $M_{SR}$  also depends on the type of operators  $O_k$  included in the minimization, hence on the type of variational parameters to be minimized.

It is possible to introduce another appropriate iterative scheme for the minimization of the energy, based on the variational technique that in some case im-

prove the stochastic schemes. Indeed, by using a very efficient statistical evaluation of the first and second energy derivatives, it is possible to define a very rapidly converging iterative scheme (the Hessian minimization) that, within the variational Monte Carlo, is much more convenient than the standard Newton method. We refer to the original paper [102] for a detailed description of this method.

## 2.4 Green's Function Monte Carlo

### 2.4.1 Basic Principles: importance sampling

The Green's function Monte Carlo (GFMC) [103] is a stochastic technique that allows us to filter out the ground-state  $|\Phi_0\rangle$  of an Hamiltonian  $H$  from a trial wave function  $|\Psi_T\rangle$ , provided that  $\langle\Psi_T|\Phi_0\rangle \neq 0$ , by using the power method Eq. (2.1).

In practice we define a basis  $|x\rangle$  (e.g. the spin configuration of the lattice) and the iterative application of the Green's function  $G_{x',x}$  given by Eq. (2.1) reads

$$\Psi_{n+1}(x') = \sum_x G_{x',x} \Psi_n(x). \quad (2.47)$$

On large sizes it is not possible to evaluate exactly this recursive equation. Indeed, after few steps, the application of  $G$  generates transitions to a very large number of different states, implying a huge amount of memory occupation. Therefore an alternative approach is necessary. The solution is to sample in a statistical way the matrix-vector product (2.47) by defining a Markov process.

In order to implement efficiently the power method, it is convenient to consider not the original matrix  $G$ , but the slightly more involved non-symmetric one

$$\bar{G}_{x',x} = \frac{\Psi_G(x')}{\Psi_G(x)} G_{x',x}, \quad (2.48)$$

where  $\Psi_G(x)$  is the so-called *guiding wave function*. The convenience of using  $\bar{G}$  instead of  $G$  comes out from the following argument. If we consider  $\bar{G}$ , the local energy  $E_x$  is given by

$$E_x = \sum_{x'} \frac{\Psi_G(x')}{\Psi_G(x)} H_{x',x} = \sum_{x'} \bar{H}_{x',x}. \quad (2.49)$$

Thus if  $\Psi_G(x)$  is exactly equal to the ground-state of  $H$  then  $E_x = E_0$ , independently on  $x$ . This is the so called zero-variance property, namely if the guiding

wave function approaches an exact eigenstate of  $H$ , the method is free of statistical fluctuations. The guiding wave function has to be as simple as possible to be efficiently implemented in the calculation of the matrix elements and as close as possible to the ground-state of  $G$ . Moreover, it is easy to show that if  $\Phi_i(x)$  is an eigenvector of  $G$  with eigenvalue  $E_i$ , then  $\Psi_G(x)\Phi_i(x)$  is an eigenvector of  $\bar{G}$  with the same eigenvalue, i.e.  $G$  and  $\bar{G}$  have the same spectrum. It is worth noting that, after the importance sampling transformation (2.48), the iteration step (2.47), reads

$$\Psi_{n+1}(x')\Psi_G(x') = \sum_x \bar{G}_{x',x}\Psi_n(x)\Psi_G(x). \quad (2.50)$$

For simplicity, from now on the bar over an operator represents the same operator after the importance sampling transformation.

## 2.4.2 Statistical implementation of the power method by the many walker formulation

In order to define the statistical implementation of Eq. (2.50), we decompose the matrix  $\bar{G}_{x',x}$  in terms of three factors:

$$\bar{G}_{x',x} = s_{x',x}p_{x',x}b_x, \quad (2.51)$$

where  $s_{x',x}$  is the sign of  $\bar{G}_{x',x}$ ,  $b_x$  is a normalization factor and  $p_{x',x}$  is a *stochastic matrix*, i.e. it fulfills the conditions  $p_{x',x} \geq 0$  and  $\sum_{x'} p_{x',x} = 1$ .

The basic element of the stochastic process is the *walker*, which, in the simplest formulation, is defined by  $(x, w)$ , i.e. by its configuration in the lattice  $x$  and by a weight  $w$ . Stochastically, the iteration (2.50) is interpreted as a transition of the walker  $x \rightarrow x'$ , whereas the weight of the walker is scaled  $w \rightarrow w' = s_{x',x}b_xw$ . This scheme defines a Markov process in the walker space  $(x, w)$ . The basic idea of the stochastic implementation of Eq. (2.50) is that, although the number of non-zero elements of  $\bar{G}_{x',x}$  is of the order of the Hilbert space times the number of sites, the number of non-zero entries in each column is of the order of the number of sites. Therefore all the non-zero elements of  $\bar{G}_{x',x}$  for a fixed  $x$  can be computed, even for large size systems.

The previous Markov iteration allows us to define the evolution of the probability distribution  $P_n(w, x)$  to have a walker with weight  $w$  and configuration  $x$ ,

namely:

$$P_{n+1}(w', x') = \sum_x \frac{p_{x',x}}{b_x} P_n \left( \frac{w'}{b_x s_{x',x}}, x \right). \quad (2.52)$$

The first momentum of the probability distribution  $P_n(w, x)$  completely determines the wave function  $\Psi_n(x)$  of the power method (2.1)

$$\Psi_n(x) \Psi_G(x) = \int dw w P_n(w, x). \quad (2.53)$$

Indeed, it can be easily seen that the evolution (2.52) correctly reproduces the dynamics of the wave function, Eq. (2.50). Therefore, after an equilibration, the probability  $P_n(w, x)$  converges to its equilibrium limit  $P^*(w, x)$ , which defines the ground-state wave function

$$\Phi_0(x) \Psi_G(x) = \int dw w P^*(w, x). \quad (2.54)$$

Therefore, the ground-state energy is given by

$$E_0 = \frac{\langle \Psi_G | H | \Phi_0 \rangle}{\langle \Psi_G | \Phi_0 \rangle} = \frac{\sum_{x,x'} \bar{H}_{x',x} \int dw w P_0(w, x)}{\sum_x \int dw w P_0(w, x)}. \quad (2.55)$$

Using the fact that the local energy  $E_x = \sum_{x'} \bar{H}_{x',x}$ , we have that the ground-state energy  $E_0$  can be computed over a sample  $X$  of independent  $\mathcal{N}$  values of configurations

$$E_0 \simeq \frac{\sum_{(w,x) \in X} w E_x}{\sum_{(w,x) \in X} w}. \quad (2.56)$$

In addition, within the same Monte Carlo sampling, it is also possible to calculate the so-called *mixed averages* [103] of arbitrary linear operators  $O$ ,

$$\langle O \rangle_{\text{MA}} = \frac{\langle \Psi_G | O | \Phi_0 \rangle}{\langle \Psi_G | \Phi_0 \rangle}. \quad (2.57)$$

In fact, such mixed averages can be calculated using Eq. (2.56) by substituting the local energy  $E_x$  with the local estimator associated to the operator  $O$ , namely

$$O_x = \sum_{x'} \bar{O}_{x',x}. \quad (2.58)$$

where  $\bar{O}_{x',x}$  are the operator matrix elements transformed according to the guiding wave function.

In the practical implementation of the method, since the walker weights grow exponentially with the Markov iteration, the procedure for the statistical evaluation of the ground-state energy and the mixed averages is slightly different. We can consider that, after many iterations, the configuration  $x$ , generated in the Markov process, is distributed according to the maximum right eigenstate of the matrix  $p_{x',x}$ . This state is different from the state  $\Psi_G(x)\Phi_0(x)$  we are interested in, and we can consider it as a trial state in the power method. At any Markov iteration we can compute the weight of the walker assuming that  $L$  iterations before it was equal to 1. In this way the ground-state energy is given by

$$E_0 = \frac{\sum_n E_{x_n} G_n^L}{\sum_n G_n^L}, \quad (2.59)$$

where

$$G_n^L = \prod_{j=1}^L b_{x_{n-j}} s_{x_{n-j+1}, x_{n-j}}. \quad (2.60)$$

In principle, the previously described procedure is free from any approximation, and, it gives exact results within the statistical errors. Unfortunately there are two main technical problem. The first one is that the weight  $G_n^L$  grows exponentially by increasing  $L$ , implying a divergent variance in the energy average. Indeed  $G_n^L$  is a product of  $L$  different factors and it can assume very large or very small values. This problem has a simple solution by considering the GFMC technique with many walkers and by introducing a reconfiguration scheme, which enables to drop out the irrelevant walkers with small weights. Calandra and Sorella [104] have introduced a reconfiguration scheme working at fixed number of walkers, in a way that allows us to control the bias due to the finite walker population, which we will describe in the following.

The second problem is much more serious and it is related to the *sign problem*. It is due to the fact that the average sign,

$$\langle s_L \rangle = \frac{\sum_n G_n^L}{\sum_n |G_n^L|}, \quad (2.61)$$

vanishes exponentially with  $L$ . Indeed walkers with positive and negative weights cancel almost exactly, giving rise to an exponentially small quantity to sample, with huge fluctuations. In the following section we will introduce the fixed node technique that is an approximation that allow us to avoid the sign problem.

Let us focus on the first problem and, in order to show how the reconfiguration scheme works, let consider a case without sign problem, i.e. with  $s_{x',x} = 1$ . We consider  $M$  walkers and label the corresponding configurations and weights with a couple of vectors  $(\mathbf{x}, \mathbf{w})$ , with each component  $(x_i, w_i)$ ,  $i = 1, \dots, M$  corresponding to the  $i^{\text{th}}$  walker. It is easy to generalize Eq. (2.52) to many independent walkers

$$P_{n+1}(\mathbf{w}', \mathbf{x}') = \sum_{x_1, \dots, x_M} P_n \left( \frac{w'_1}{b_{x_1}}, \dots, \frac{w'_M}{b_{x_M}} \right) \frac{P_{x'_1, x_1} \cdots P_{x'_M, x_M}}{b_{x_1} \cdots b_{x_M}}. \quad (2.62)$$

Again, the wave function  $\Psi_n(\mathbf{x})$  is completely determined by the first momentum of the probability  $P_n(\mathbf{w}, \mathbf{x})$ , namely

$$\Psi_n(x) \Psi_G(x) = \int [\mathbf{d}\mathbf{w}] \sum_{\mathbf{x}} \frac{\sum_j w_j \delta_{x, x_j}}{M} P_n(\mathbf{w}, \mathbf{x}). \quad (2.63)$$

If the evolution of  $P_n(\mathbf{w}, \mathbf{x})$  is done without any restriction, we have that each walker is completely uncorrelated from the other

$$P_n(\mathbf{w}, \mathbf{x}) = \prod_{i=1, \dots, M} P_n(w_i, x_i). \quad (2.64)$$

In order to prevent the divergence of the weights, we define a reconfiguration process that changes the probability distribution without changing its first momentum, i.e. the wave function:

$$P'_n(\mathbf{w}', \mathbf{x}') = \int [\mathbf{d}\mathbf{w}] \sum_{\mathbf{x}} K(\mathbf{w}', \mathbf{x}', \mathbf{w}, \mathbf{x}) P_n(\mathbf{w}, \mathbf{x}), \quad (2.65)$$

where the kernel  $K(\mathbf{w}', \mathbf{x}', \mathbf{w}, \mathbf{x})$  is given by

$$K(\mathbf{w}', \mathbf{x}', \mathbf{w}, \mathbf{x}) = \prod_{i=1}^M \left( \frac{\sum_j w_j \delta_{x'_i, x_j}}{\sum_j w_j} \right) \delta \left( w'_i - \frac{1}{M} \sum_j w_j \right), \quad (2.66)$$

where the symbol  $\int [\mathbf{d}\mathbf{w}]$  indicates the  $M$  dimensional integral over the  $w_i$  variables.

In practice this reconfiguration process amounts to generate a new set of  $M$  walkers  $(\mathbf{x}', \mathbf{w}')$  in terms of the old  $M$  walkers  $(\mathbf{x}, \mathbf{w})$  in the following way: each new walker will have a weight  $\bar{w} = \frac{1}{M} \sum_j w_j$  and a new configuration  $x'_i$  among

the possible old ones  $x_j$ , chosen with a probability  $p_i = w_{j(i)} / \sum_k w_k$ . After this reconfiguration scheme, all the new walkers have the same weight and most of the irrelevant walkers with small weight are dropped out. Moreover it is easy to show that this kind of reconfiguration does not change the first momentum of the probability distribution [104].

### 2.4.3 Fixed node and Gamma Correction

When the weights of the walkers are not all positive it is always possible to define the transition probability for the stochastic process, but even if the Markov process converges to a probability distribution which determines the ground-state wave function, calculations are unstable due to wild cancellations between positive and negative weights. It is then necessary to consider some kind of approximation. The most popular one is the fixed node (FN) approximation [105]. In this approach an effective Hamiltonian is defined, starting from  $\bar{H}$ , by adding a perturbation  $O$ :

$$\mathcal{H}_{eff}^\gamma = \mathcal{H} + (1 + \gamma)O. \quad (2.67)$$

Here we follow [106] and introduce the external parameter  $\gamma$ , the original FN approximation [105] being recovered for  $\gamma = 0$ . The operator  $O$  is defined through its matrix elements and depends upon a given guiding function  $|\Psi\rangle$ , which in our case is the variational state  $|\Psi_{VMC}\rangle$ :

$$O_{x',x} = \begin{cases} -\mathcal{H}_{x',x} & \text{if } s_{x',x} = \Psi_{x'} \mathcal{H}_{x',x} \Psi_x > 0 \\ \sum_{y, s_{y,x} > 0} \mathcal{H}_{y,x} \frac{\Psi_y}{\Psi_x} & \text{for } x' = x, \end{cases} \quad (2.68)$$

where  $\Psi_x = \langle x | \Psi \rangle$ . One has to notice that the above operator annihilates the guiding function, namely  $O|\Psi\rangle = 0$ . Therefore, whenever the guiding function is close to the exact ground state of  $\mathcal{H}$  the perturbation  $(1 + \gamma)O$  is expected to be small and the effective Hamiltonian becomes very close to the original one.

Let us review the properties of the FN Hamiltonian in this scheme. Trivially, for  $\gamma = -1$ ,  $\mathcal{H}_{eff}^\gamma$  coincides with  $\mathcal{H}$ , as the perturbation vanishes. The most important property of this effective Hamiltonian is that for  $\gamma \geq 0$  its ground state  $|\Psi_0^\gamma\rangle$  can be efficiently computed by using the Green's function Monte Carlo technique [103, 104] (because  $\mathcal{H}_{eff}^\gamma$  is free from the sign problem), which allows one

to sample the distribution  $\Pi_x \propto \langle x|\Psi\rangle\langle x|\Psi_0^\gamma\rangle$  by means of a statistical implementation of the power method:  $\Pi \propto \lim_{n \rightarrow \infty} G^n \Pi^0$ , where  $\Pi^0$  is a starting distribution and  $G_{x',x} = \Psi(x')(\Lambda\delta_{x',x} - \mathcal{H}_{eff,x',x}^\gamma)/\Psi(x)$ , is the Green's function, defined with a large or even infinite [107] positive constant  $\Lambda$ ,  $\delta_{x',x}$  being the Kronecker symbol.

The statistical method is very efficient for  $\gamma \geq 0$ , since in this case all the matrix elements of  $G$  are non-negative and, therefore, it can represent a transition probability in configuration space, apart for a normalization factor  $b_x = \sum_{x'} G_{x',x}$ . In this case, it follows immediately that the asymptotic distribution  $\Pi$  is also positive and, therefore, we arrive at the important conclusion that for  $\gamma \geq 0$  the ground state of  $\mathcal{H}_{eff}^\gamma$  has the same signs of the chosen guiding function.

Within the FN approximation, we have a direct access to the ground-state energy  $E_{FN}^\gamma$  of the effective Hamiltonian by sampling the local energy  $e_L(x) = \langle x|\mathcal{H}|\Psi\rangle/\langle x|\Psi\rangle$  over the distribution  $\Pi_x$ . In the following, we will denote the standard FN energy for  $\gamma = 0$  simply by  $E_{FN}$ . It should be noted that, since  $O|\Psi\rangle = 0$ , we have that  $E_{FN}^\gamma$  is also the mixed average of the original Hamiltonian:

$$E_{FN}^\gamma = \frac{\langle \Psi_0^\gamma | \mathcal{H}_{eff}^\gamma | \Psi_0^\gamma \rangle}{\langle \Psi_0^\gamma | \Psi_0^\gamma \rangle} = \frac{\langle \Psi | \mathcal{H} | \Psi_0^\gamma \rangle}{\langle \Psi | \Psi_0^\gamma \rangle}. \quad (2.69)$$

$E_{FN}^\gamma$  gives a rigorous upper bound of the exact ground-state energy  $E_0 = E_{FN}^{\gamma=0}$  since it is an increasing function of  $\gamma$  as the operator  $O$  is positive definite <sup>6</sup> and by the Hellman-Feynman theorem:

$$\frac{dE_{FN}^\gamma}{d\gamma} = \frac{d\langle \mathcal{H}_{eff}^\gamma \rangle}{d\gamma} = \langle \frac{d\mathcal{H}_{eff}^\gamma}{d\gamma} \rangle = \langle O \rangle \geq 0, \quad (2.70)$$

here  $\langle \dots \rangle$  indicates the expectation value over  $|\Psi_0^\gamma\rangle$ . This upper bound is also certainly below or equal to the variational energy of the guiding function  $E = \langle \Psi | \mathcal{H} | \Psi \rangle / \langle \Psi | \Psi \rangle$ , since from  $O|\Psi\rangle = 0$  it follows that  $E$  is also the expectation value of the FN Hamiltonian over  $|\Psi\rangle$ , namely  $E = \langle \Psi | \mathcal{H}_{eff}^\gamma | \Psi \rangle / \langle \Psi | \Psi \rangle$ .

One of the advantages of having introduced the parameter  $\gamma$  is that it is possible to extract the expectation value of the original Hamiltonian  $\mathcal{H}$  over the FN state  $|\Psi_0^\gamma\rangle$ . Indeed, by applying Eq. (2.70), we have that:

$$E_{\Psi_0}^\gamma = \langle \mathcal{H} \rangle = \langle \mathcal{H}_{eff}^\gamma \rangle - (1 + \gamma) \frac{d\langle \mathcal{H}_{eff}^\gamma \rangle}{d\gamma}$$

---

<sup>6</sup>This has been shown in [105], by proving that  $\langle \Phi | O | \Phi \rangle \geq 0$  for any wave function  $|\Phi\rangle$

$$= E_{FN}^\gamma - (1 + \gamma) \frac{dE_{FN}^\gamma}{d\gamma}, \quad (2.71)$$

and therefore, by doing simulations for different values of  $\gamma$  to calculate numerically the derivative, it is possible to evaluate the expectation value of  $\mathcal{H}$  over the ground state of the FN Hamiltonian. Moreover, by using the definition (2.71) and the fact that  $E_{FN}^\gamma$  is a convex function [106], it turns out that:

$$\frac{dE_{\Psi_0}^\gamma}{d\gamma} = -(1 + \gamma) \frac{d^2 E_{FN}^\gamma}{d\gamma^2} > 0, \quad (2.72)$$

namely  $E_{\Psi_0}^\gamma$  is monotonically increasing with  $\gamma$ . A practical estimate of  $E_{\Psi_0}^{\gamma=0}$ , the best variational energy that can be obtained within a stable statistical method, can be worked out by performing two calculations for  $\gamma = 0$  and  $\gamma = \tilde{\gamma} > 0$  via:

$$\tilde{E}_{\Psi_0}^{\gamma=0} = E_{FN} - \frac{1}{\tilde{\gamma}} (E_{FN}^{\tilde{\gamma}} - E_{FN}). \quad (2.73)$$

$\tilde{E}_{\Psi_0}^{\gamma=0}$  certainly improves the standard FN upper bound of the energy and still  $\tilde{E}_{\Psi_0}^{\gamma=0} \geq E_{\Psi_0}^{\gamma=0}$ . This latter inequality follows from the convexity of  $E_{FN}^\gamma$ , implying that its first derivative at  $\gamma = 0$  is certainly larger or equal than the corresponding finite difference estimate. In order to obtain a compromise between having small enough statistical errors and a reasonable energy gain with respect to the mixed average of Eq. (2.69), we have computed  $\tilde{E}_{\Psi_0}^{\gamma=0}$  using  $\tilde{\gamma} = 1$  for obtaining our results that we will show in the following chapter.

## 2.4.4 Forward walking technique

The GFMC technique can be used with success to compute also correlation functions on the ground-state of  $H$ . In particular, it is simple to compute expectation values of operators that are diagonal in the working basis, so that  $O_{x,x'} = \delta_{x,x'} \langle x|O|x\rangle$ . By using GFMC, the configurations of the walkers are distributed as  $\Psi_G(x)\Phi_0(x)$ , however, in order to compute

$$\langle O \rangle = \frac{\langle \Psi_0 | O | \Psi_0 \rangle}{\langle \Psi_0 | \Psi_0 \rangle}, \quad (2.74)$$

a further work is required. To this purpose, the desired expectation value is written as

$$\langle O \rangle = \lim_{N, N' \rightarrow \infty} \frac{\langle \Psi_G | H^N O H^{N'} | \Psi \rangle}{\langle \Psi_G | H^{N+N'} | \Psi \rangle}. \quad (2.75)$$

From a statistical point of view, Eq. (2.75) amounts first to sample a configuration  $x$  after  $N'$  GFMC steps, then to measure the quantity  $\langle x|O|x\rangle$ , and finally to let the walker propagate forward for further  $N$  steps. In order to evaluate the stochastic average, an approach similar to that done for the energy is possible. In this case we have:

$$\langle O \rangle = \frac{\sum_n O^n G_n^L}{\sum_n G_n^L}, \quad (2.76)$$

where  $O^n$  is the average over the walker population of the operator  $O$  at the generation  $n$ , i.e.  $O^n = \frac{1}{M} \sum_j O_j^n$ , being  $O_j^n$  the value of the operator  $O$  on the configuration  $x_j$  of the  $j^{\text{th}}$  walker at the iteration  $n$ , and

$$G_n^L = \prod_{j=-N}^{L-1} \bar{w}_{n-j}. \quad (2.77)$$

Notice that the correcting factors  $G_n^L$  are different from the case of the energy. Indeed, in this case,  $G_n^L$  contain a further propagation of  $N$  steps as compared to the previous expression.

A further condition is necessary in order to control the bias in the forward walking technique. The set of measured values  $O_j^n$  with weight factors given by Eq. (2.77) has to be modified after each reconfiguration process occurring in the forward direction. In practice after each reconfiguration, we have to bookkeep only the values  $O_j^n$  of the observable that survive after the reconfiguration. Therefore, after each reconfiguration,  $O_i^{n'} = O_{j(i)}$ , for  $i = 1, \dots, M$  and the function  $j(i)$  describing the reconfiguration scheme has to be computed: the walker with index  $i$  assumes the configuration with index  $j(i)$  before the reconfiguration.

In order to implement recursively the forward walking, it is useful to store at each reconfiguration the integer function  $j_n(i)$  for each reconfiguration  $n$  and the value of  $O_i^n$  of the operator for each walker. Then it is possible to compute the relevant configurations contributing to the operator  $O$  after  $N$  reconfiguration steps by recursive application of the integer function  $j_n(i)$ .



# Chapter 3

## Phase Separation in the $2D$ $t-J$ model

### 3.1 Introduction

The possible existence of charge and spin inhomogeneities and their relevance for the low-temperature physics of cuprate superconductors is a long-standing problem, not yet completely clarified [26, 108]. In particular, the issue is twofold: on the one hand, one is interested in understanding the low-energy behavior of microscopic models and the possibility to have or not inhomogeneous phases in physically relevant regions; on the other hand, it is also important to clarify the possible relation between charge or spin inhomogeneities and the electronic pairing, which may lead to a high critical temperature for superconductivity.

The original interest in the role of these inhomogeneities dates back to the works by Emery and Kivelson [5, 44] and raised when neutron scattering experiments [109, 110] suggested the possible formation of conducting hole-rich regions separated from hole-poor ones with strong antiferromagnetic moments. Indeed, in most materials, the presence of a true phase separation (PS) instability is ruled out by the existence of the long-range Coulomb force that prevents the charge from accumulating in macroscopic regions<sup>1</sup>, only allowing the possibility

---

<sup>1</sup>To our knowledge, the only cuprates superconductor showing PS is  $La_2CuO_{4+\delta}$ , due to the presence of mobile apical oxygens atoms that can screen the Coulomb potential of the mobile charges in the  $CuO_2$  plane [46].

to have a mesoscopic charge segregation, i.e. charge density waves (CDW) or the celebrated stripes. In the last decade, a great number of direct and indirect pieces of evidence for such charge segregation have been presented in different cuprate and nickelate materials, stimulating theoretical investigations in simple microscopic models [26, 108]. Several authors addressed the possibility of the emergence of PS or CDW generating from the competition between the kinetic energy, which tends to delocalize charge carriers, and various local interactions (like, for instance, the on-site Coulomb repulsion, the antiferromagnetic superexchange, or the coupling with some local phonon), which instead tend to freeze electrons. Given the complexity of the strongly correlated problem, which contains different energy scales, it is very difficult to study its ground-state and low-energy properties. For instances, by considering mean-field approaches it is very easy to overestimate the tendency of charge segregation [111–114]. In this respect, a great advantage of the variational Monte Carlo (VMC) technique is that it allows one to consider highly correlated wave functions, which are well beyond a simple mean-field ansatz [68, 115, 116]. Then it would be very important to compare the validity of the ansatz considered with exact ground-state properties on fairly large system sizes, since the variational approach may fail, especially for low-energy properties. This comparison is possible only for bosonic nonfrustrated models by means of quantum Monte Carlo (QMC) projection techniques, but for fermion systems the so-called sign problem prevents one from reaching the exact zero temperature properties in a stable way. Nevertheless, very-well-established and efficient approximate approaches are known for fermionic system that considerably improve the quality of a given variational guess. For instance, the so-called fixed-node (FN) method, that we have described in detail in the previous chapter, allows one to obtain the lowest-energy state constrained to have the same signs of a given variational wave function. Therefore, the FN scheme provides a simple procedure to assess the stability of a particular variational wave function, its accuracy being related to the differences between its properties and the ones obtained with the improved FN state.

In this chapter, we will revisit the problem of the PS instability in the  $t - J$  model on the square lattice. This issue has been largely considered by several authors in the recent past [78, 117–122]. Although a great effort has been done, a general consensus for  $J/t \lesssim 0.6$  and small-hole doping  $\delta$  is still lacking.

For very large  $J/t$ , at small hole doping, the ground state is phase separated between undoped regions, with long-range antiferromagnetic correlations, and conducting hole-rich regions. The simple explanation is based on the fact that the magnetic gain in accumulating the holes in a given region of space is much larger than the loss of kinetic energy. Therefore, a phase-separated state will have a lower energy than a homogeneous one. By decreasing  $J/t$ , the situation is much less clear, since the magnetic gain becomes comparable with the kinetic one. Emery, Kivelson, and Lin [44], by using simple variational arguments, claimed that the ground state of the  $t - J$  model should phase separate for all values of antiferromagnetic coupling  $J$  and close to half filling. This claim was first confirmed by using a more sophisticated Monte Carlo technique [118], but then disclaimed by other authors, using slightly different Monte Carlo approaches and series expansions [119–122]. In particular, Calandra, Becca and Sorella, showed that, by filtering out the high-energy components of a projected BCS wave function, it was possible to obtain a homogeneous ground state for  $J/t \sim 0.4$  [121]. Later, this approach was questioned in Ref. [123], since it was noted that the ground state is still unstable against PS for very small hole doping, where the previous variational ansatz had technical problems. In particular, it has been shown that Monte Carlo results could indicate an instability for  $\delta \lesssim 0.05$ . Moreover, it was disappointing that it was not possible to define a stable variational wave function and that a homogeneous state was obtained only after the filtering procedure. From all the calculations done by different numerical techniques, it is now clear that, in any case, the  $t - J$  model for  $J/t \sim 0.5$  is on the verge of charge instabilities and both PS or CDW can be stabilized with small perturbations [124–126].

A key issue that was absent in the previous calculations and must be included in a correct description is the presence of antiferromagnetic correlations at low doping. Recently, by using a variational approach that contains both antiferromagnetism and  $d$ -wave pairing, Ivanov [78] suggested that antiferromagnetic ordering could enhance the instability towards PS. However, in his approach, the presence of an antiferromagnetic order parameter in the fermionic determinant without the presence of a Jastrow term to take into account spin fluctuations implies a wrong behaviour of the spin properties at small momenta, which in turn could also induce incorrect charge properties. In fact, by using, a spin-wave approach for the Heisenberg model, it has been shown [99] that an exceptionally

accurate description of the ground state is obtained by applying a long-range spin Jastrow factor to the classically ordered state. In the corresponding variational wave function, it is important that the Gaussian fluctuations induced by the jastrow term are orthogonal to the direction of the order parameter, in order to reproduce correctly the low-energy excitations. A simple generalization of this wave function was used to study the Hubbard model at half filling and for low doping [127]. On the other hand, it is well known [96, 128, 129] that a projected BCS state with  $d_{x^2-y^2}$  symmetry and no antiferromagnetic order provides an accurate wave function for the low-doping region of the  $t - J$  model and remains rather accurate in energy even at zero doping, where a magnetically ordered ground state is well established in two dimensions. Therefore, in order to have an accurate variational ansatz to describe lightly doped correlated insulators, it seems natural to include both antiferromagnetic correlations and electronic pairing [130].

Following these suggestions, we construct a very accurate variational wave function that describes an energetically stable homogeneous phase. Moreover, by considering the FN approach, we have strong evidence in favour of a homogeneous ground state for  $J/t \lesssim 0.7$  for all accessible hole doping.

Our results give support to the RVB description of the superconducting pairing solving an old debated question risen long time ago. From one side Kivelson and collaborators were convinced that superconductivity need CDW or stripes, which give the origin of pairing. In contrast to this argument Rice and Anderson supported the idea that the  $t-J$  model can show HTSC also with a homogeneous phase, supporting in this way the idea that the origin of pairing must be addressed to the RVB state. Our results show one more evidence that the RVB state gives the correct way for describing the properties of the HTSC.

This chapter is organized as follow: first of all we will present how is possible to study in a simple way the PS problem starting from the Maxwell construction; after that we will present our improved variational wave function; and at the end we will show our numerical results and finally we will draw our conclusions.

## 3.2 Maxwell construction for Phase Separation

Let us enter a little bit more in detail in the problem of a finite number of holes in an antiferromagnetic background. At finite hole doping there is competition be-

tween the kinetic energy, which favors a homogeneous delocalized state, and the interaction energy, which favors an inhomogeneous localized state. This competition may give rise to strong charge fluctuations and eventually to phase separation or charge density waves.

In order to gain insight into the possible charge inhomogeneities in the lightly doped  $t - J$  model, it is instructive to consider the case of two holes and  $J \gg t$ . In this limit the kinetic energy can be neglected, and the energy of a state with two widely separated holes is  $E = E_0 - 8BJ$ , where  $E_0$  is the energy of the uniform antiferromagnetic background and  $B$  is the antiferromagnetic energy per bond. By contrast the energy of a state with the two holes clustered together to form a pair is  $E = E_0 - 7BJ$  (see Fig. 3.1). A similar argument holds for a finite number of holes and therefore this simple variational calculation shows that, for very large values of  $J$ , the state in which the holes are segregated, leaving the rest of the system undoped, is favored over the uniform one. At finite  $t$  the loss in antiferromagnetic energy competes with the gain in kinetic energy, and it is not at all obvious if the homogeneous state should have higher energy or not.

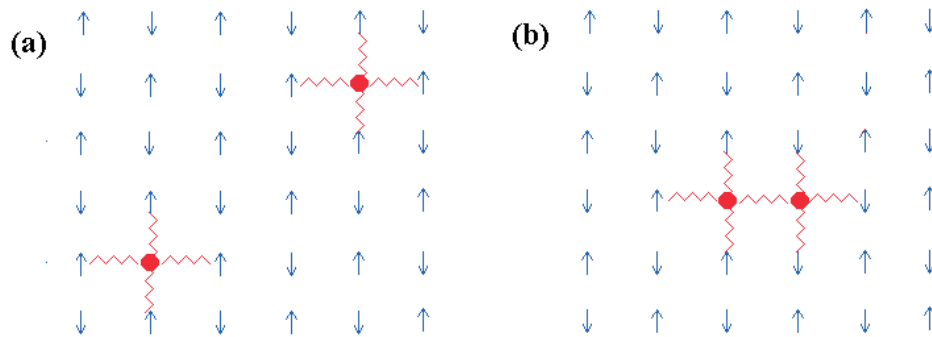


Figure 3.1: Two holes in an antiferromagnetic background. In the  $J \gg t$  limit, the energy loss with respect to the ordered state is given by number of broken bonds. If the holes are apart (a) the energy loss is  $8BJ$  whereas if they form a cluster (b) it is  $7BJ$ .

In the thermodynamic limit, the compressibility of a stable system is finite and positive. Since the compressibility can be related to the second derivative of the

energy per site  $e(\delta)$  with respect to the doping density  $\delta$

$$\chi = \left( \frac{\partial^2 e}{\partial \delta^2} \right)^{-1}, \quad (3.1)$$

it turns out that, in an infinite system, the stability criterium requires that the energy per site is a convex function of the density, see Fig. 3.2 (a). By contrast, if the compressibility is negative, the system phase separates, i.e. it creates two macroscopic regions with densities  $\delta_{c1}$  and  $\delta_{c2}$ . In this case, the energy of the homogeneous state can be lowered by forming two separated regions with different densities, being the total energy given by the Maxwell construction, see Fig. 3.2 (b).

In Ref. [44], a very clever way to detect phase separation by using energy calculations has been suggested. Assuming that, at a fixed hole doping  $\delta$ , the system is composed of a hole-free and a hole-rich phase, with density  $x$ , and assuming that the volume is large enough that the surface interaction can be neglected, the energy per site can be written in the form

$$e(\delta) = \min_x e(\delta, x) = \min_x \left\{ \left( 1 - \frac{L_x}{L} \right) e_0 + \frac{L_x}{L} e_x \right\}, \quad (3.2)$$

where  $L$  is the total number of sites,  $L_x$  is the number of sites in the hole-rich phase,  $e_0$  is the energy per site of the Heisenberg (hole-free) phase, and  $e_x$  is the energy per site of the uniform hole-rich phase, which is a function of  $x = N_h/L_x$ , with  $N_h$  number of holes, finally the hole density of the total system is  $\delta = N_h/L$ . For fixed values of  $N_h$  and  $L$ , i.e. for a given doping  $\delta$ ,  $e(\delta, x)$  is a function of  $L_x$ . The system phase-separates if  $e(\delta, x)$  has a minimum as a function of  $L_x$  at  $L_x < L$ . The energy per site can be rearranged into the form

$$e(\delta, x) = e_0 + \delta \epsilon(x), \quad (3.3)$$

where

$$\epsilon(x) = \frac{e_x - e_0}{x} \quad (3.4)$$

is the energy per hole in the uniform hole-rich region. Therefore phase separation occurs if  $\epsilon(x)$  has a minimum at finite  $x$ , see Fig. 3.2 (c) and (d). It is worth noting that, in the thermodynamic limit, if the system phase-separates,  $\epsilon(x)$  is a flat function of  $x$  for  $0 < x < \delta_c$ , whereas, in a finite size lattice, due to surface terms,  $\epsilon(x)$  can be slightly convex.

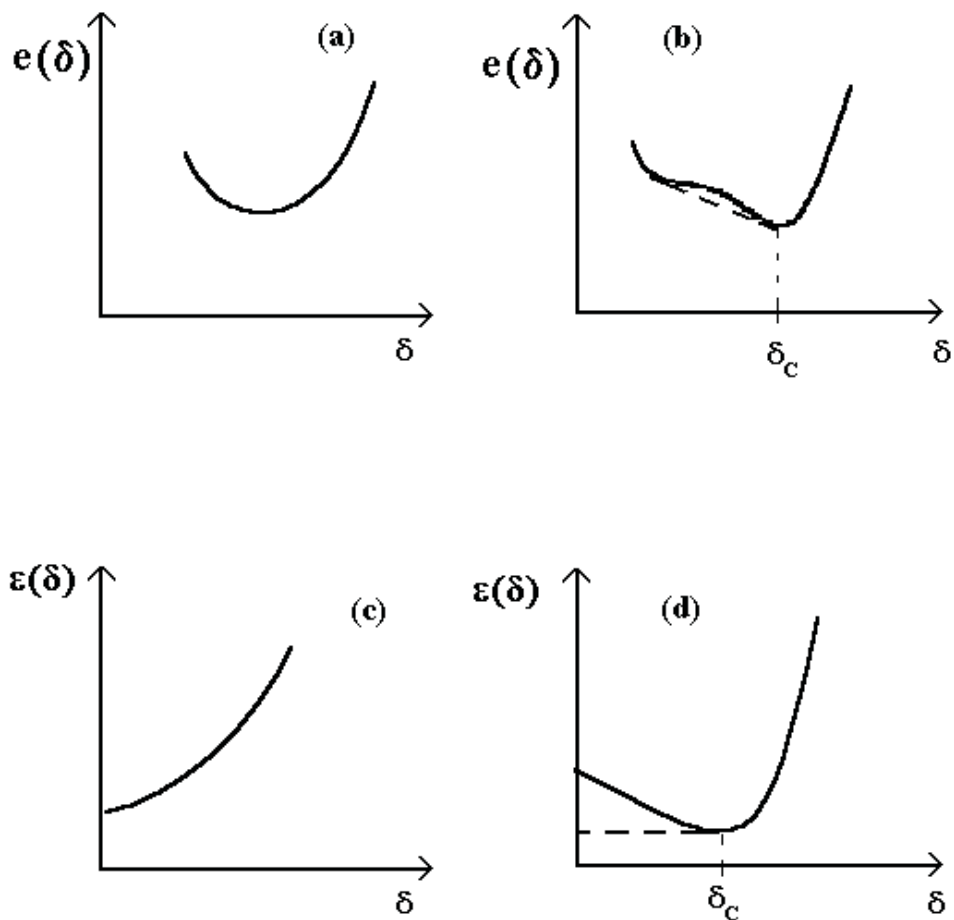


Figure 3.2: Energy per site landscape versus doping for a stable (a) and a phase separated (b) system. Energy per hole versus doping for a stable (c) and unstable (d) system. The dashed line is the Maxwell construction.

In their work, Emery and co-worker [44] claimed that, at low doping the ground-state of the  $t - J$  model is phase-separated for all the interaction strength  $J$ . Their statement was supported by an exact diagonalization on a small lattice cluster and by a variational calculation for  $J \ll t$ . Although the exact diagonalization results give insight into the physical properties of the cluster under consid-

eration, for fermion systems it is impossible to consider sizes with more than 32 sites and, for such small lattices, any size scaling in more than one dimension is highly questionable. Since the phase separation is a long-wavelength instability, it is crucial to consider large systems. Moreover, on small lattice and for low doping it is not easy to distinguish between phase separation and pairing. For example, for a 16-site lattice, the clustering of two holes can represent both pairing or phase separation at a doping of  $\delta \sim 0.12$ . Therefore, calculations with larger cluster size are needed.

By using quantum Monte Carlo and series expansion techniques, several authors have addressed the problem of finding out the critical value  $J_c$  above which there is phase separation at low doping in the  $t - J$  model [117–124, 131]. Although there is no general consensus on the value of  $J_c$ , most of the calculations agree that is between  $0.5t$  and  $1.2t$ . Different quantum Monte Carlo calculations [119–121, 131] agree with a  $J_c \sim 0.5t$ , by contrast in Refs. [118, 123] it was found that there is phase separation at all the interaction strengths. These discrepancies are probably due to the fact that in the latter work the different dopings are not achieved by varying the number of holes while keeping the lattice sizes constant, but by varying the lattice size while keeping the number of holes constant. Although this procedure probably overcomes the problems of having shell effects, it forces one to use fairly small size in the delicate low-doping region.

### 3.3 The $t - J$ model: variational approach

The  $t$ - $J$  model is defined by:

$$\mathcal{H} = -t \sum_{\langle i,j \rangle \sigma} \left( c_{i,\sigma}^\dagger c_{j,\sigma} + h.c. \right) + J \sum_{\langle i,j \rangle} \left( \mathbf{S}_i \cdot \mathbf{S}_j - \frac{1}{4} n_i n_j \right), \quad (3.5)$$

where  $\langle \dots \rangle$  indicates the nearest-neighbor sites,  $c_{i,\sigma}^\dagger$  ( $c_{i,\sigma}$ ) creates (destroys) an electron with spin  $\sigma$  on the site  $i$ ,  $\mathbf{S}_i = (S_i^x, S_i^y, S_i^z)$  is the spin operator,  $S_i^\alpha = 1/2 \sum_{\sigma,\sigma'} c_{i,\sigma}^\dagger \tau_{\sigma,\sigma'}^\alpha c_{i,\sigma'}$ , being  $\tau^\alpha$  the Pauli matrices, and  $n_i = \sum_{\sigma} c_{i,\sigma}^\dagger c_{i,\sigma}$  is the density operator.

We consider a square lattice with  $L$  sites and periodic boundary conditions rotated by 45 degrees such that  $L = 2l^2$  (tilted square lattice),  $l$  being an odd

integer, so that the non-interacting ground state is non-degenerate at half filling. Finally,  $J$  is the antiferromagnetic exchange constant and  $t$  the amplitude for nearest-neighbor hopping. In the following we will take  $t = 1$ .

### 3.3.1 Variational wave function: RVB projected WF

As pointed out by Gros [68], a very good variational wave function in the low doping regime is given by the projected  $d - wave$  BCS state

$$|\Psi_{RVB}^N\rangle = \mathcal{P}_N \mathcal{P}_G \Pi_k \left( 1 + f_k c_{k,\uparrow}^\dagger c_{-k,\downarrow}^\dagger \right) |0\rangle, \quad (3.6)$$

Where  $\mathcal{P}_N$  projects onto the subspace of  $N$  particles,  $\mathcal{P}_G$  is the Gutzwiller projector, which completely forbids doubly occupied sites, and  $f_k$  is the pair amplitude given by

$$f_k = \frac{\Delta_k}{\xi_k + \sqrt{\xi_k^2 + \Delta_k^2}}, \quad (3.7)$$

with  $\Delta_k = \Delta(\cos k_x - \cos k_y)$ ,  $\xi_k = -2t(\cos k_x + \cos k_y) - \mu$ ,  $\Delta$  being a variational parameter and  $\mu$  the chemical potential.

The non-projected wave function (3.6) can be obtained as the ground-state of the mean-field Hamiltonian

$$\mathcal{H}_{BCS} = \sum_k \xi_k c_{k,\sigma}^\dagger c_{k,\sigma} + \sum_k \Delta_k \left[ c_{k,\uparrow}^\dagger c_{-k,\downarrow}^\dagger + h.c. \right]. \quad (3.8)$$

It is worth noting that  $f_k$  is highly singular for a  $d - wave$  superconducting order parameter: it diverges along the diagonal directions for  $\xi_k < 0$ , i.e. inside the bare electronic Fermi surface. Therefore, it comes out that the wave function (3.6) is ill-defined on every finite cluster containing  $k - points$  along the diagonal direction. In order to avoid these singularities, it is useful to perform a particle-hole transformation on down-spin

$$d_i = (-1)^{R_i} c_{i,\downarrow}^\dagger \quad (3.9)$$

$$c_i = c_{i,\uparrow} \quad (3.10)$$

where  $R_i$  is the lattice's position of the  $i^{th}$  particle. After this transformation, the average number of electrons  $N$  is related to the difference between  $c$  and  $d$  particles as follows

$$N = \sum_i \left( \langle c_{i,\uparrow}^\dagger c_{i,\uparrow} \rangle + \langle c_{i,\downarrow}^\dagger c_{i,\downarrow} \rangle \right) = L + \sum_i \left( \langle c_i^\dagger c_i \rangle - \langle d_i^\dagger d_i \rangle \right), \quad (3.11)$$

whereas the average magnetization is given by

$$M = \sum_i \left( \langle c_{i,\uparrow}^\dagger c_{i,\uparrow} \rangle - \langle c_{i,\downarrow}^\dagger c_{i,\downarrow} \rangle \right) = -L + \sum_i \left( \langle c_i^\dagger c_i \rangle + \langle d_i^\dagger d_i \rangle \right). \quad (3.12)$$

After the particle-hole transformation, the wave function (3.6) can be written as

$$|\Psi_{RVB}^N\rangle = \tilde{\mathcal{P}}_N \tilde{\mathcal{P}}_G \Pi_k \left( u_k d_{k+Q}^\dagger + v_k c_k^\dagger \right) |\tilde{0}\rangle, \quad (3.13)$$

where  $\tilde{\mathcal{P}}_N$  and  $\tilde{\mathcal{P}}_G$  are the particle-hole transformed projectors  $\mathcal{P}_N$  and  $\mathcal{P}_G$ , respectively, while  $Q = (\pi, \pi)$ .

$$u_k = \sqrt{\frac{1}{2} \left( 1 + \frac{\xi_k}{\sqrt{\xi_k^2 + \Delta_k^2}} \right)} \quad (3.14)$$

$$v_k = \frac{|\Delta_k|}{\Delta_k} \sqrt{\frac{1}{2} \left( 1 - \frac{\xi_k}{\sqrt{\xi_k^2 + \Delta_k^2}} \right)} \quad (3.15)$$

and  $|\tilde{0}\rangle$  is the vacuum of  $c$  and  $d$  particles, i.e.  $c_k|\tilde{0}\rangle = d_k|\tilde{0}\rangle = 0$ , defined by  $|\tilde{0}\rangle = \Pi_k d_k^\dagger |0\rangle$ . In this case the singular points are occupied by the particles. It is worth noting that, if the magnetization is zero, the system is always at half-filling.

In order to improve this variational wave function, one can add to the wave function (3.15) a density-density Jastrow factor [132]

$$\mathcal{J}_d = \exp \left( \frac{1}{2} \sum_{i,j} u_{ij} n_i n_j \right). \quad (3.16)$$

Therefore, at the end the variational RVB projected wave function reads

$$|\Psi_{VMC}^{RVB}\rangle = \mathcal{J}_d |\Psi_{RVB}^N\rangle. \quad (3.17)$$

This wave function will be used in the following and represents the best non magnetic wave function at finite doping. In the next section, we will describe how to introduce antiferromagnetism (AF) and obtain a very accurate wave function in the low doping regime.

### 3.3.2 Improved variational wave function: PfaffianWF

Our improved variational ansatz is constructed by applying different projector operators to a mean-field state:

$$|\Psi_{VMC}^{Pfaff}\rangle = \mathcal{J}_s \mathcal{J}_d \mathcal{P}_N \mathcal{P}_G |\Psi_{MF}\rangle, \quad (3.18)$$

where,  $\mathcal{P}_G$  is the Gutzwiller projector that forbids double occupied sites,  $\mathcal{P}_N$  is the projector onto the subspace with fixed number of  $N$  particles,  $\mathcal{J}_s$  is a spin Jastrow factor

$$\mathcal{J}_s = \exp\left(\frac{1}{2} \sum_{i,j} v_{ij} S_i^z S_j^z\right), \quad (3.19)$$

being  $v_{ij}$  variational parameters, and finally  $\mathcal{J}_d$  is a density Jastrow factor

$$\mathcal{J}_d = \exp\left(\frac{1}{2} \sum_{i,j} u_{ij} n_i n_j\right), \quad (3.20)$$

being  $u_{ij}$  other variational parameters. The above wave function can be efficiently sampled by standard variational Monte Carlo, by employing a random walk of a configuration  $|x\rangle$ , defined by the electron positions and their spin components along the  $z$  quantization axis. Indeed, in this case, both Jastrow terms are very simple to compute since they only represent classical weights acting on the configuration.

The main difference from previous approaches is the presence of the spin Jastrow factor and the choice of the mean-field state  $|\Psi_{MF}\rangle$ , which includes both superconducting and antiferromagnetic order parameters. Actually,  $|\Psi_{MF}\rangle$  is taken as the ground state of the mean-field Hamiltonian

$$\begin{aligned} \mathcal{H}_{MF} = & \sum_{i,j,\sigma} t_{i,j} \left( c_{i,\sigma}^\dagger c_{j,\sigma} + h.c. \right) - \mu \sum_{i,\sigma} n_{i,\sigma} \\ & + \sum_{\langle i,j \rangle} \Delta_{i,j} \left( c_{i,\uparrow}^\dagger c_{j,\downarrow}^\dagger + c_{j,\uparrow}^\dagger c_{i,\downarrow}^\dagger + h.c. \right) + \mathcal{H}_{AF}, \end{aligned} \quad (3.21)$$

where, in addition to the BCS pairing  $\Delta_{i,j}$  (with d-wave symmetry), we also consider a staggered magnetic field  $\Delta_{AF}$  in the  $x$ - $y$  plane:

$$\mathcal{H}_{AF} = \Delta_{AF} \sum_i (-1)^{R_i} \left( c_{i,\uparrow}^\dagger c_{i,\downarrow} + c_{i,\downarrow}^\dagger c_{i,\uparrow} \right), \quad (3.22)$$

where  $\Delta_{AF}$  is a variational parameter that, together with the chemical potential  $\mu$  and the next-nearest-neighbor hopping of Eq. (3.21), can be determined by minimizing the variational energy of  $\mathcal{H}$  (3.5). This kind of mean-field wave function was first introduced by Bouchaud, Georges, and Lhuillier [133] and then used to study  $^3\text{He}$  systems and small atoms and molecules [134, 135]. Recently, it has been also used to study the  $t$ - $J$  model on the triangular lattice [136]. However, in these approaches the role of the long-range spin Jastrow factor was missed. We emphasize that, in the mean-field Hamiltonian (3.21), the magnetic order parameter is in the  $x$ - $y$  plane and not along the  $z$  direction like:

$$\mathcal{H}_{AF} = \Delta_{AF} \sum_i (-1)^{R_i} \left( c_{i,\uparrow}^\dagger c_{i,\uparrow} - c_{i,\downarrow}^\dagger c_{i,\downarrow} \right). \quad (3.23)$$

Indeed, as already mentioned at the beginning of this chapter, only in the case of Eq. (3.22), the presence of the spin Jastrow factor (3.19) can introduce relevant fluctuations over the mean-field order parameter  $\Delta_{AF}$ , leading to an accurate description of the spin properties. By contrast, if the Jastrow potential is applied to the mean-field ansatz (3.23), it cannot induce correct spin fluctuations and it is not efficient in lowering the energy.

Finally, as already shown in Ref. [96], the presence of the density Jastrow factor helps to reproduce the charge correlations of the superconducting regime, giving rise to the correct Goldstone modes.

The mean-field Hamiltonian (3.21) is quadratic in the fermionic operators and can be easily diagonalized in real space. Its ground state has the general form:

$$|\Psi_{MF}\rangle = \exp \left( \frac{1}{2} \sum_{i,j,\sigma_i,\sigma_j} f_{i,j}^{\sigma_i,\sigma_j} c_{i,\sigma_i}^\dagger c_{j,\sigma_j}^\dagger \right) |0\rangle, \quad (3.24)$$

the pairing function  $f_{ij}^{\sigma_i,\sigma_j}$  being an antisymmetric  $4L \times 4L$  matrix, i.e.  $f_{i,j}^{\sigma_i,\sigma_j} = -f_{j,i}^{\sigma_j,\sigma_i}$ . Notice that in the case of the standard BCS Hamiltonian, with  $\Delta_{AF} = 0$  or even with  $\Delta_{AF}$  along  $z$ , we have that  $f_{i,j}^{\uparrow,\uparrow} = f_{i,j}^{\downarrow,\downarrow} = 0$ , while in presence of

magnetic field in the  $x$ - $y$  plane the pairing function acquires non-zero contributions also in this triplet channel. The technical difficulty when dealing with such a state is that, given a generic configuration with definite  $z$ -component of the spin  $|x\rangle = c_{i_1, \sigma_1}^\dagger \dots c_{i_N, \sigma_N}^\dagger |0\rangle$ , we have that:

$$\langle x | \Psi_{MF} \rangle = Pf[F] = Pf \begin{pmatrix} f_{ij}^{\uparrow, \uparrow} & f_{ij}^{\uparrow, \downarrow} \\ f_{ij}^{\downarrow, \uparrow} & f_{ij}^{\downarrow, \downarrow} \end{pmatrix}, \quad (3.25)$$

where  $Pf[F]$  is the Pfaffian of the pairing function. See the Appendix, for more technical details on the Pfaffian and how it is used to describe our new variational wave function. It should be noticed that, whenever  $f_{i,j}^{\uparrow, \uparrow} = f_{i,j}^{\downarrow, \downarrow} = 0$ , the usual form of  $\langle x | \Psi_{MF} \rangle$  written in terms of a determinant is recovered.

The fact of dealing with Pfaffians makes the algorithm slower than the case of determinants, but the important point is that the algebra of Pfaffians still allows us to have a very efficient updating procedure in the Monte Carlo calculation. Then, by using the minimization technique described in Ref. [102], we are able to deal with a large number of variational parameters and in particular we can optimize all the independent coefficient  $v_{ij}$  and  $u_{ij}$ , beside the parameters contained in the mean-field Hamiltonian (3.21).

## 3.4 Results: Properties of the PfaffianWF and Phase Separation

### 3.4.1 Half-filled case

The inclusion of the magnetic field and the spin Jastrow factor strongly improves the energies with respect to the non-magnetic wave function. First we consider the half-filled case of a 26-site cluster, where the FN is *exact* (within the error-bars), i.e.,  $E_{FN}/L = -1.184450(2)$  (in unit of  $J = 1$ ) and also the variational energy is very good  $E_{VMC}/L = -1.18213(1)$ . On the other hand, although the signs of the non-magnetic wave function are correct (with the choice of  $t_{i,j}$  and  $\Delta_{i,j}$  connecting opposite sublattices and  $\mu = 0$ ), this state vanishes on many relevant configurations. This implies that, due to the importance sampling procedure described in the previous chapter, such configurations are never visited by the

Markov process, leading to  $E_{FN}/L = -1.1833(3)$ , despite the fact that the variational energy is not so poor  $E_{VMC}/L = -1.15334(1)$ . We also notice that in this case the FN is highly unstable and many walkers are needed to stabilize its convergence.

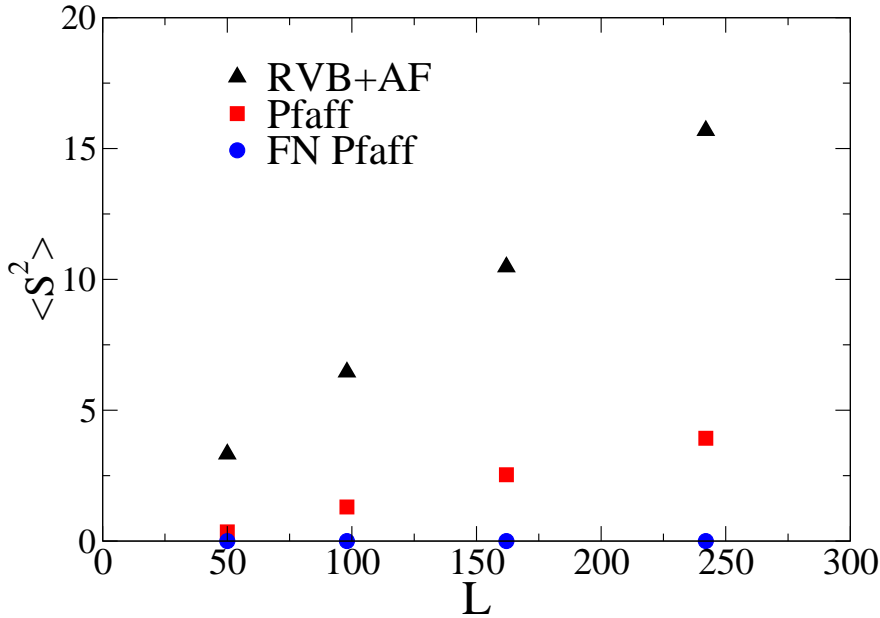


Figure 3.3: Results for the total spin  $\langle S^2 \rangle$  at half filling as a function of the cluster size  $L$  for the wave function of Eq. (3.18) defined by the mean-field Hamiltonian (3.21) and the two possible orientations of the magnetic field, i.e., Eqs. (3.22), indicated by “Pfaff”, and (3.23), indicated by “RVB+AF”. The FN results for the former case are also shown.

It is important to stress that the concomitant presence of the magnetic order parameter  $\Delta_{AF}$ , that breaks the  $SU(2)$  spin symmetry of the electronic part, and the spin Jastrow factor of Eq. (3.19), that also breaks the spin symmetry, gives rise to an almost symmetric state, even for large sizes. This can be verified by calculating the total spin  $S^2$ : In Fig. 3.3 we report the results for the two wave functions with magnetic order in the  $x$ - $y$  plane and along the  $z$  direction, usually

considered to describe the half-filled case and the lightly doped region [74, 78]. In the same figure, we also report the FN value of  $S^z$  (by using the former state as the guiding function) in order to show that a totally symmetric state is eventually recovered.

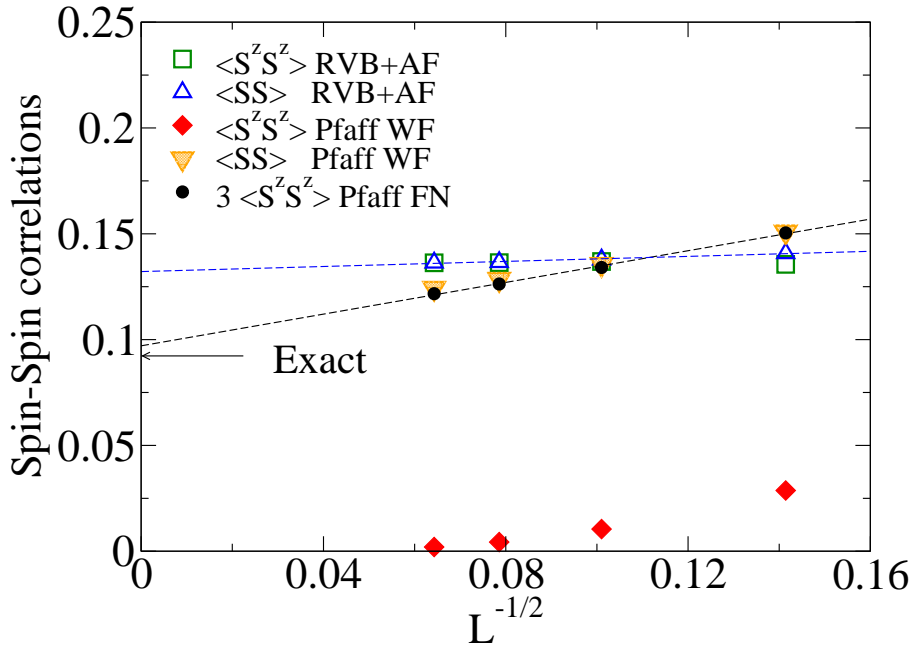


Figure 3.4: Spin-spin correlations at the maximum distance at half filling for the wave functions of Fig. 3.3. The exact value in the thermodynamic limit is marked by the arrow.

By a direct calculation of the spin-spin correlations at the maximum distance, we obtain that also the value of the magnetization at half filling is in a very good agreement with the exact result [104, 137], see Fig. 3.4. It should be noted that the variational wave function with the magnetization in the  $x-y$  plane and the spin Jastrow factor has very accurate isotropic spin-spin correlations, though in the  $z$  direction they decay to zero in the thermodynamic limit. By performing the FN approach (with  $\gamma = 0$ ), a finite value for the correlations along  $z$  is recovered. By contrast, when the magnetization is directed along  $z$  in the variational ansatz, the

spin correlations are almost Ising-like in the same direction and lead to overestimate the thermodynamic value of the magnetization, namely  $m \sim 0.37$ , instead of the well established value of  $m \sim 0.30$ , see Fig. 3.4.

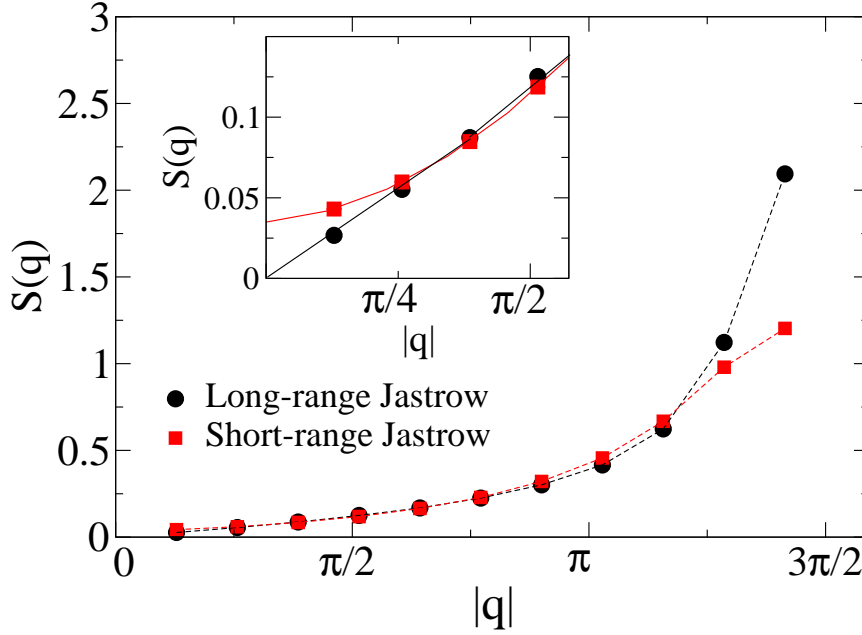


Figure 3.5: Spin structure factor  $S(q)$  at half filling for the variational wave function of Eq. (3.18) defined by the mean-field Hamiltonian of Eqs. (3.21) and (3.22) with long-range and short-range (i.e., nearest-neighbor) Jastrow factors. Inset: Detail for small momenta.

Finally, we want to stress that the long-range tail of the spin Jastrow factor, obtained by minimizing the energy and leading to  $v_q \sim 1/|q|$  for small  $|q|$  ( $v_q$  being the Fourier transform of  $v_{ij}$ ), is necessary to correctly reproduce the small- $q$  behavior of the spin-structure factor

$$S(q) = \frac{1}{L} \sum_{l,m} e^{iq(R_l - R_m)} S_l^z S_m^z. \quad (3.26)$$

Indeed, as it is clear from Fig. 3.5, only with a long-range spin Jastrow factor, it is possible to obtain  $S(q) \sim |q|$  for small momenta and, therefore, a gapless spin

Table 3.1: Ground state energy for 2 holes on 26 sites and different values of  $J/t$ . Two wave function with and without  $\Delta_{AF}$  are indicated with ‘‘Pfaff’’ and ‘‘RVB’’, respectively. The variational results are indicated by VMC and the Fixed-node ones by FN. In the last two columns we report the extrapolated value of Eq. (2.73) with the Pfaffian wave function and exact results by Lanczos method, respectively.

$J/t$	$E_{VMC}^{RVB}/L$	$E_{FN}^{RVB}/L$	$E_{VMC}^{Pfaff}/L$	$E_{FN}^{Pfaff}/L$	$\tilde{E}_{\Psi_0}^{\gamma=0}/L$	$E_{ex}/L$
0.3	-0.48334(1)	-0.49256(1)	-0.48476(1)	-0.49325(1)	-0.49445(2)	-0.50097
0.4	-0.57664(1)	-0.58625(1)	-0.57978(1)	-0.58770(1)	-0.58881(2)	-0.59452
0.5	-0.67045(1)	-0.68091(1)	-0.67568(1)	-0.68327(1)	-0.68434(3)	-0.68945
0.6	-0.76463(1)	-0.77645(1)	-0.77228(1)	-0.77960(1)	-0.78062(3)	-0.78537
0.8	-0.95410(1)	-0.96920(1)	-0.96706(1)	-0.97414(1)	-0.97505(3)	-0.97935
1.0	-1.14483(1)	-1.16385(1)	-1.16352(1)	-1.17052(1)	-1.17136(2)	-1.17538

spectrum. By contrast, with a short-range spin Jastrow term (for instance with a nearest-neighbor term),  $S(q) \sim \text{const}$ , for small  $q$ , that is clearly not correct.

### 3.4.2 Doped region

In order to show the accuracy of the wave function (3.18) in the doped region, we report in Table 4.1 and 3.2 the energies for 2 and 4 holes in 26 sites compared with the exact diagonalization data. In the same table we also show the results obtained from the wave function without the antiferromagnetic order parameter. Finally, we report the values of the extrapolated energies  $\tilde{E}_{\Psi_0}^{\gamma=0}$  given by Eq. (2.73). Also in these doped cases, the inclusion of the magnetic field with the spin Jastrow term substantially improves the accuracy of the non-magnetic wave function.

Let us move to the central issue of this chapter. In order to detect a possible PS instability, it is convenient to follow the criterion given in Ref. [44], described briefly at the beginning of this chapter, and consider the energy per hole:

$$e_h(\delta) = \frac{e(\delta) - e(0)}{\delta}, \quad (3.27)$$

where  $e(\delta)$  is the energy per site at hole doping  $\delta$  and  $e(0)$  is its value at half filling. For a stable system,  $e_h(\delta)$  must be a monotonically increasing function of  $\delta$ , since in this case the energy is a convex function of the doping and  $e_h(\delta)$  represents the

Table 3.2: The same as in Table 4.1 but for 4 holes on 26 sites.

$J/t$	$E_{VMC}^{RVB}/L$	$E_{FN}^{RVB}/L$	$E_{VMC}^{Pfaff}/L$	$E_{FN}^{Pfaff}/L$	$\tilde{E}_{\Psi_0}^{\gamma=0}/L$	$E_{ex}/L$
0.3	-0.61372(1)	-0.62752(1)	-0.61478(1)	-0.62754(1)	-0.62958(3)	-0.64262
0.4	-0.68894(1)	-0.70101(1)	-0.68946(1)	-0.70106(1)	-0.70292(2)	-0.71437
0.5	-0.76461(1)	-0.77571(1)	-0.76512(1)	-0.77595(1)	-0.77770(4)	-0.78812
0.6	-0.84065(1)	-0.85132(1)	-0.84170(1)	-0.85189(1)	-0.85348(3)	-0.86337
0.8	-0.99361(1)	-1.00476(1)	-0.99709(1)	-1.00659(1)	-1.00806(2)	-1.01733
1.0	-1.14760(1)	-1.16072(1)	-1.15479(1)	-1.16422(1)	-1.16566(3)	-1.17493

chord joining half filling and the doping  $\delta$ . On the other hand, the PS instability is marked by a minimum at a given  $\delta_c$  on finite clusters, and a flat behavior up to  $\delta_c$  in the thermodynamic limit where the Maxwell construction is implied.

Firstly, Fig. 3.6 shows the results of  $e_h(\delta)$  for different ratios  $J/t$  on the 26-site cluster, where the exact data are available by the Lanczos method. Although these data are already contained in tables 4.1 and 3.2, their graphical representation better shows our accuracy to estimate the slope of the energy per hole. In particular, we stress the fact that, even though already the variational results of the wave function (3.18) are very accurate, there is a strong improvement by considering the FN approach, both in the mixed average of Eq. (2.69) and in the extrapolation of Eq. (2.73), for which a perfect estimation of the slope is obtained.

Then we can move to large cluster to extract the thermodynamic properties. We report in Fig. 3.7 the results of the energy per hole for  $J/t = 0.4$ . For comparison, the FN calculations for  $\gamma = 0$  are performed by using two different guiding functions, including or not the antiferromagnetic order parameter and the spin Jastrow factor. At large doping the results are independent on the choice of the guiding state, clearly indicating that the antiferromagnetism is not essential in that region. However, by decreasing the hole concentration, the inclusion of the antiferromagnetic order becomes crucial for the stabilization of the homogeneous phase, whereas the simple projected BCS state is eventually unstable at small doping. This latter outcome actually is in agreement with our previous calculations [121] and confirms what has been noticed by Hellberg and Manousakis [123] and interpreted as an evidence for PS close to the insulating limit.

By contrast, our present FN results, based on the wave function with antifer-

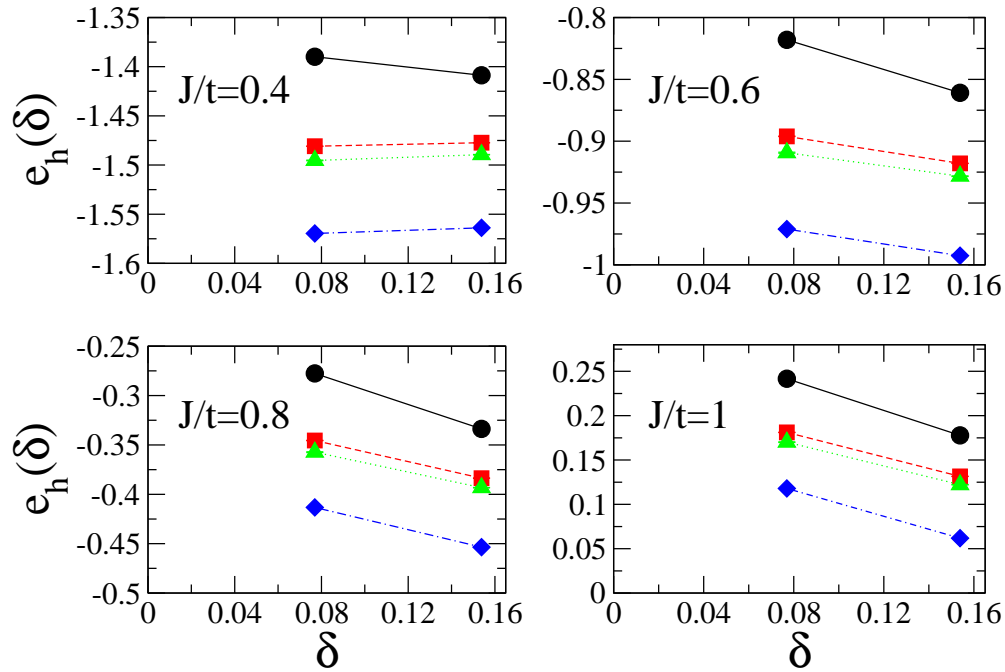


Figure 3.6: Energy per hole  $e_h(\delta)$  as a function of the doping  $\delta$  for the 26-site cluster calculated by different approaches: The variational calculations for the Pfaffian wave function (circles), the FN approach of Eq. (2.69) (squares), and the expectation value of the Hamiltonian over the FN ground state given by Eq. (2.73) (triangles); the exact results are also shown (diamonds).

romagnetic fluctuations, strongly improve the accuracy of previous calculations for small doping and point towards the stability of the homogeneous phase for all hole concentrations. Quite impressively, the energies are very accurate on the whole doping regime analyzed and there is not a qualitative difference if one considers the expectation value of the Hamiltonian (2.73), see Fig 3.7. These results indicate that the ground state is stable for all the hole concentrations, namely down to  $\delta \sim 0.01$  (i.e., two holes on 242 sites). Remarkably, also the variational wave function is stable for such value of the super-exchange interaction and small

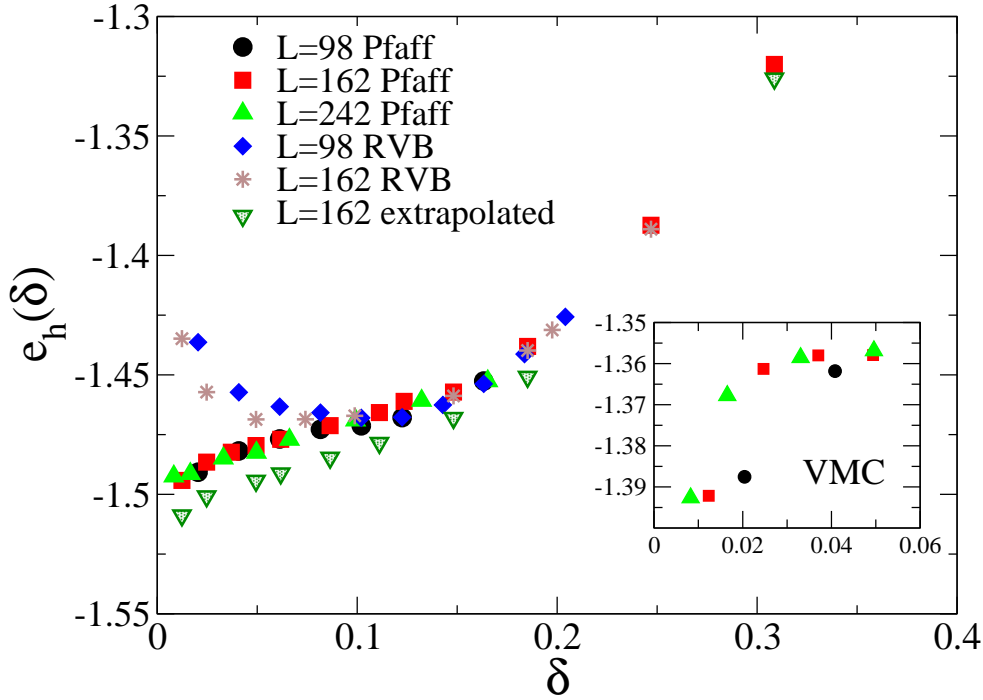


Figure 3.7: Energy per hole  $e_h(\delta)$  as a function of the doping  $\delta$  for  $J/t = 0.4$  and different sizes. The results are obtained by using the FN approach described in the text. Two different states are used as guiding function: The simple non-magnetic state, denoted by “RVB” and the state with pairing, antiferromagnetism in the  $x$ - $y$  plane, and the spin Jastrow factor, denoted by “Pfaff”. The expectation value of the Hamiltonian over the FN ground state are also shown for  $L = 162$  for the latter case. Inset: Variational results of  $e_h(\delta)$  for the Pfaffian wave function.

hole concentrations, see the inset of Fig 3.7. To our knowledge, this is the first successful attempt to obtain a variational state which is clearly stable towards the formation of regions with segregated holes, when approaching the Mott insulating regime.

From the energy calculation it is straightforward to estimate the compressibil-

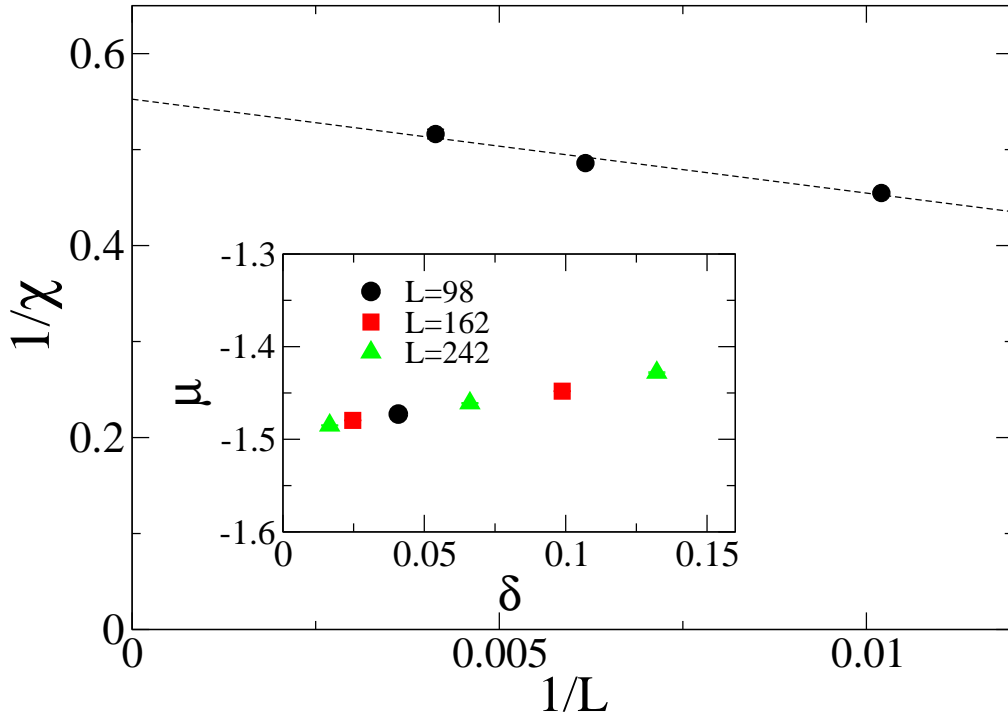


Figure 3.8: The inverse compressibility of the half-filled Mott insulator for  $J/t = 0.4$  calculated by extracting the second derivative of the polynomial fit of the FN energy. Inset: The chemical potential, defined through the difference of ground-state energies, as a function of the doping for different sizes of the cluster.

ity  $\chi$  for  $\delta \rightarrow 0$ :

$$\chi^{-1} = \frac{\partial^2 e(\delta)}{\partial \delta^2}. \quad (3.28)$$

Recently, Imada and coworkers [138, 139], by using hyper-scaling arguments and numerical simulations on the Hubbard model, proposed that the compressibility must diverge when the insulating phase is approached by decreasing the doping concentration. Their arguments imply that  $e(\delta) \sim \delta^3$  for small doping, as in the one-dimensional case, where the charge properties can be simply understood by considering spinless fermions. Instead, within our FN approach, we find that the

compressibility stays finite up to half filling. Indeed, for  $J/t = 0.4$  and in general for the stable magnetic phase, the variational calculation provides a finite compressibility that is further decreased by the more accurate FN approximation. It should be noticed that a much larger compressibility, or even an infinite one, could be worked out when considering only small size calculations, like the ones used in Ref. [138] to obtain  $\chi \sim |\mu - \mu_c|^{-1/2} \sim \delta^{-1}$  (where  $\mu$  is the chemical potential and  $\mu_c$  is nothing but the charge gap at half filling): In this case, it is possible to underestimate the slope of the energy at small doping and, therefore, also to overestimate the value of  $\chi$ . Instead, from our large cluster calculations, we have a clear evidence that the chemical potential is linear with the doping close to half filling or, equivalently, that  $e(\delta) \sim \delta^2$ , implying a finite compressibility when  $\delta \rightarrow 0$ , see Fig. 3.8. Our calculations are rather robust and do not depend upon the number of holes considered and a very accurate polynomial fit of the energy turns out to be very stable. We argue that the infinite compressibility scenario proposed by Imada and coworkers could be correct when the antiferromagnetism does not play an important role and the undoped system is a spin liquid with no magnetic order. This is also supported by dynamical mean-field theory calculations by Kotliar and coworkers [140] on the Hubbard model, where the mean-field solution without an antiferromagnetic order parameter leads to a diverging compressibility close to the Mott regime.

By increasing the antiferromagnetic super-exchange, we come closer to the PS region. Indeed, for  $J/t = 0.6$  we obtain that the energy per hole  $e_h(\delta)$  shows a slightly non-monotonic behavior with a minimum for  $\delta_c \sim 0.17$ , when considering the FN energies. This minimum disappears by performing the extrapolation of Eq. (2.73) to estimate the expectation value of the  $t$ - $J$  Hamiltonian over the FN ground state, see Fig. 3.9. This fact would indicate that, for this value of  $J/t$ , the FN Hamiltonian (2.67) has an higher tendency towards PS than the original  $t$ - $J$  model. In this case, the mixed average of Eq. (2.69) is slightly biased, and this bias can be eliminated by considering the actual expectation value of the  $t$ - $J$  Hamiltonian over the FN ground state. In doing this, we approach the exact result (by improving the energy) and an homogeneous phase, with a monotonically increasing energy per hole, is obtained. Within this more accurate scheme, we substantially improve previous results which were based on the mixed average of the FN approximation and indicated a rather high critical doping [121]. Unfortu-

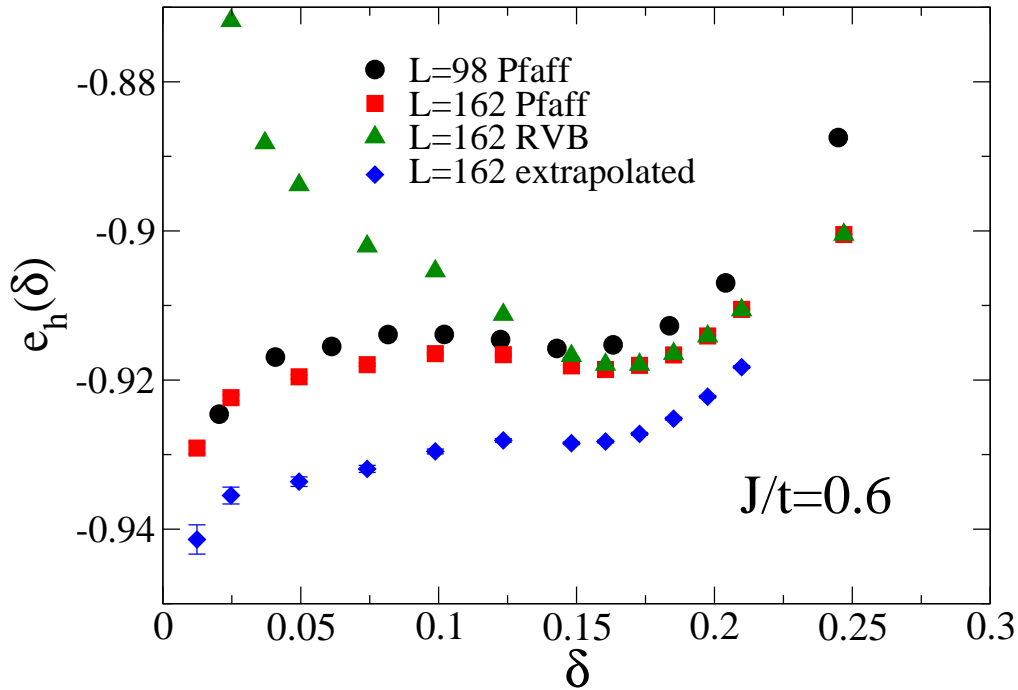


Figure 3.9: The same as in Fig. 3.7 for  $J/t = 0.6$ .

nately, within our numerical approach, it is very difficult to study the possible formation of hole droplets close to the PS instability, as suggested by Poilblanc [141]. Indeed, this would require a very delicate size scaling of the binding energy of few holes, which is beyond our present possibilities.

By further increasing the super-exchange coupling, we eventually enter into the PS region: For  $J/t = 0.8$ , the energy per hole has a rather deep minimum at finite doping and also the expectation value (2.73) clearly indicates a non-monotonic behavior, see Fig. 3.10.

Finally, it is important to stress that very similar results can be also obtained by considering the density-density correlation function

$$N(q) = \frac{1}{L} \sum_{l,m} e^{iq(R_l - R_m)} n_l n_m. \quad (3.29)$$

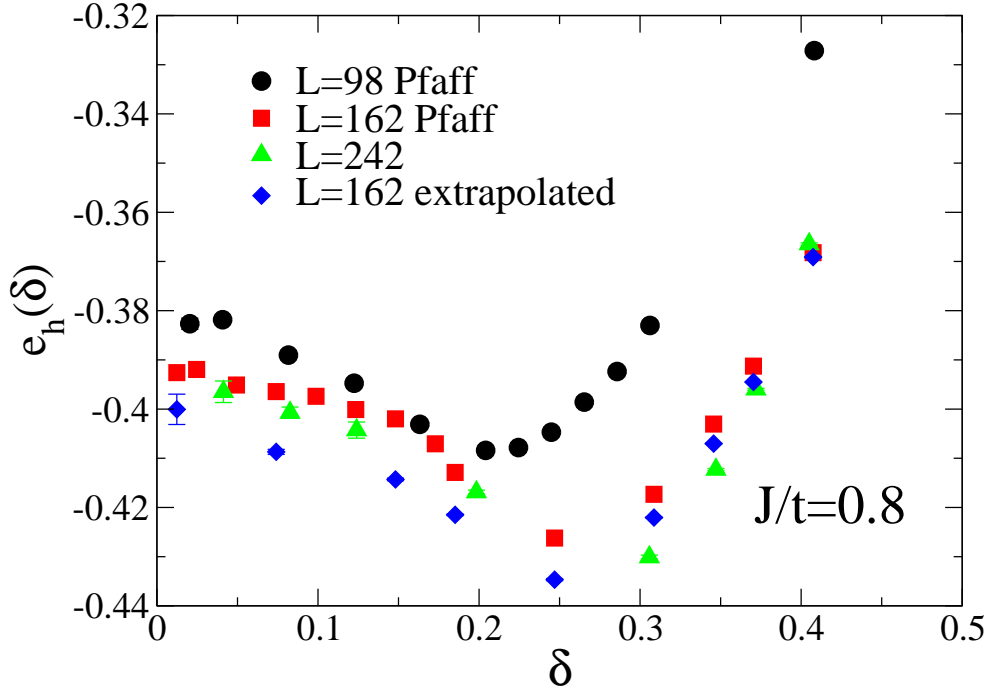


Figure 3.10: The same as in Fig. 3.7 for  $J/t = 0.8$ .

In this case, since  $N(q)$  is a diagonal operator in the configuration space, it is easy to compute its average value over the FN ground state by using the so-called forward-walking technique [104]. This quantity is therefore free from possible bias coming from mixed averages. The PS instability is signaled by the divergence at small momenta of  $N(q)$ . In a previous paper of Calandra, Becca and Sorella [121], was reported the calculations of this quantity, showing the presence of a finite- $q$  peak, linearly depending upon the doping, close to the PS instability. Here, thanks to the accuracy of the guiding function and the progress in stabilizing the statistical implementation of the FN technique, we are able to present much more accurate results that confirm the previous ones. Indeed, the existence of this peak is due to the closeness of the PS: Figs. 3.11 and 3.12 show the evolution of  $N(q)$  by increasing  $J/t$  for two values of the doping, near the insulating

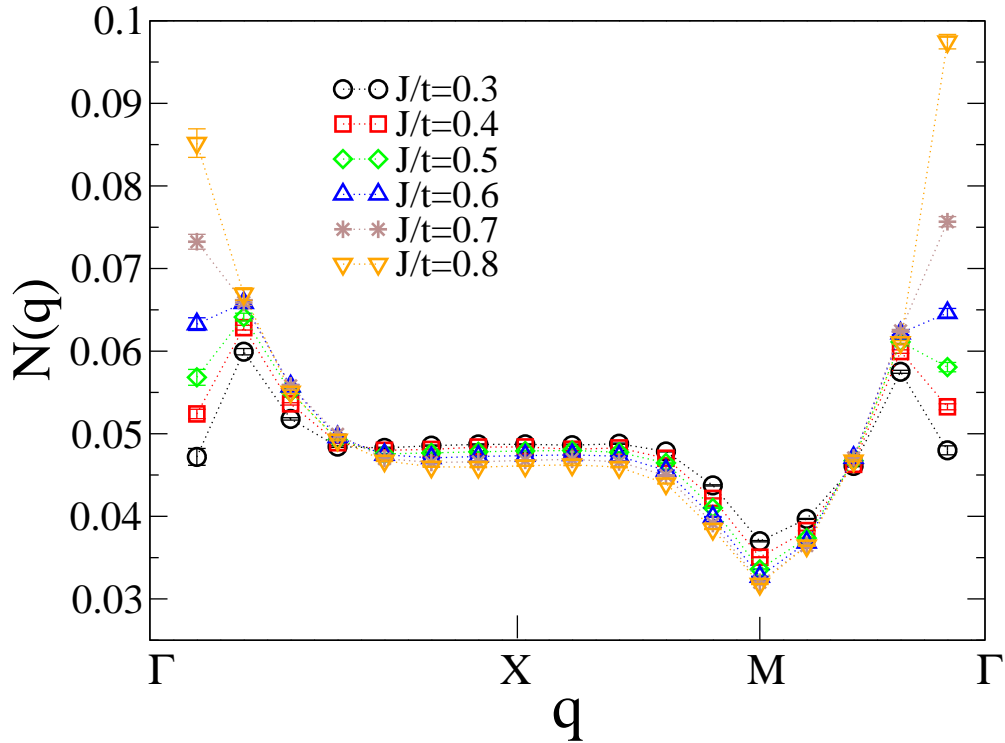


Figure 3.11: FN results for the density correlation function for 8 holes on 162 sites and different values of  $J/t$ . The high-symmetry points are marked as  $\Gamma = (0, 0)$ ,  $X = (\pi, \pi)$ , and  $M = (\pi, 0)$ .

regime. In particular, we obtain the evidence for a stable homogeneous phase for  $J/t \sim 0.4$ , confirming the indications given by the analysis based upon the energy per hole. Then also the progressive development of a huge peak around  $q = (0, 0)$  for  $J/t \sim 0.7$  is in good agreement with the energy calculations.

All together, these results allow us to draw our final phase diagram of Fig. 3.13, where we report, for comparison, also some of the previous estimations for the PS boundaries.

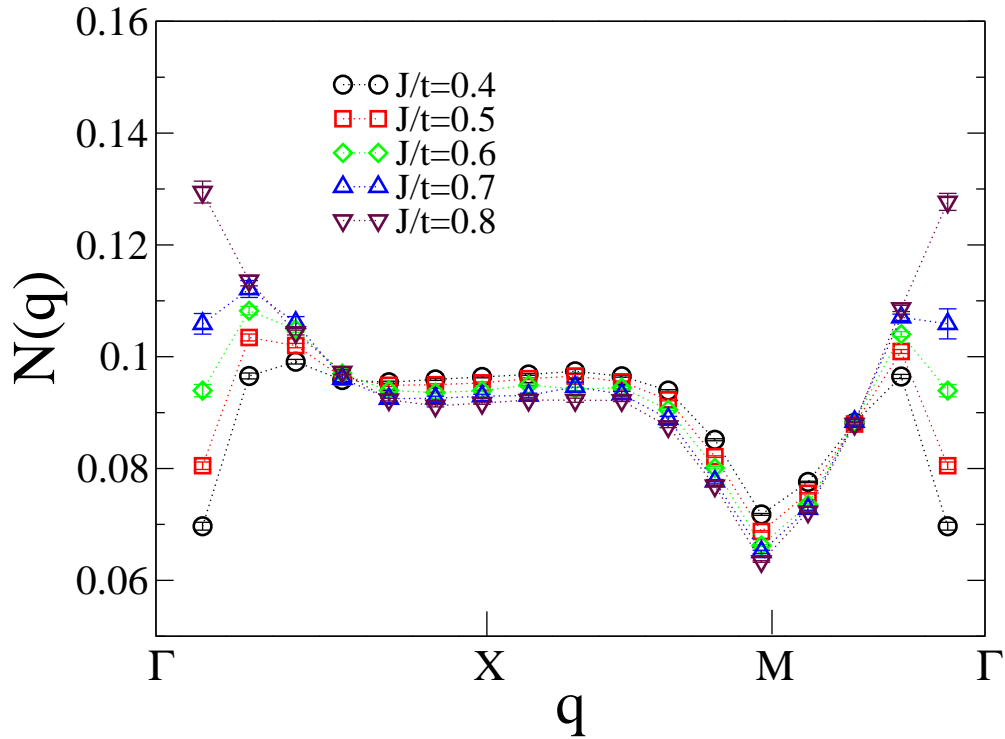


Figure 3.12: The same as in Fig. 3.11 but for 16 holes on 162 sites.

### 3.5 Conclusion

We have revisited the problem of the PS instability in the  $t-J$  model. By generalizing the Pfaffian wave function introduced some time ago [133], we have defined a very accurate variational state that, for the first one to our knowledge, is stable against PS at low doping. In particular, we have shown the necessity to consider both an antiferromagnetic order parameter (in the fermionic determinant) and a spin Jastrow factor, to mimic the spin fluctuations. In this way all the low-energy properties of the exact ground state are correctly reproduced. Then, by using a more sophisticated Monte Carlo technique that can filter out the high-energy components of a given trial wave function, we can obtain the ground state

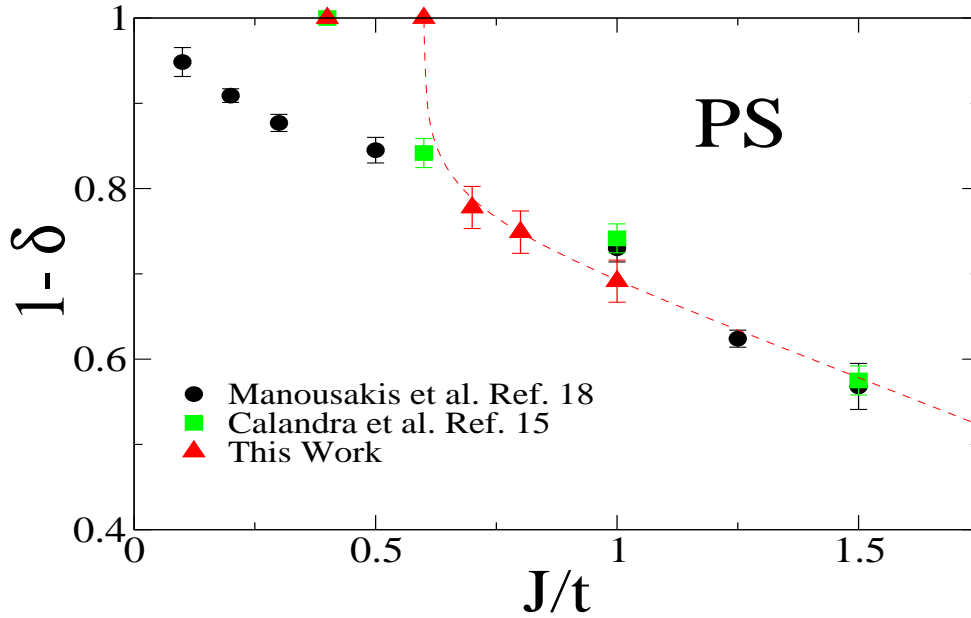


Figure 3.13: Boundary for the phase separation (PS) instability. The results of previous works are also shown for comparison. The line is a guide to the eye.

of an effective Hamiltonian and, at the same time, assess the stability of our initial guess. So, we have shown that for  $J/t = 0.4$ , the ground state does not phase separate at any hole doping down to  $\delta \sim 0.01$ , giving a serious improvement on the possible PS boundaries at small  $J/t$ . Remarkably, the analysis based on the energy per hole is also corroborated by the calculation of the static density-density correlations. The phase separation, in the low doping region, appears at a critical antiferromagnetic coupling slightly larger than the value given in Ref. [121], namely here we find  $J_c/t \sim 0.7$ . Although future improvements in the Monte Carlo technique or in the accuracy of the variational wave function may lead to an higher coupling, it looks unlikely to reach the critical point recently obtained by high-temperature expansion, i.e.,  $J_c/t \sim 1.2$  [117, 122]. In fact, as shown in Fig. 3.6, our present accuracy in the energy per hole is about  $0.05t$  and its slope is almost correct. This holds rather independently of  $J/t$  and system sizes, at least

for the clusters where exact results are available. For  $J/t = 0.8$  (see Fig. 3.10), the minimum of the energy per hole implies an energy gain for the inhomogeneous phase of about  $0.05t$  per hole, i.e., comparable with our maximum possible error estimated before. Thus we expect that  $J_c/t$  cannot be much larger than 0.8 even for a numerically exact method.

Moreover, we do not expect that different variational wave functions (used as guiding states for the FN approach) can strongly modify our results. Indeed, for the simple  $t$ - $J$  model of Eq. (3.5) there are strong evidences that, for  $\delta \lesssim 0.4$  and  $J/t$  between 0.2 and 0.7, the best variational state is given by projecting a state with electron pairing (and possibly a finite antiferromagnetic order). Different choices for the wave function, containing for instance flux phases or stripes, have higher energies and they become competitive only when additional interactions, like a next-nearest-neighbor Coulomb repulsion, or different topologies of the Fermi surface are considered in the microscopic Hamiltonian [125, 142, 143].

Finally, we have obtained that, in contrast with what was found in the Hubbard model, the compressibility stays finite by approaching the Mott insulator. A simple explanation of a finite compressibility in two dimensions is obtained by assuming that the holes form hole pockets around the nodal points [i.e.,  $q = (\pm\pi/2, \pm\pi/2)$ ] and behave as spinless fermions, implying that  $e(\delta) \simeq \delta^{1+2/D}$ , where  $D$  is the spatial dimension. In this simple scenario the compressibility is divergent only in one dimension, whereas it is finite in two dimensions, and should approach zero in three dimensions, leading to a more conventional metal-insulator transition.

The stability against phase separation of a wave function with explicit antiferromagnetism and d-wave superconducting order parameter provides new insight for understanding the phase diagram of the high-temperature superconductors. Remarkably, in the clean system, possibly idealized by the  $t$ - $J$  model, the antiferromagnetism and the d-wave order parameter should not exclude each other, at least at the variational level, and actually cooperate to decrease the energy and lead to a stable homogeneous phase.

# Chapter 4

## Magnetism and superconductivity in the $t-t'-J$

### 4.1 Introduction

As already discussed in the first chapter, after more than twenty years from the discovery of high-temperature superconductivity, a comprehensive description of the cuprate materials is still lacking. One of the main concern is about the origin of the electron pairing, namely if it is due to electron-phonon coupling, like in the standard theory by Bardeen, Cooper and Schrieffer (BCS) [2], or it can be explained by alternative mechanisms, based on the electronic interaction alone. From one side, though the isotope effect in cuprates (if any) is much smaller than the one observed in BCS superconductors, there are experiments suggesting a strong coupling between electrons and localized lattice vibrations [144, 145]. On the other side, besides a clear experimental outcome showing unusual behaviors in both metallic and superconducting phases, there is an increasing theoretical evidence that purely electronic models can indeed sustain a robust pairing, possibly leading to a high critical temperature [96, 146, 147]. Within the latter scenario, the minimal microscopic model to describe the low-energy physics has been proposed to be the Hubbard model or its strong-coupling limit, namely the  $t-J$  model, which includes an antiferromagnetic coupling between localized spins and a kinetic term for the hole motion [57, 58]. Anderson proposed that electron pairing could naturally emerge from doping a Mott insulator, described by a resonating valence

bond (RVB) state, where the spins are coupled together forming a liquid of singlets [57]. Indeed, subsequent numerical calculations for the  $t-J$  model [68], showed that, though the corresponding Mott insulator (described by the Heisenberg model) has magnetic order, the RVB wave function with d-wave symmetry in the electron pairing can be stabilized in a huge region of doping close to the half-filled insulator. These calculations have been improved by studying the accuracy of such a variational state, giving solid and convincing arguments for the existence of a superconducting phase in the  $t-J$  model [96]. However, other numerical techniques, like Density Matrix Renormalization Group, provided some evidence that charge inhomogeneities can occur at particular filling concentrations. These stripes are probably enhanced by the strong anisotropic boundary conditions used in this approach [50, 125, 126].

Coming back to the projected RVB wave function, it is worth mentioning that an approximate and simplified picture can be obtained by the renormalized mean-field theory (RMFT), the so-called “plain vanilla” approach [148]. When this approach is applied to the  $t-J$  model, it is possible to describe many unusual properties of the high-temperature superconductors and capture the most important aspects of the cuprate phase diagram <sup>1</sup>.

However, at present, most of the calculations have been done by neglecting antiferromagnetic correlations, that are definitively important at low doping. Within RMFT and most of the variational calculations, the magnetic correlations are omitted, implying a spin liquid (disordered) state in the insulating regime. Although antiferromagnetism can be easily introduced in both approaches, it is often not satisfactorily described, since the presence of an antiferromagnetic order parameter in the fermionic determinant implies a wrong behavior of the spin properties at small momenta [78, 149], unless a spin Jastrow factor is used to describe the corresponding spin-wave fluctuations. Indeed, it is now well known that the accurate correlated description of an ordered state is obtained by applying a long-range spin Jastrow factor to a state with magnetic order [97, 99, 127]. The important point is that the Gaussian fluctuations induced by the Jastrow term must be orthogonal to the direction of the order parameter, in order to reproduce correctly

---

<sup>1</sup>For a recent review on the RMFT and variational Monte Carlo based on the RVB wave function, see for instance, B. Edegger, V.N. Muthukumar, and C. Gros, to be published in *Advances in Physics*.

the low-energy spin-wave excitations. Moreover, by generalizing the variational wave function to consider Pfaffians instead of simple determinants [7, 133], it is possible to consider both electron pairing and magnetic order, that are definitively important to determine the phase diagram of the  $t-J$  model.

The interplay between superconductivity and magnetism is the subject of an intense investigation in the recent years. In most of the thermodynamic measurements these two kinds of order do not coexist, though elastic neutron scattering experiments for underdoped  $\text{YBa}_2\text{Cu}_3\text{O}_x$  could suggest a possible coexistence, with a small staggered magnetization [150–152].

On the contrary, in the  $t-J$  model, there is an evidence in favor of a coexistence [96], the antiferromagnetic order surviving up to a relatively large hole doping, i.e.,  $\delta \sim 0.1$  for  $J/t = 0.2$  [7]. Therefore, the regime of magnetic order predicted by these calculations extend to much larger doping than the experimental results and also the robustness of the coexistence of superconductivity and antiferromagnetism seems to be inconsistent with the experimental outcome. Of course, disorder effects, which are expected to be important especially in the underdoped region, would affect the general phase diagram [28]. However, without invoking disorder, one is also interested to understand if alternative ingredients can modify the phase diagram of the simple  $t-J$  model. For instance, band structure calculations support the presence of a sizable second-neighbor hopping  $t'$  in cuprate materials, showing a possible connection between the value of the highest critical temperature and the ratio  $t'/t$ . [153] Moreover, an experimental analysis suggests an influence of the value of  $t'/t$  on the pseudogap energy scale [154]. From a theoretical point of view, the effect of  $t'$  is still not completely elucidated, though there are different calculations providing evidence that a finite  $t'$  could suppress superconductivity in the low-doping regime [143, 155–159]. On the other hand, recent Monte Carlo calculations suggest that the presence of  $t'$  (as well as a third-neighbor hopping  $t''$ ) could induce an enhancement of pairing in optimal and overdoped regions [158, 159].

In this chapter, we want to examine the problem of the interplay between magnetism and superconductivity in the  $t-J$  model and its extension including a next-nearest-neighbor hopping  $t'$  by using improved variational and Green's function Monte Carlo (GFMC) techniques. Indeed, especially the latter approach has been demonstrated to be very efficient in projecting out a very accurate approximation

of the exact ground state and, therefore, can give useful insight into this important issue related to high-temperature superconductivity.

## 4.2 Model and Method

In this section, we introduce the basic notations for the  $t-t'-J$  model and for the techniques used to obtain our numerical results. First of all, we give the definition of the model and next we briefly describe the GFMC method within the fixed-node approximation, that is used to work out the main results of this chapter.

We consider the  $t-t'-J$  model on a two-dimensional square lattice with  $L$  sites and periodic boundary conditions on both directions:

$$\begin{aligned} \mathcal{H} = & J \sum_{\langle i,j \rangle} \left( \mathbf{S}_i \cdot \mathbf{S}_j - \frac{1}{4} n_i n_j \right) \\ & - t \sum_{\langle i,j \rangle \sigma} c_{i,\sigma}^\dagger c_{j,\sigma} - t' \sum_{\langle\langle k,l \rangle\rangle \sigma} c_{k,\sigma}^\dagger c_{l,\sigma} + h.c. \end{aligned} \quad (4.1)$$

where  $\langle \dots \rangle$  indicates the nearest-neighbor sites,  $\langle\langle \dots \rangle\rangle$  the next-nearest-neighbor sites,  $c_{i,\sigma}^\dagger$  ( $c_{i,\sigma}$ ) creates (destroys) an electron with spin  $\sigma$  on the site  $i$ ,  $\mathbf{S}_i = (S_i^x, S_i^y, S_i^z)$  is the spin operator,  $S_i^\alpha = \sum_{\sigma,\sigma'} c_{i,\sigma}^\dagger \tau_{\sigma,\sigma'}^\alpha c_{i,\sigma'}$ , being  $\tau^\alpha$  the Pauli matrices, and  $n_i = \sum_{\sigma} c_{i,\sigma}^\dagger c_{i,\sigma}$  is the local density operator. In the following, we set  $t = 1$  and consider  $t' = 0$  and  $t'/t = -0.2$ . Moreover, we consider two kinds of square clusters: Standard clusters with  $L = l \times l$  sites and  $45^\circ$  tilted lattices with  $L = 2 \times l^2$  sites. Besides translational symmetries, both of them have all reflection and rotational symmetries.

The variational wave function that we used, is the one defined in the previous chapter by:

$$|\Psi_{VMC}^{Pfaf}\rangle = \mathcal{J}_s \mathcal{J}_d \mathcal{P}_N \mathcal{P}_G |\Phi_{MF}\rangle, \quad (4.2)$$

where  $\mathcal{P}_G$  is the Gutzwiller projector that forbids double occupied sites,  $\mathcal{P}_N$  is the projector onto the subspace with fixed number of  $N$  particles,  $\mathcal{J}_s$  is a spin Jastrow factor(3.19), and finally  $\mathcal{J}_d$  is a density Jastrow factor(3.20).

As explained in the second chapter, the above wave function can be efficiently sampled by standard variational Monte Carlo, by employing a random walk of

a configuration  $|x\rangle$ , defined by the electron positions and their spin components along the  $z$  quantization axis. Indeed, in this case, both Jastrow terms are very simple to compute, since they only represent classical weights acting on the configuration.

As reported in the previous chapter, the main difference from previous approaches is the presence of the spin Jastrow factor and the choice of the mean-field state  $|\Phi_{MF}\rangle$ , defined as the ground state of the mean-field Hamiltonian(3.21), where we include both BCS pairing  $\Delta_{i,j}$  [with  $d$ -wave symmetry, i.e., for nearest-neighbor sites  $\Delta_k = \Delta(\cos k_x - \cos k_y)$ ] and staggered magnetic field in the  $x$ - $y$  plane(3.22) where  $\Delta_{AF}$  is a variational parameter that, together with the chemical potential  $\mu$  and the next-nearest-neighbor hopping of Eq. (3.21), can be determined by minimizing the variational energy of  $\mathcal{H}$ . As seen in the previous chapter, whenever both  $\Delta$  and  $\Delta_{AF}$  are finite, the mean-field state  $|\Phi_{MF}\rangle$  can be described in terms of Pfaffians, instead if  $\Delta = 0$  or  $\Delta_{AF} = 0$  it can be described by using determinants. Moreover, only in the case where the magnetic order parameter is in the  $x$ - $y$  plane, the presence of the spin Jastrow factor (3.19) can introduce relevant fluctuations over the mean-field order parameter  $\Delta_{AF}$ , leading to an accurate description of the spin properties. The variational parameters contained in the mean-field Hamiltonian (3.21) and in the Jastrow factors (3.19) and (3.20) are calculated by using the optimization technique described in Refs. [160, 161], that make it possible to handle with a rather large number of variational parameters.

The optimized variational wave function  $|\Psi_{VMC}^{Pfaf}\rangle$  can be also used as *guiding* function within the GFMC method to filter out an approximation of the ground state  $|\Psi_0^{FN}\rangle$ . Indeed, due to the presence of the fermionic sign problem, in order to have a stable numerical calculation, the GFMC must be implemented within the fixed-node (FN) approach, that imposes to  $|\Psi_0^{FN}\rangle$  to have the same nodal structure of the variational ansatz [105]. We have seen in the second chapter the basic definitions of the standard FN method. Here, we just recall some basic definitions that can be useful in the following.

Since  $|\Psi_0^{FN}\rangle$  is an exact eigenstate of the effective Hamiltonian  $\mathcal{H}_{eff}$  (2.67), the corresponding ground-state energy can be evaluated efficiently by computing

$$E_{MA} = \frac{\langle \Psi_{VMC} | \mathcal{H}_{eff} | \Psi_0^{FN} \rangle}{\langle \Psi_{VMC} | \Psi_0^{FN} \rangle}, \quad (4.3)$$

namely the statistical average of the local energy  $e_L(x) = \langle \Psi_{VMC} | \mathcal{H} | x \rangle / \langle \Psi_{VMC} | x \rangle$

over the distribution  $\Pi_x \propto \langle x | \Psi_{VMC} \rangle \langle x | \Psi_0^{FN} \rangle$ . The mixed average (MA) quantity  $E_{MA} \leq E_{VMC}$  because, by the variational principle

$$E_{MA} \leq \frac{\langle \Psi_{VMC} | \mathcal{H}_{eff} | \Psi_{VMC} \rangle}{\langle \Psi_{VMC} | \Psi_{VMC} \rangle} = E_{VMC}. \quad (4.4)$$

Moreover,  $E_{MA}$  represents an upper bound of the expectation value  $E_{FN}$  of  $\mathcal{H}$  over  $|\Psi_0^{FN}\rangle$  [105]. In the following, we will denote by FN the (variational) results obtained by using the GFMC method with fixed-node approximation, whereas the standard variational Monte Carlo results obtained by considering the wave function of Eq. (3.18) will be denoted by VMC.

Summarizing, the FN approach is a more general and powerful variational method than the straightforward variational Monte Carlo. Within the FN method, the wave function  $|\Psi_0^{FN}\rangle$ , the ground state of  $\mathcal{H}^{eff}$  is known only statistically, and, just as in the variational approach,  $E_{FN}$  depends explicitly on the variational parameters defining the guiding function  $|\Psi_{VMC}\rangle$ . The main advantage of the FN approach is that it provides the exact ground-state wave function for the undoped insulator (where the signs of the exact ground state are known), and therefore it is expected to be particularly accurate in the important low-doping region. Moreover, the FN method is known to be very efficient in various cases: For instance, it has allowed to obtain a basically exact description of the three-dimensional system of electrons interacting through the realistic Coulomb potential (in presence of a uniform positive background) [162]. Therefore, it represents a very powerful tool to describe the electron correlation in electronic systems.

## 4.3 Results

### 4.3.1 Phase separation

Before showing the results on magnetic and superconducting properties, we briefly discuss the stability against phase separation. In order to detect a possible phase separation, it is very useful to follow the criterion given in the previous chapter and in Ref. [44] and consider the energy per hole:

$$e_h(\delta) = \frac{e(\delta) - e(0)}{\delta}, \quad (4.5)$$

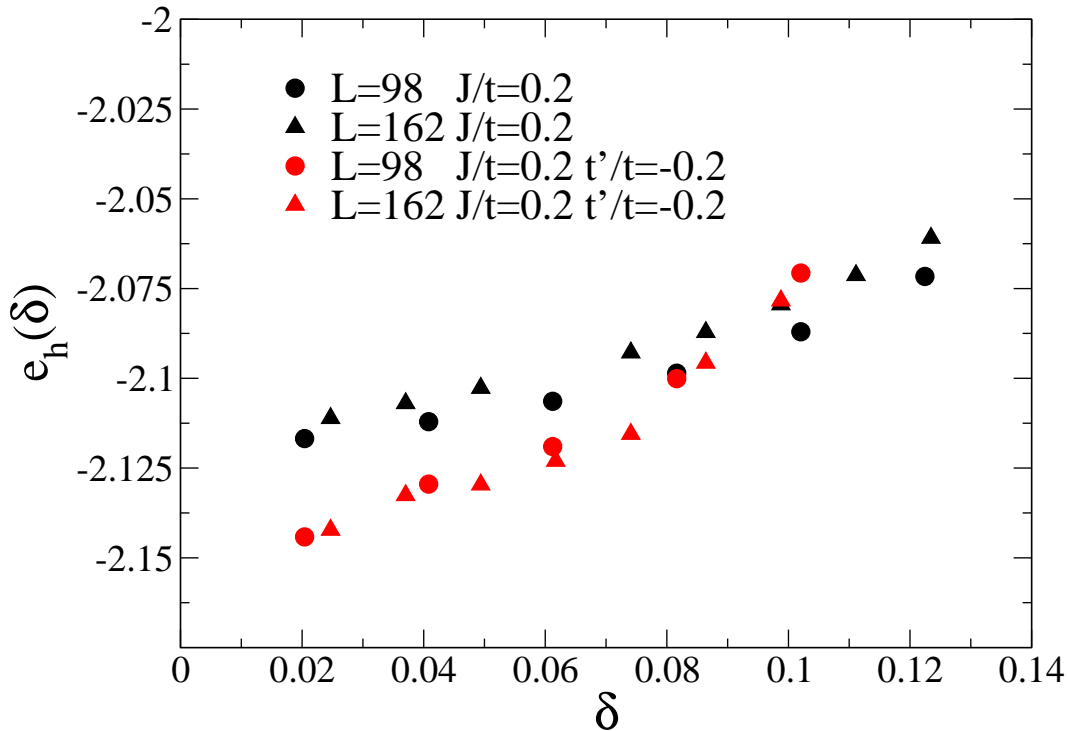


Figure 4.1: Energy per hole  $e_h(\delta)$ , calculated by using the FN method, as a function of the doping  $\delta$  for  $L = 98$  and  $162$  and two values of the next-nearest-neighbor hopping  $t'/t = 0$  and  $-0.2$ .

where  $e(\delta)$  is the energy per site at hole doping  $\delta$  and  $e(0)$  is its value at half filling. In practice,  $e_h(\delta)$  represents the chord joining the energy per site at half filling and the one at doping  $\delta$ . For a stable system,  $e_h(\delta)$  must be a monotonically increasing function of  $\delta$ , implying that energy is a convex function of the doping. By contrast, the phase separation instability is marked by a minimum at a given  $\delta_c$  on finite clusters, and a flat behavior up to  $\delta_c$  in the thermodynamic limit where the Maxwell construction is implied. In the previous chapter, we demonstrated existence of an homogeneous state for  $t' = 0$  and  $J/t \lesssim 0.7$ . As shown in Table 4.1, the FN approximation, that is exact at zero doping [7], provides a substantial lowering of the VMC energy, especially away from half filling and for a finite  $t'$ . This is a first indication that the simple variational approach could not be adequate to

Table 4.1: Variational (VMC) and fixed-node (FN) energies per site for  $J/t = 0.2$  and  $t' = 0$  (third and fourth columns), and  $t'/t = -0.2$  (fifth and sixth columns) for two clusters with  $L = 98$  and  $162$  and different hole concentrations  $N_h = L - N$

$L$	$N_h$	$E_{VMC}/L$	$E_{FN}/L$	$E_{VMC}/L$	$E_{FN}/L$
98	0	-0.233879(1)	-0.23432(1)	-0.233879(1)	-0.23432(1)
98	2	-0.274144(5)	-0.27752(1)	-0.27290(1)	-0.27808(1)
98	4	-0.31429(1)	-0.32053(1)	-0.31189(1)	-0.32123(1)
98	6	-0.35482(1)	-0.36328(1)	-0.35132(1)	-0.36405(1)
98	8	-0.39550(1)	-0.40563(2)	-0.39028(1)	-0.40575(1)
98	10	-0.43581(1)	-0.44728(2)	-0.42814(1)	-0.44561(1)
162	0	-0.233707(1)	-0.23409(1)	-0.233707(1)	-0.23409(1)
162	2	-0.258002(5)	-0.26020(1)	-0.257260(5)	-0.26012(1)
162	4	-0.282117(5)	-0.28621(1)	-0.28067(1)	-0.28698(1)
162	6	-0.306324(5)	-0.31212(1)	-0.30429(1)	-0.31307(1)
162	8	-0.33060(1)	-0.33793(1)	-0.32807(1)	-0.33925(2)
162	10	-0.35498(1)	-0.36360(2)	-0.35207(1)	-0.36514(2)
162	12	-0.37954(1)	-0.38912(2)	-0.37567(1)	-0.39079(2)
162	14	-0.40406(1)	-0.41446(2)	-0.39939(1)	-0.41520(2)
162	16	-0.42838(1)	-0.43946(2)	-0.42232(1)	-0.43936(2)

provide a reliable quantitative description of the ground-state properties.

The FN results clearly indicate that the inclusion of a negative next-nearest-neighbor hopping contributes to further stabilize the homogeneous phase at finite doping, see Fig. 4.1. This result is compatible with the outcome of recent calculations based on cluster dynamical mean-field theory on the Hubbard model, where a negative ratio  $t'/t$  enhances the stability of the homogeneous phase, whereas positive values of  $t'$  favor phase separation [163]. Here, we do not want to address in much detail this issue and we will focus our attention on the more interesting magnetic and superconducting properties.

### 4.3.2 Antiferromagnetic properties

Here we present the results for the magnetic properties of the  $t-t'-J$  model and compare the FN approach with the VMC one, based upon the wave function (3.18). As already discussed in the previous chapter, the optimized wave function (3.18) breaks the SU(2) spin symmetry, because of the magnetic order parameter  $\Delta_{AF}$  of Eq. (3.22) and the spin Jastrow factor (3.19). It turns out that at half-filling and in the low-doping regime, the variational state (3.18) has an antiferromagnetic order in the  $x-y$  plane, whereas the spin-spin correlations in the  $z$  axis decay very rapidly. Therefore, in order to assess the magnetic order at the variational level, we have to consider the isotropic spin-spin correlations:

$$\langle \mathbf{S}_0 \cdot \mathbf{S}_r \rangle = \frac{\langle \Psi_{VMC} | \mathbf{S}_0 \cdot \mathbf{S}_r | \Psi_{VMC} \rangle}{\langle \Psi_{VMC} | \Psi_{VMC} \rangle}. \quad (4.6)$$

The FN approach alleviates the anisotropy between the  $x-y$  plane and the  $z$  axis; in this case, we find that a rather accurate (and much less computational expensive) way to estimate of the magnetic moment can be obtained from the  $z$  component of the spin-spin correlations:

$$\langle S_0^z S_r^z \rangle = \frac{\langle \Psi_0^{FN} | S_0^z S_r^z | \Psi_0^{FN} \rangle}{\langle \Psi_0^{FN} | \Psi_0^{FN} \rangle}, \quad (4.7)$$

that, since the operator  $S_0^z S_r^z$  is diagonal in the basis used in the Monte Carlo sampling, can be easily computed within the forward-walking technique [104].

From the spin-spin correlations at the maximum distance, it is possible to extract the value of the magnetization. In particular, for the variational wave function, that is not a singlet when the antiferromagnetic order sets in,  $M = \lim_{r \rightarrow \infty} \sqrt{\langle \mathbf{S}_0 \cdot \mathbf{S}_r \rangle}$ , whereas for the FN one, the magnetization can be estimated by  $M = \lim_{r \rightarrow \infty} \sqrt{3 \langle S_0^z S_r^z \rangle}$ . The spin isotropy of the FN wave function can be checked by explicitly computing the mixed-average of the total spin square

$$\langle S^2 \rangle_{MA} = \frac{\langle \Psi_{VMC} | S^2 | \Psi_0^{FN} \rangle}{\langle \Psi_{VMC} | \Psi_0^{FN} \rangle}, \quad (4.8)$$

that vanishes if  $|\Psi_0^{FN}\rangle$  is a perfect singlet, even if  $|\Psi_{VMC}\rangle$  has not a definite value of the spin.

In Fig. 4.2 we report the results of the magnetization in the  $t-J$  model with  $J/t = 0.2$  and  $0.4$ . At finite doping, it is not possible to perform a precise size

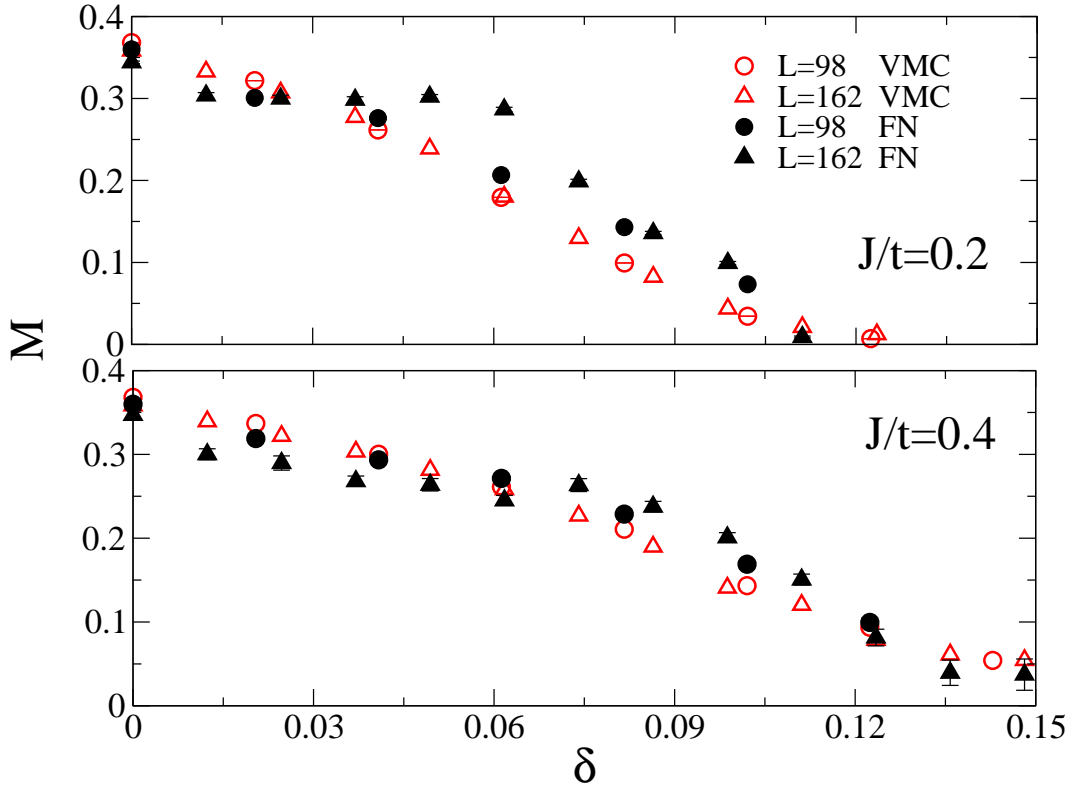


Figure 4.2: Magnetization obtained from the spin-spin correlations at the maximum distance calculated for the  $t-J$  model with  $J/t = 0.2$  (upper panel) and  $J/t = 0.4$  (lower panel). For the VMC calculations the error-bars are smaller than the symbol sizes. The VMC magnetization has been obtained from the isotropic correlations, whereas the FN one from the correlations along the  $z$  axis (see text).

scaling extrapolation since it is very rare to obtain the same doping concentration for different cluster sizes. Moreover, though the FN approach is able to recover an exact singlet state at half filling,  $\langle S^2 \rangle_{MA}$  increases by doping, reaching its maximum around  $\delta \sim 0.06$ , e.g.,  $\langle S^2 \rangle_{MA} \sim 1$  for 8 holes on 162 sites. This could explain that, especially for  $J/t = 0.2$ , the FN results are a bit larger than the VMC ones for  $\delta \sim 0.06$ . Definitely, close to the transition point, where the mean-field order parameter  $\Delta_{AF}$  goes to zero (together with the parameters defining the spin Jastrow factor), both the VMC and FN wave functions are almost spin singlets. Therefore, we are rather confident in the estimation of the critical doping

$\delta_c$ , where long-range antiferromagnetic order disappears. In particular, we find  $\delta_c = 0.10 \pm 0.01$  and  $\delta_c = 0.13 \pm 0.02$  for  $J/t = 0.2$  and  $J/t = 0.4$ , respectively.

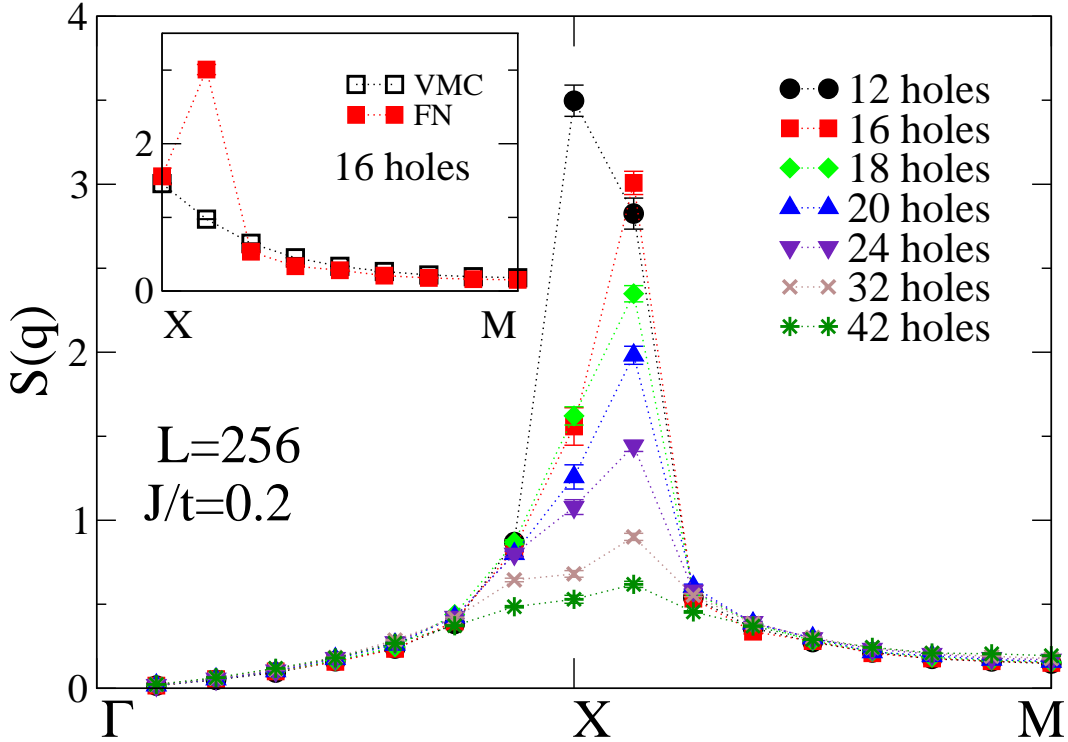


Figure 4.3: Static spin structure factor  $S(q)$  for  $L = 16 \times 16$  cluster and different hole concentrations for the  $t$ - $J$  model with  $J/t = 0.2$ .  $\Gamma = (0, 0)$ ,  $X = (\pi, \pi)$ , and  $M = (\pi, 0)$ . Inset:  $S(q)$  for the variational state (empty symbols) and for the FN approximation (full symbols).

At low doping, we have evidence that long-range order is always commensurate, with a (diverging) peak at  $X = (\pi, \pi)$  in the static spin structure factor, defined as

$$S(q) = \frac{1}{L} \sum_{l,m} e^{iq(R_l - R_m)} S_l^z S_m^z. \quad (4.9)$$

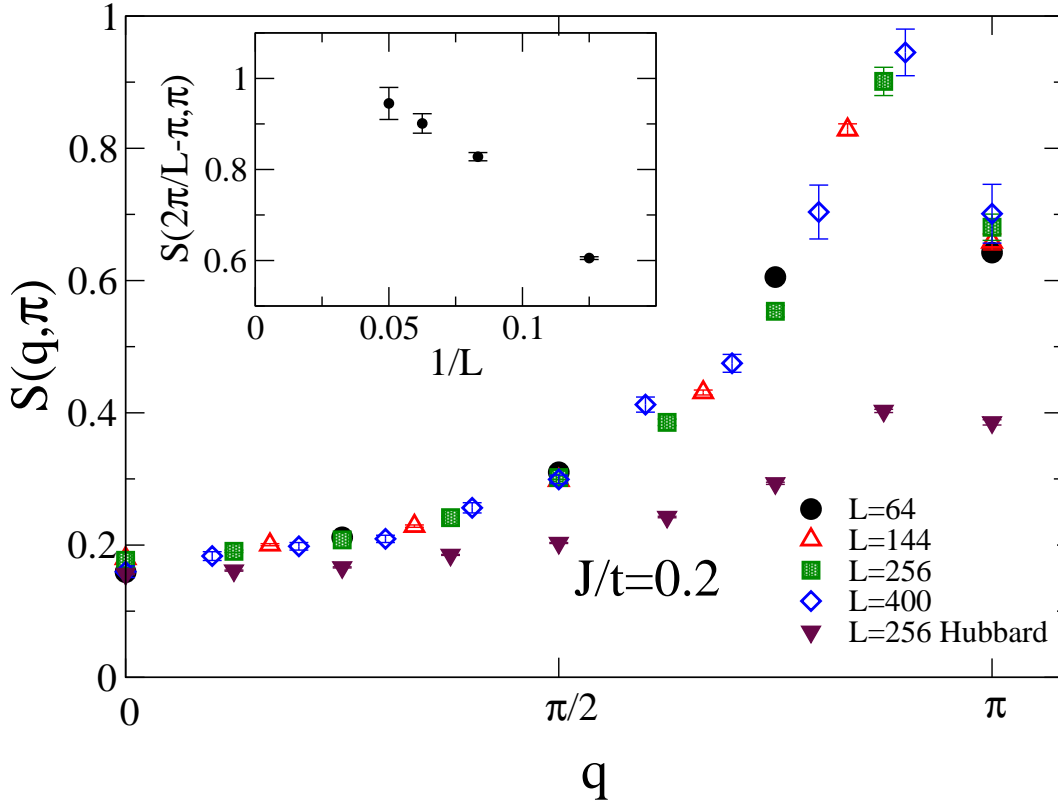


Figure 4.4: Spin structure factor  $S(q)$  for the  $t$ - $J$  with  $J/t = 0.2$  and doping  $\delta = 1/8$  and different clusters ( $L = 8 \times 8$ ,  $12 \times 12$ ,  $16 \times 16$ , and  $20 \times 20$ ). The case of the Hubbard model at  $U/t = 4$  and  $L = 16 \times 16$  is also reported for comparison. Inset: Size scaling of the peak as a function of  $1/L$ .

This outcome is clear for all kinds of cluster considered, namely both for standard  $l \times l$  and  $45^\circ$  tilted lattices. By contrast, close to the critical doping, we have the indication that some incommensurate peaks develop. Remarkably, we do not find any strong doping dependence of the peak positions. We show the results of  $S(q)$  for the  $16 \times 16$  cluster and  $J/t = 0.2$  in Fig. 4.3, where the evolution of the peak as a function of the doping  $\delta$  is reported. By increasing the hole doping, the commensurate peak at  $X$  reduces its intensity and eventually shifts to a different k-point, i.e.,  $(\pi, \pi - 2\pi/L)$ . This is a genuine effect of the FN projection, since

the variational wave function always shows commensurate correlations, see inset of Fig. 4.3. Moreover, this feature can be obtained only when the BCS parameter is considered, a FN calculation with a fully projected free-electron determinant cannot reproduce an incommensurate peak in  $S(q)$  (see Fig. 4.5). Interestingly, for all the cluster sizes we considered, i.e., up to  $L = 20 \times 20$ , the peak always appears at  $(\pi, \pi - 2\pi/L)$ , namely the closest k-point to  $X$  along the border of the Brillouin zone. This indicates that, in the thermodynamic limit, the peak should be located very close to  $X$  and it is not compatible with  $(\pi, \pi - 2\pi\delta)$ , found in cuprate materials [48]. As one can see from Fig. 4.6 and Fig. 4.7, the above mentioned peak, besides to be quite independent from doping, is also qualitatively independent from the presence of the  $t'$  term, which frustrates the antiferromagnetic order of the system.

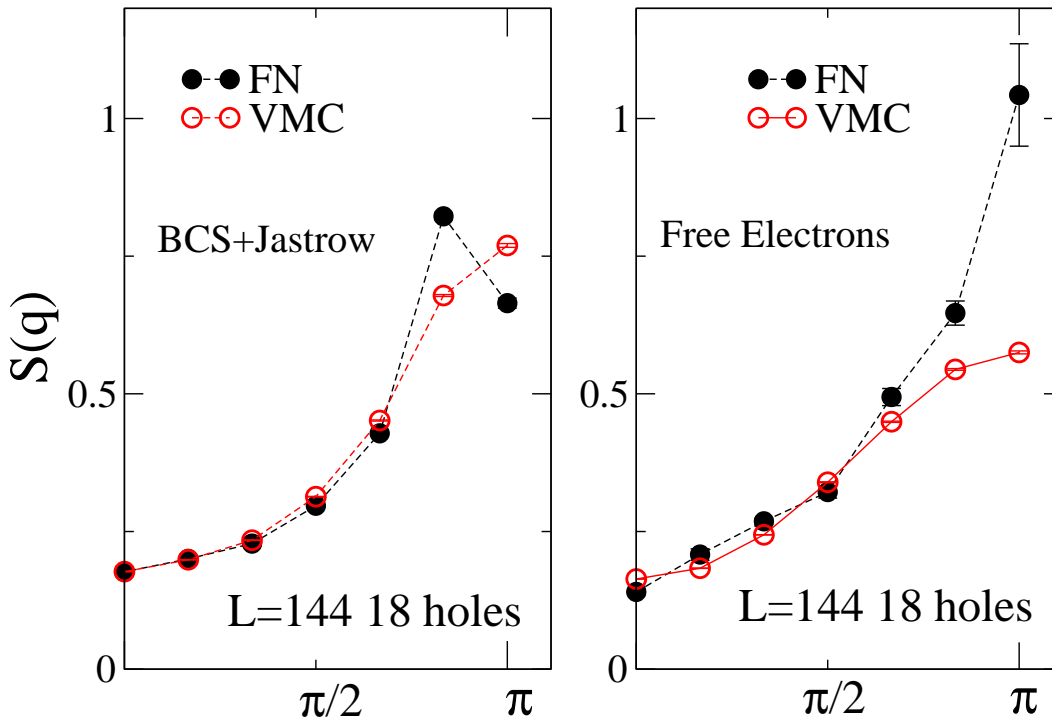


Figure 4.5: Static spin structure factor  $S(q)$ , calculated with a BCS wave function (Left panel) and with a free-electron wave function (Right panel).

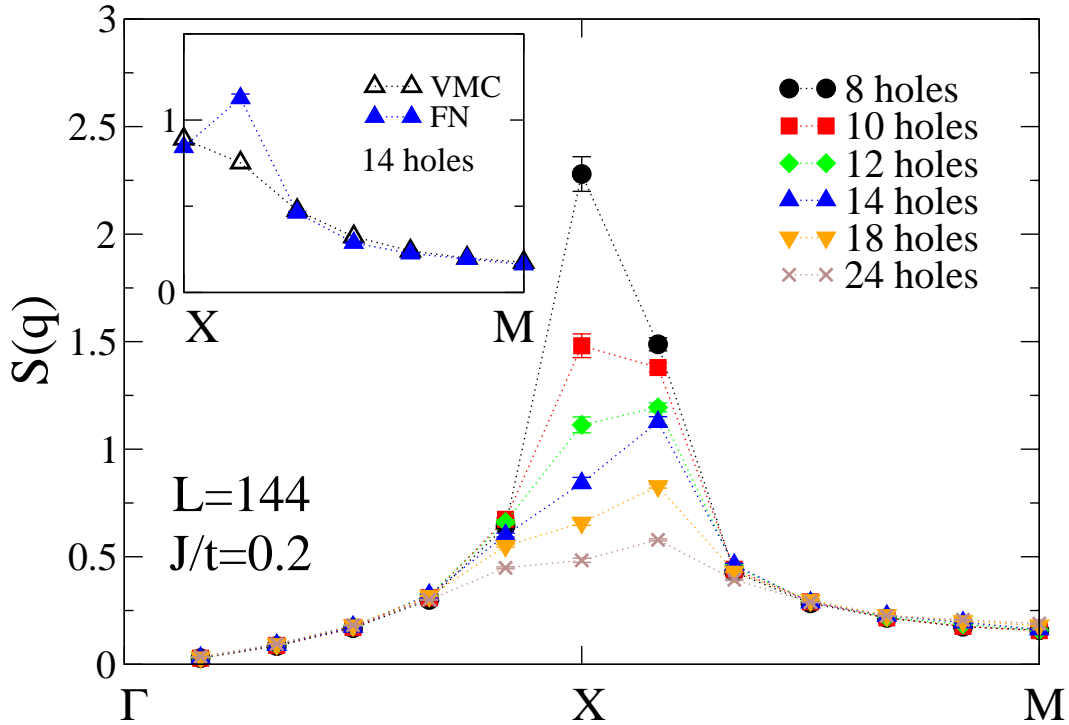


Figure 4.6: Static spin structure factor  $S(q)$  for the  $t-J$  model on the  $L = 12 \times 12$  cluster with  $J/t = 0.2$ .

Although size scaling extrapolations are not possible for a generic hole doping, we do not have evidence that the incommensurate peak diverges in the thermodynamic limit, implying no incommensurate long-range order at finite doping concentrations. Nevertheless, once the commensurate magnetic order is melted, the ground state is characterized by short-range incommensurate spin correlations. In Fig. 4.4, we show the results for  $J/t = 0.2$  and  $\delta = 1/8$ , where different clusters with the same doping are available. Interestingly, the position of the incommensurate peak is the same as the one found in the Hubbard model at  $U/t = 4$  (where our FN results correctly reproduce the previous data reported in Ref. [164] on the  $10 \times 10$  lattice), though its intensity is much more reduced compared to the case of the  $t-J$  model. This fact suggests that the peak is not related to the strong coupling limit.

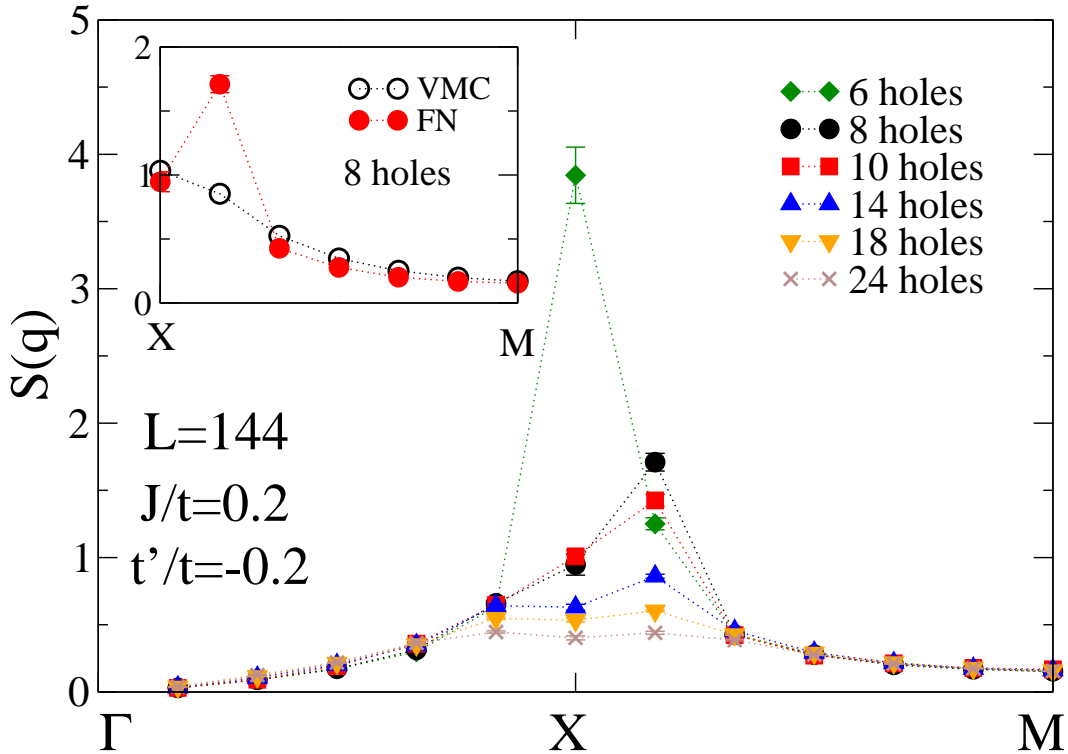


Figure 4.7: The same as Fig.4.6 for the  $t-t'-J$  model with  $J/t = 0.2$  and  $t'/t = -0.2$ .

Coming back to the commensurate magnetic order close to half-filling, we stress that the pure  $t-J$  model shows robust antiferromagnetic correlations, with a critical doping much larger than the one observed in the hole-doped cuprates materials, where the long-range order disappears at  $\delta_c \sim 0.05$  [48]. This smaller value of the critical doping cannot be explained by reducing the antiferromagnetic superexchange  $J$ , given the fact that, by changing  $J/t$  from 0.4 to 0.2, the variation of  $\delta_c$  is smaller than 30%. Besides disorder effects that can be important in the underdoped regime [28], one important ingredient to be considered in a microscopic model is the next-nearest-neighbor hopping, that was shown to have remarkable effects on both magnetic and superconducting properties [155, 156, 158, 159]. In particular, in spite exact diagonalization calculations suggest a suppression of

antiferromagnetic correlations for negative  $t'/t$  [155], more recent Monte Carlo simulations (also including a further third-neighbor hopping  $t''$ ) do not confirm these results, pointing instead toward a suppression of superconducting correlations [159].

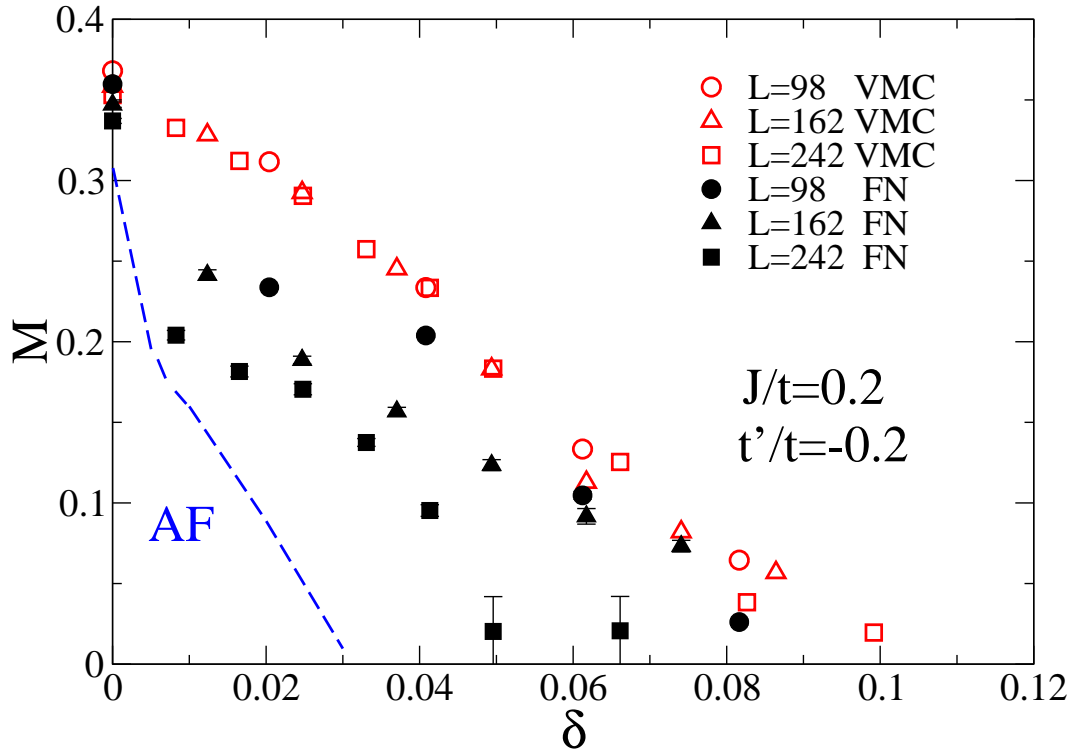


Figure 4.8: The same as in Fig. 4.2 for the  $t-t'-J$  model with  $J/t = 0.2$  and  $t'/t = -0.2$ . For the VMC calculations the error-bars are smaller than the symbol sizes. The dashed line indicates a tentative estimation for the thermodynamic limit.

In Fig. 4.8, we report the magnetization for  $J/t = 0.2$  and  $t'/t = -0.2$ . The first outcome is that the VMC results, though pretty renormalized with respect to the case  $t' = 0$ , present a critical doping  $\delta_c$  very similar to the one found for the pure  $t-J$  model. By contrast, the FN approach strongly suppresses the spin-spin correlations, even very close to half filling. In this case, the FN results

have rather large size effects, that prevent us to extract a reliable estimate for the thermodynamic limit. However, it is clear that the antiferromagnetic region is tiny and we can estimate that  $\delta_c \lesssim 0.03$ . It should be emphasized that for  $t'/t = -0.2$  the variational wave function is not as accurate as for the pure  $t-J$  model with  $t' = 0$ , but nevertheless the projection technique, even if approximate, is able to reduce the bias (e.g., the presence of a large magnetic order up to  $\delta \sim 0.1$ ), showing the importance of alternative numerical methods to assess the actual accuracy of the simple variational approach. Indeed, we are confident that our FN results represent a good approximation of the true ground-state properties. On the contrary, the VMC calculations clearly show that the wave function (3.18) overestimates the correct value of the magnetic moment.

### 4.3.3 Superconducting properties

In the following, we want to address the problem of the superconducting properties of the Hamiltonian (4.1). In particular, we would like to obtain an accurate determination of the pair-pair correlations as a function of the hole doping and clarify the role of the next-nearest-neighbor hopping  $t'$ . The effect of such term has been recently considered by using different numerical techniques. Density-matrix renormalization group for  $n$ -leg ladders (with  $n = 4$  and  $6$ ) showed that the effect of a negative  $t'$  is to stabilize a metallic phase, without superconducting correlations [156]. Moreover, improved variational Monte Carlo techniques suggested that  $t'$  could suppress pairing at low doping, whereas some increasing of superconducting correlations can be found in the optimal doping regime [158, 159]. A further variational study [157], suggested the possibility that a sufficiently large ratio  $t'/t$  can disfavor superconductivity and stabilize charge instabilities (stripes) near  $1/8$  doping.

The pair-pair correlations are defined as

$$\Delta^{\mu,\nu}(r) = S_{r,\mu} S_{0,\nu}^\dagger, \quad (4.10)$$

where  $S_{r,\nu}^\dagger$  creates a singlet pair of electrons in the neighboring sites  $r$  and  $r + \mu$ , namely

$$S_{r,\mu}^\dagger = c_{r,\uparrow}^\dagger c_{r+\mu,\downarrow}^\dagger - c_{r,\downarrow}^\dagger c_{r+\mu,\uparrow}^\dagger. \quad (4.11)$$

Most importantly, for the first time, we implemented the forward-walking technique in order to compute true expectation values of the pairing correlations over the FN state:

$$\langle \Delta^{\mu,\nu}(r) \rangle = \frac{\langle \Psi_0^{FN} | \Delta^{\mu,\nu}(r) | \Psi_0^{FN} \rangle}{\langle \Psi_0^{FN} | \Psi_0^{FN} \rangle}. \quad (4.12)$$

Indeed, given the fact that  $\Delta^{\mu,\nu}(r)$  is a non-diagonal operator (in the  $|x\rangle$  basis, defined above), within the FN approach all the previous calculations [96] were based upon the so-called mixed average, where, similarly to Eq. (4.3), the state on the left is replaced by the variational one. Now, by using Eq. (4.12), it is possible to verify the fairness of the variational results against a much more accurate estimation of the exact correlation functions given by the FN approach.

The superconducting off-diagonal long-range order implies a non-zero value of  $\langle \Delta^{\mu,\nu}(r) \rangle$  at large distance  $r$ . In the following, we consider the pair-pair correlation at the maximum distance and  $\mu = \nu$  (parallel singlets) both for the variational case and for the FN approximation and denote  $P_d^2 = 4 \lim_{r \rightarrow \infty} \langle \Delta^{y,y}(r) \rangle$ . It is worth noting that, as far as the superconducting correlations are concerned, there is no appreciable difference between the results obtained with and without the antiferromagnetic order parameter and the long-range spin Jastrow factor. The results for the pure  $t-J$  model are reported in Fig 4.9, where we report two different values of the antiferromagnetic coupling, i.e.,  $J/t = 0.2$  and  $J/t = 0.4$ . In this case, variational and FN calculations are in fairly good agreement, giving a similar superconducting phase diagram. In contrast to RMFT, that predicts a quadratic behavior of the pair-pair correlations, the variational results show that these correlations have instead a linear behavior with  $\delta$  in the underdoped regime, even in the simplest case without Jastrow term [165]. Interestingly, the optimal doping, i.e., the doping at which the maximum in the pair-pair correlations takes place, occurs in both cases at  $\delta \sim 0.2$ , whereas the actual value of the correlations is proportional to  $J/t$ . At high doping, where antiferromagnetic fluctuations play a minor role, the behavior of the pairing is unchanged when  $J$  is varied. Although in this region there are some size effects, we can safely estimate that superconductivity disappears around  $\delta \sim 0.35$  and  $\delta \sim 0.4$  for  $J/t = 0.2$  and  $J/t = 0.4$ , respectively.

It is worth noting that the density Jastrow term (3.20) is very important to obtain an accurate estimation of the pairing correlations. Indeed, whereas the

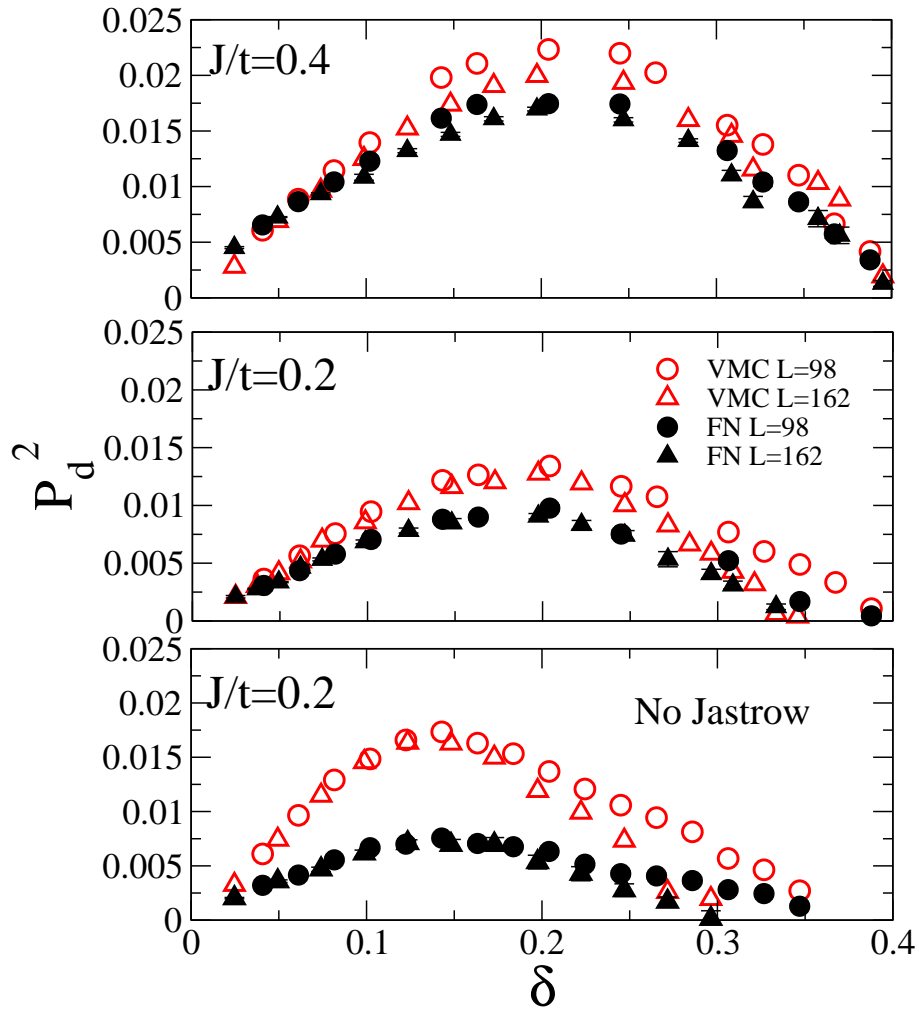


Figure 4.9: Pair-pair correlations at the maximum distance as a function on the doping for  $J/t = 0.4$  (upper panel) and  $J/t = 0.2$  (middle panel). The results for the variational wave function (3.18) (empty symbols) and for the FN approximation (filled symbols) are reported. The results for the wave function without the Jastrow factors (both for spin and density) and magnetic order parameter are also reported (lower panel).

qualitative behavior as a function of doping is correctly captured by the simplest variational wave function with BCS pairing and on-site Gutzwiller projector, the

variational results based on such a state overestimate the pairing correlations at optimal doping by a factor two. Remarkably, the FN approach is able to correct this bias and give approximately the same results as the one obtained starting from the wave function with the long-range Jastrow factor, see Fig. 4.9. This fact demonstrates once more the reliability of the FN method, that can reduce significantly the dependence of the results upon the choice of the variational ansatz.

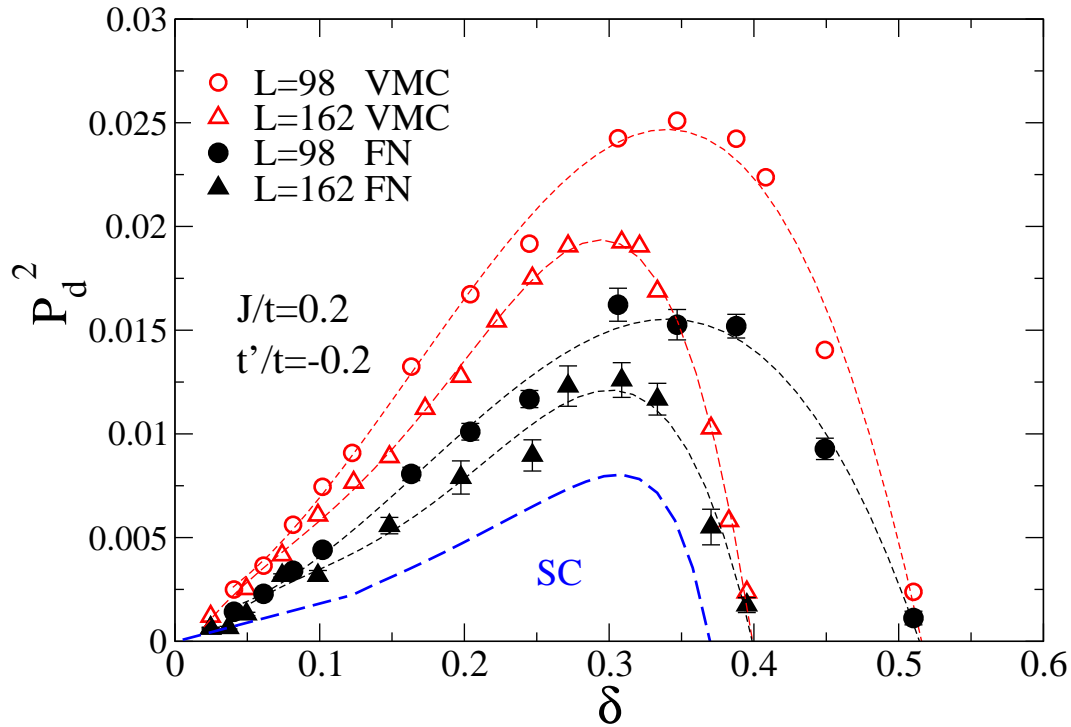


Figure 4.10: The same as in Fig. 4.9 for the  $t-t'-J$  model with  $J/t = 0.2$  and  $t'/t = -0.2$ . The dashed line indicates a tentative estimation for the thermodynamic limit.

The inclusion of the next-nearest-neighbor hopping induces sizable modifications in the pairing correlations, though the qualitative dome-like behavior remains unchanged, see Fig. 4.10. At low doping there is a sizable suppression of the superconducting pairing, particularly evident after the FN projection, see Fig. 4.11. Indeed, while for the pure  $t-J$  model we clearly obtain a linear behav-

ior of the pair-pair correlations with  $\delta$ , indicating a superconducting phase as soon as the Mott insulator is doped, in the case of a finite  $t'$ , the FN results could be compatible with a finite critical doping, below which the system is not superconducting. This outcome is in agreement with earlier Monte Carlo calculations done by Anisimov, Sorella et al., [166] where it was suggested that the extended  $t$ - $J$  model with hoppings and super-exchange interactions derived from structural data of the  $\text{La}_2\text{CuO}_4$  compound could explain the main experimental features of high-temperature superconducting materials, with a finite critical doping for the onset of electron pairing.

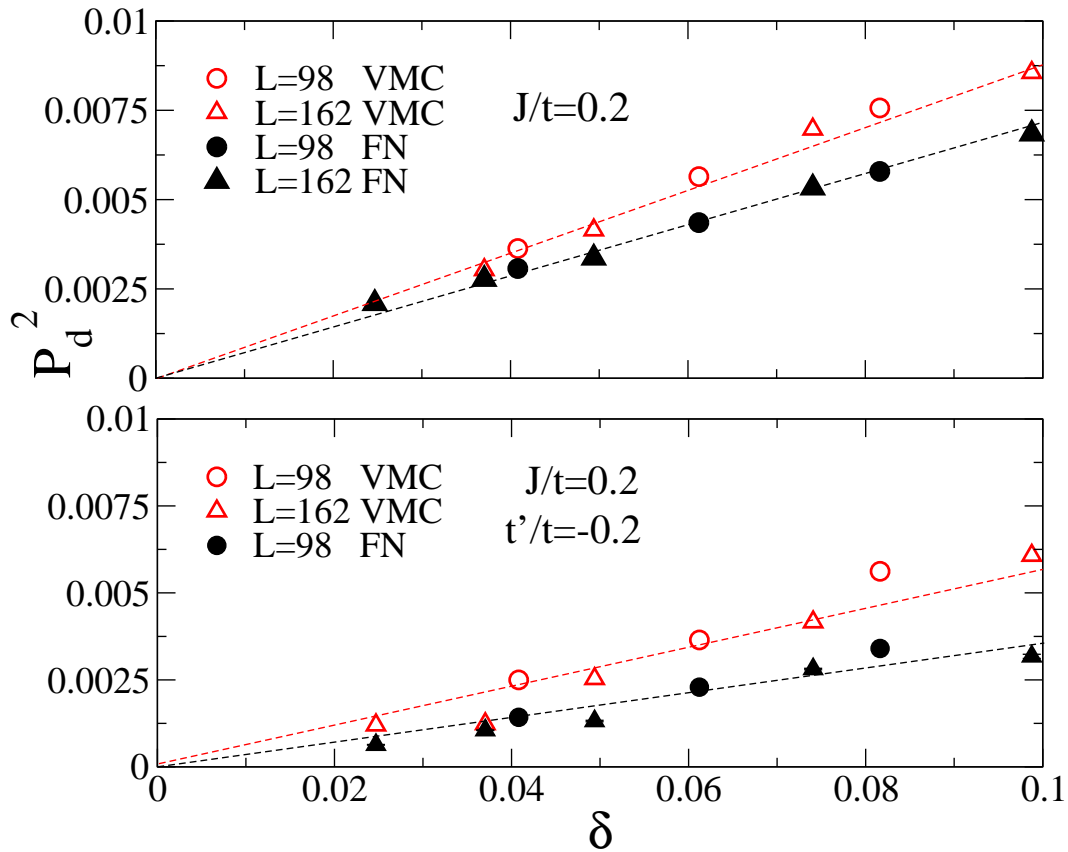


Figure 4.11: Detail of the pair-pair correlations reported in Figs. 4.9 and 4.10 at low doping.

Remarkably, from  $\delta \sim 0.1$  to  $\delta \sim 0.4$  there are huge size effects. Though, for  $\delta \sim 0.3$ , small clusters, e.g.,  $L = 98$ , indicate stronger pairing correlations

than the pure  $t-J$  model without  $t'$ , larger clusters point out a large reduction of  $P_d^2$ . Nonetheless, we have a rather clear evidence that for  $\delta \sim 0.3$  there is a finite superconducting order parameter in the thermodynamic limit, see Fig. 4.12. This strong reduction of the superconducting correlations is a very interesting effect, demonstrating that the superconducting wave function (even if supplemented by magnetic order) deteriorates its accuracy by increasing the value of  $t'$ , that could eventually stabilize competing phases with modulation in the charge distribution and/or a magnetic flux through the plaquettes [167]. However, for  $t'/t = -0.2$ , our variational wave function (3.18) remains a better energy when compared to the one used in Ref. [167].

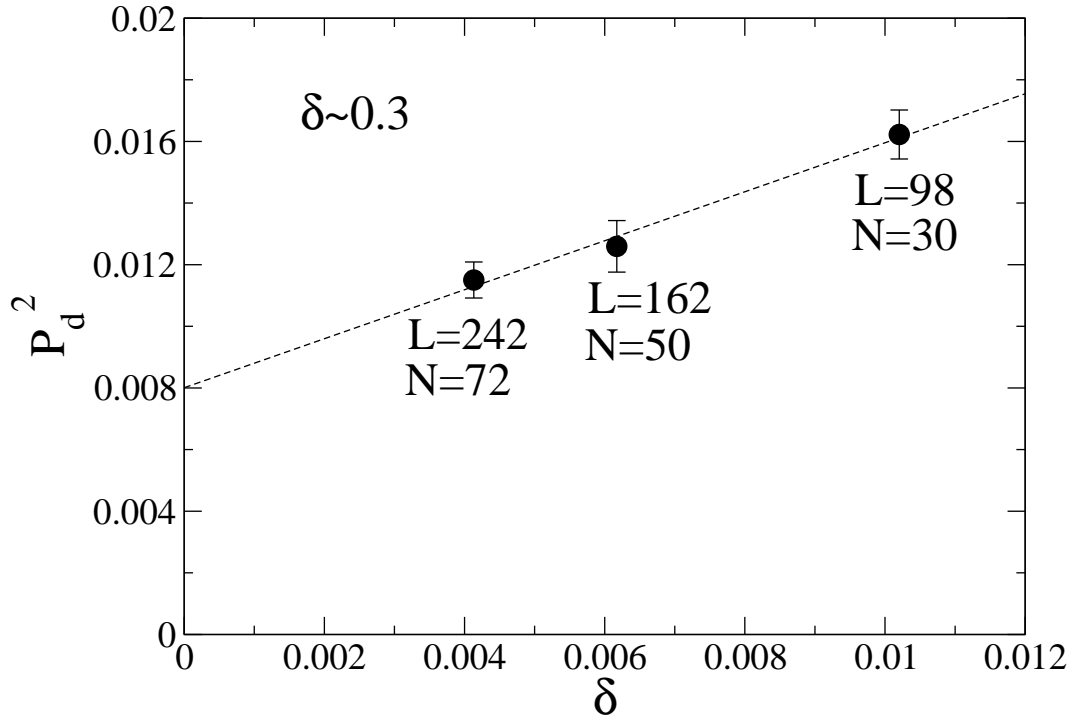


Figure 4.12: Size scaling of the Pair-pair correlations at the maximum distance for  $t-t'-J$  model with  $J/t = 0.2$  and  $t'/t = -0.2$  at  $\delta \sim 0.3$ .

## 4.4 Conclusion

In this chapter, we considered the magnetic and superconducting properties of the  $t-t'-J$  model within the variational and the FN approaches. We showed that for  $t' = 0$  the ground-state properties can be accurately reproduced by a state containing both electron pairing and suitable magnetic correlations, namely a magnetic order parameter in the mean-field Hamiltonian that defines the fermionic determinant and a spin Jastrow factor for describing the spin fluctuations. In this case, we obtain a rather large magnetic phase, with a critical doping that slightly depend upon the super-exchange coupling  $J$ , i.e.,  $\delta_c = 0.10 \pm 0.01$  and  $\delta_c = 0.13 \pm 0.02$  for  $J/t = 0.2$  and  $J/t = 0.4$ , respectively. The superconducting correlations show a dome-like behavior and vanish when the Mott insulator at half filling is approached. Interestingly, compared to the RMFT that predicts a quadratic behavior of the pair-pair correlations as a function of the doping  $\delta$ , here we found that a linear behavior is more plausible.

Then, we also reported important modifications due to the presence of a finite ratio  $t'/t$ . The first effect of this further hopping term is to strongly suppress antiferromagnetic correlations at low doping, shifting the critical doping to 0.03 for  $t'/t = -0.2$ . This is a genuine effect of the FN method, since, within the pure variational approach, though the spin-spin correlations are suppressed with respect to the case of  $t' = 0$ , the values of the critical doping for these two cases are very similar. Most importantly, the presence of a finite value of the next-nearest-neighbor hopping has dramatic effects on the superconducting properties. At small doping, i.e.,  $\delta \lesssim 0.1$  there is a sizable suppression of the electronic pairing, possibly pointing toward a metallic phase in the slightly doped regime, as previously suggested by using improved Monte Carlo techniques [166]. Moreover, for  $0.1 \lesssim \delta \lesssim 0.4$ , though small lattices seem to indicate an increasing of superconductivity compared to the pure  $t-J$  model, larger clusters show huge size effects that strongly renormalize the pairing correlations at large distance. However, for the value of  $t'$  considered in this work, we are rather confident that superconducting off-diagonal long-range order takes place in a considerable hole region. In any case, the huge renormalization of the electronic pairing for  $\delta \sim 0.3$ , together with the fact that the FN results are very different from the VMC ones based on a wave function containing pairing (and magnetic order at low doping), is pointing towards the

possibility to the existence of a non-superconducting phase (with magnetic fluxes and/or charge order) that could be eventually stabilized by further increasing the ratio  $t'/t$ .

# Conclusions and perspectives

The variational approach, based upon the definition of a proper trial wave function, is certainly one of the most powerful and general methods for studying fundamental problems in several fields of Physics. This approach allows to obtain fundamental and sometimes surprising results, as well as predictions for new phenomena. In particular, among many different applications, we would like to mention the cases of the fractional quantum Hall effect explained by the Laughlin wave function and the elegant description of superconductivity by Bardeen, Cooper, and Schrieffer in 1957. The most important aspect of this approach is to give an immediate and straightforward description of the physical problem, by allowing to clarify the most relevant effects. Sometimes, a good variational ansatz, though approximate, is even better than knowing the exact solution, since the latter one can be so complicated that it is very hard to handle and to be interpreted, like for instance the Bethe ansatz solution of the Hubbard model in one dimension.

On the other hand, within the variational approach, correlation functions can be generally computed by means of Monte Carlo techniques, that allow one to study very large systems and give the possibility to obtain accurate phase diagrams. The limitation of Monte Carlo approaches is given by the computer memory and the computational time. In fact, the quantum Monte Carlo algorithms, that are continuously developing even in the very recent years, scale at most with the third power of the system size, making possible efficient calculations on rather large clusters.

In analogy with the standard BCS theory, the search of a particularly accurate variational wave functions is extremely important to address the (still open) problems raised by the recent discovery of high-temperature superconductors (HTSC). Of course in the case of HTSC there are much more complications with respect to the conventional superconductors, due to the competition of many different energy

scales. At present, the state of the art on the study of the  $t-J$  model by the variational approach is given by the Resonating Valence Bond (RVB) wave function and its generalization to the case containing flux phases or charge-density waves. Most calculations have been done taking non-magnetic states, even though they are usually considered in relation to the underdoped and optimally doped regimes. One of the great successes of the RVB states was the prediction (before the experimental evidence) of the d-wave symmetry of the pairing function. However, they still present some problems, because they are not able to describe the correct magnetic properties close to the insulating regime at half filling. Indeed, until now, many attempts have been done, but all of them contained some drawback, like for instance a wrong spin-wave spectrum.

In this thesis, we introduced a new variational wave function that provides a much better approximation than all the previous ones, allowing us to tackle in a very accurate way a series of open problems. By means of our new variational wave function, it is possible to obtain the correct magnetic properties at low doping: a very accurate estimation of the antiferromagnetic moment at half filling, a very accurate estimation of the spin velocity, and the correct behavior of the spin-spin structure factor, implying a correct spin-wave spectrum. Therefore, this state gives us the possibility to obtain the (so far) most accurate results at low doping. The fundamental ingredients in our trial wave function are the *long-range* spin Jastrow factor and an uncorrelated state containing both magnetism and superconductivity. In contrast to the previous attempts, where the Jastrow factor was either missing or, at most, parallel to the axis of the magnetization, by using very accurate numerical simulations, we have been able to show that the Jastrow factor must be orthogonal to this axis in order to generate the correct quantum fluctuations and reproduce the exact gapless behavior of the spin waves.

The impressive accuracy of our wave function at low doping allows us to address different aspects of the phase diagram of the  $t-J$  model. In particular, we considered the problem of the possible emergence of a phase separation in the physical regime for HTSC, i.e., for  $J/t \sim 0.4$ . This issue is particularly important for understanding the actual mechanism that leads to electronic pairing and it was intensively discussed in the last 10 years. We found that the  $t-J$  model does not phase-separate for  $J/t \lesssim 0.7$ , giving a strong indication of the validity of the RVB description as the origin of superconductivity. Moreover, we find

that, by approaching half filling, the compressibility stays finite, suggesting that, close to the Mott insulator, holes form hole pockets around the nodal points, i.e.,  $q = (\pm\pi/2, \pm\pi/2)$ , and behave as spinless fermions.

In the second part of the present thesis, it was possible to address the magnetic and superconducting properties, considering also the effect of a further second-neighbor hopping  $t'$ , in order to understand whether this extra coupling constant can allow a connection between the microscopic model and *hole-doped* cuprate materials. Indeed, we have found that the simple  $t$ - $J$  model is not adequate to reproduce the phase diagram of the HTSC materials, and more ingredients have to be considered. Indeed, there is a very large region, close to half filling, with a coexistence of superconductivity and antiferromagnetism that strongly contrasts with the experimental observation. In this respect, without invoking the relevance of disorder effects, the presence of a finite  $t'$  could help to have a closer contact with hole-doped materials. In fact, the presence of a second-neighbor hopping dramatically shrinks the antiferromagnetic region, by renormalizing also the pairing correlations. These results suggest a possible non-superconducting phase close to the Mott insulator. Moreover, we do not find a sizable enhancement of the electron pairing by increasing the ratio  $t'/t$ . This could be in contradiction with the empirical relation between  $t'/t$  and the value of  $T_c$ , that has been recently put forward. However, we have to remark that we only considered ground-state properties, without a direct calculation of  $T_c$  and, in a strongly-correlated system, the relation between the critical temperature and the pairing correlations can be highly non trivial. On the other hand, it is possible that the second-neighbor hopping term deteriorates the accuracy of the variational wave function, and the presence of a finite (and large)  $t'$  could eventually stabilize competing phases with modulation in the charge distribution and/or a magnetic flux through the plaquettes. Also in this case, the relevance of this exotic phase on the actual critical temperature is not clear.

Finally, work is in progress to consider *electron-doped* cuprates, i.e., by changing the sign of  $t'$  with respect to the *hole-doped* case and the effect of a further frustrating super-exchange term  $J_2$ . The latter ingredient, even if it is not probably relevant for HTSC, can be very useful to clarify the role of the antiferromagnetic long-range order to establish pairing between electrons. Preliminary results clearly indicate that  $t'$  leads to an enhancement of the antiferromagnetic order at

low doping, which is in agreement with the experimental outcome.

# Appendix A

## Pfaffian wave function

### A.1 Definition and properties of the Pfaffian

The Pfaffian is

$$Pf[A] = \mathcal{A}[a_{1,2}a_{3,4}a_{5,6} \dots a_{N-1,N}] \quad (\text{A.1})$$

where  $\mathcal{A}$  is the antisymmetrization operator, the result is normalized such that every equivalent term occurs only once, and  $a_{i,j} = -a_{j,i}$ . For the case where  $N = 4$  this becomes

$$Pf[A] = a_{1,2}a_{3,4} - a_{1,3}a_{2,4} + a_{1,4}a_{2,3}. \quad (\text{A.2})$$

The Pfaffian is zero if  $N$  is odd and has  $(N - 1)!!$  terms otherwise.

The Pfaffian can be constructed recursively as

$$Pf[A] = \sum_{N-1 \text{ cyclic permutations of } 2-N} a_{12} \mathcal{A}[a_{3,4}a_{5,6} \dots a_{N-1,N}], \quad (\text{A.3})$$

which we will rewrite as

$$Pf[A] \equiv \sum_{j=2}^N a_{1,j} P_c(a_{1,j}). \quad (\text{A.4})$$

Here  $P_c(a_{1,j})$  is defined to be the Pfaffian cofactor of  $a_{1,j}$ , and since there are an odd number of indices in the cyclic exchange, the sign is positive. For  $N = 4$  it becomes

$$a_{1,2}a_{3,4} + a_{1,3}a_{4,2} + a_{1,4}a_{2,3} \quad (\text{A.5})$$

and using the fact that  $a_{4,2} = -a_{2,4}$ , we will obtain the Eq. (A.2). The case with  $N = 6$  gives a slightly more complicated example with the Pfaffian written as

$$a_{1,2}\mathcal{A}[a_{3,4}a_{5,6}] + a_{1,3}\mathcal{A}[a_{4,5}a_{6,2}] + a_{1,4}\mathcal{A}[a_{5,6}a_{2,3}] + a_{1,5}\mathcal{A}[a_{6,2}a_{3,4}] + a_{1,6}\mathcal{A}[a_{2,3}a_{4,5}] \quad (\text{A.6})$$

which applying the Eq. (A.2) gives all the 15 terms.

In general, given a skew-symmetric matrix  $A$

$$\begin{pmatrix} 0 & a_{1,2} & a_{1,3} & a_{1,4} \\ -a_{1,2} & 0 & a_{2,3} & a_{2,4} \\ -a_{1,3} & -a_{2,3} & 0 & a_{3,4} \\ -a_{1,4} & -a_{2,4} & -a_{3,4} & 0 \end{pmatrix},$$

the Pfaffian of this matrix is defined to be Eq. (A.1) and as one can see, the determinant of  $A$  is the square of the Pfaffian.

## A.2 Variational Monte Carlo implementation of the Pfaffian wave function

We have seen in Chapter 3, that the mean-field Hamiltonian (3.21) is quadratic in the fermionic operators and can be easily diagonalized in real space. Its ground state has the general form:

$$|\Psi_{MF}\rangle = \exp\left(\frac{1}{2} \sum_{i,j,\sigma_i,\sigma_j} f_{i,j}^{\sigma_i,\sigma_j} c_{i,\sigma_i}^\dagger c_{j,\sigma_j}^\dagger\right) |0\rangle, \quad (\text{A.7})$$

the pairing function  $f_{ij}^{\sigma_i\sigma_j}$  being an antisymmetric  $4L \times 4L$  matrix, i.e.  $f_{i,j}^{\sigma_i,\sigma_j} = -f_{j,i}^{\sigma_j,\sigma_i}$ . Notice that in the case of the standard BCS Hamiltonian, with  $\Delta_{AF} = 0$  or even with  $\Delta_{AF}$  along  $z$ , we have that  $f_{i,j}^{\uparrow,\uparrow} = f_{i,j}^{\downarrow,\downarrow} = 0$ , while in presence of magnetic field in the  $x-y$  plane the pairing function acquires non-zero contributions also in this triplet channel. The technical difficulty when dealing with such

## A.2 Variational Monte Carlo implementation of the Pfaffian wave function 13

a state is that, given a generic configuration with definite  $z$ -component of the spin  $|x\rangle = c_{i_1, \sigma_1}^\dagger \cdots c_{i_N, \sigma_N}^\dagger |0\rangle$ , we have that:

$$\langle x | \Psi_{MF} \rangle = Pf[F] = Pf \begin{pmatrix} f_{ij}^{\uparrow, \uparrow} & f_{ij}^{\uparrow, \downarrow} \\ f_{ij}^{\downarrow, \uparrow} & f_{ij}^{\downarrow, \downarrow} \end{pmatrix}, \quad (\text{A.8})$$

where  $Pf[F]$  is the Pfaffian of the pairing function. It should be noticed that, whenever  $f_{i,j}^{\uparrow, \uparrow} = f_{i,j}^{\downarrow, \downarrow} = 0$ , the usual form of  $\langle x | \Psi_{MF} \rangle$  written in terms of a determinant is recovered.

Let us enter, in this section, in more details giving a short proof of the statement given above. First of all we emphasize that  $|\Psi_{MF}\rangle$  has neither a fixed number of particles due to the presence of the *BCS* pairing, nor a fixed total  $S^z$  due to the  $x$ - $y$  plane magnetic order.

When we consider the projector onto the state of  $N$  particles, we obtain

$$|\Psi_{MF}\rangle = \left\{ \frac{1}{2} \sum_{i,j,\sigma_i,\sigma_j} f_{i,j}^{\sigma_i,\sigma_j} c_{i,\sigma_i}^\dagger c_{j,\sigma_j}^\dagger \right\}^{N/2} |0\rangle, \quad (\text{A.9})$$

then, expanding the product we have

$$|\Psi_{MF}\rangle = \sum_{(R_1, \dots, R_{N/2})(R'_1, \dots, R'_{N/2})} \left\{ f_{(R_1, R'_1)} \cdots f_{(R_{N/2}, R'_{N/2})} \right\} c_{R_1}^\dagger c_{R'_1}^\dagger \cdots c_{R_{N/2}}^\dagger c_{R'_{N/2}}^\dagger |0\rangle \quad (\text{A.10})$$

where we used the notations  $R_i = (x_i, \sigma_i)$ . Then the projection on the basis state  $\langle x | = \langle 0 | c_{R_1} \cdots c_{R_N}$  is given by:

$$\langle x | \Psi_{MF} \rangle = \sum_{\mathcal{P}} \left\{ f_{(\mathcal{P}_{R_1}, \mathcal{P}_{R_2})} \cdots f_{(\mathcal{P}_{R_{N-1}}, \mathcal{P}_{R_N})} \right\} (-1)^{\text{sign}(\mathcal{P})} \quad (\text{A.11})$$

where the sum is done on all possible permutation  $\mathcal{P}$ , and  $\mathcal{P}(R_i) = R_k$ , where  $k = \mathcal{P}(i)$ . At this point, defining the following skew matrix  $F_{ij} = f_{R_i, R_j}$ , we can note that

$$\sum_{\mathcal{P}} \left\{ f_{(\mathcal{P}_{R_1}, \mathcal{P}_{R_2})} \cdots f_{(\mathcal{P}_{R_{N-1}}, \mathcal{P}_{R_N})} \right\} (-1)^{\text{sign}(\mathcal{P})} = Pf[F] \quad (\text{A.12})$$

and this concludes the proof.

In conclusion, we find that the wave function projected on a basis state  $|x\rangle$ , when BCS pairing and magnetization on the  $x - y$  plane are present, is the Pfaffian of the anti-symmetrized matrix  $F$ :

$$\langle x|\Psi_{MF}\rangle = Pf[F] = Pf\left(\begin{array}{cc} f_{ij}^{\uparrow,\uparrow} & f_{ij}^{\uparrow,\downarrow} \\ f_{ij}^{\downarrow,\uparrow} & f_{ij}^{\downarrow,\downarrow} \end{array}\right) \quad (\text{A.13})$$

where  $Pf[F]$  denote the Pfaffian of the matrix  $F$ . Using this last relation, the wave function can now be evaluated numerically using a Monte Carlo procedure with Pfaffian updates, as introduced in Ref. [133].

In the particular case where  $f_{i,j}^{\uparrow,\uparrow} = f_{i,j}^{\downarrow,\downarrow} = 0$  (this happen if in the mean field Hamiltonian is present just the BCS interaction, or just the antiferromagnetic term or both BCS and the  $z$  plane antiferromagnetic terms), the Pfaffian reduces to a simple determinant. In fact, the matrix  $F$  reduces to diagonal blocks:

$$F = \left(\begin{array}{cc} 0 & B \\ -B^T & 0 \end{array}\right) \Rightarrow Pf[F] = \det(B), \quad (\text{A.14})$$

where the matrix elements of  $B$  are the  $f_{i,j}^{\uparrow,\downarrow}$  of the equation (A.7). We emphasize that the matrix that we need to update in the Pfaffian Monte Carlo simulations has linear sizes twice larger than in the usual calculations with determinants. In conclusion, the Pfaffian Monte Carlo procedure is nothing else but an extension of the usual variational wave function method, which allows to treat generally every order parameter contained in the mean field Hamiltonian (3.21) in which we are interested.

# Bibliography

- [1] J.G. Bednorz and K.A. Muller. *Z. Phys. B*, **64**:189, (1986).
- [2] J. Bardeen, L.N. Cooper, and J.R. Schrieffer. *Phys. Rev.*, **108**:1175, (1957).
- [3] P. Nozieres. *Theory of Interacting Fermi Systems*, Addison-Wesley (*Advanced book classics*).
- [4] C. M. Varma, P. B. Littlewood, S. Schmitt-Rink, E. Abrahams, and A. E. Ruckenstein. *Phys. Rev. Lett.*, **63**:1996, (1989).
- [5] V.J. Emery and S.A. Kivelson. *Physica C*, **209**:597, (1993).
- [6] V.J. Emery and S.A. Kivelson. *Nature*, **374**:434, (1995).
- [7] M. Lugas, L. Spanu, F. Becca, and S. Sorella. *Phys. Rev. B*, **74**:165122, (2006).
- [8] L. Spanu, M. Lugas, F. Becca, and S. Sorella. *arXiv:0709.2850v1* (*submitted to Phys. Rev. B*).
- [9] M. Gurvitch and A. T. Fiory. *Phys. Rev. Lett.*, **59**:1337, (1987).
- [10] E. Dagotto. *Rev. Mod. Phys.*, **66**:763, (1994).
- [11] P.A. Lee, N. Nagaosa, and X-G. Wen. *Rev. Mod. Phys.*, **78**:17, (2006).
- [12] P.W. Anderson. *Phys. Rev.*, **115**:2, (1959).
- [13] H. Takagi, S. Uchida, and Y. Tokura. *Phys. Rev. Lett.*, **62**:1197, (1989).

- [14] Z.-X. Shen, D. S. Dessau, B. O. Wells, D. M. King, W. E. Spicer, A. J. Arko, D. Marshall, L. W. Lombardo, A. Kapitulnik, P. Dickinson, S. Doniach, J. DiCarlo, T. Loeser, and C. H. Park. *Phys. Rev. Lett.*, **70**:1553, (1993).
- [15] H. Ding, J.C. Campuzano, A.F. Bellman, T. Yokoya, M.R. Norman, M. Randeria, T. Takahashi, H. Katayama-Yoshida, T. Mochiku, K. Kadowaki, and G. Jennings. *Phys. Rev. Lett.*, **74**:2784, (1995).
- [16] D.J. Van Harlingen. *Rev. Mod. Phys.*, **67**:515, (1995).
- [17] C.C. Tsuei and J.R. Kirtley. *Rev. Mod. Phys.*, **72**:969, (2000).
- [18] A.G. Loeser, Z.-X. Shen, D.S. Dessau, D.S. Marshall, C.H. Park, P. Fournier, and A. Kapitulnik. *Science*, **273**:325, (1996).
- [19] A. Damascelli, Z. Hussain, and Z.-X. Shen. *Rev. Mod. Phys.*, **75**:473, (2003).
- [20] T. Timusk and B. Statt. *Rep. Prog. Phys.*, **62**:61, (1999).
- [21] D. S. Marshall, D. S. Dessau, A. G. Loeser, C-H. Park, A. Y. Matsuura, J. N. Eckstein, I. Bozovic, P. Fournier, A. Kapitulnik, W. E. Spicer, and Z.-X. Shen. *Phys. Rev. Lett.*, **76**:4841, (1996).
- [22] H. Ding, T. Yokoya, J.C. Campuzano, T. Takahashi, M. Randeria, M.R. Norman, T. Mochiku, K. Kadowaki, and J. Giapintzakis. *Nature*, **382**:51, (1996).
- [23] M.R. Norman, H. Ding, M. Randeria, J.C. Campuzano, T. Yokoya, T. Takeuchi, T. Takahashi, T. Mochiku, K. Kadowaki, P. Guptasarma, and D.G. Hinks. *Nature*, **392**:157, (1998).
- [24] N.P. Ong, Y. Wang, S. Ono, Y. Ando, and S. Uchida. *Ann. Phys.*, **13**:9, (2004).
- [25] Y. Wang, S. Ono, Y. Onose, G. Gu, Y. Ando, Y. Tokura, S. Uchida, and N.P. Ong. *Science*, **299**:86, (2003).
- [26] S.A. Kivelson, E.Fradkin, V. Oganessian, I.P. Bindloss, J.M. Tranquada, A. Kapitulnik, and C. Howald. *Rev. Mod. Phys.*, **75**:1201, (2003).

- [27] J.M. Tranquada. *cond-mat/0512115*.
- [28] E. Dagotto. *Science*, **309**:257, (2005).
- [29] J.C. Campuzano, M.R. Norman, and M. Randeria. *cond-mat/0209476*.
- [30] G. Deutscher. *Rev. Mod. Phys.*, **77**:109, (2005).
- [31] R. Khasanov, A. Shengelaya, A. Maisuradze, F. La Mattina, A. Busmann-Holder, H. Keller, and K. A. Muller. *Phys. Rev. Lett.*, **98**:057007, (2007).
- [32] D.L. Feng, D.H. Lu, K.M. Shen, C. Kim, H. Eisaki, A. Damascelli, R. Yoshizaki, J. i. Shimoyama, K. Kishio, G.D. Gu, A. Andrus, J. O'Donnell, J.N. Eckstein, and Z.-X. Shen. *Science*, **289**:277, (2000).
- [33] H. Ding, J.R. Engelbrecht, Z. Wang, J.C. Campuzano, S.-C. Wang, H.-B. Yang, R. Rogan, T. Takahashi, K. Kadowaki, and D.G. Hinks. *Phys. Rev. Lett.*, **87**:227001, (2001).
- [34] D. Le Boeuf, J. Levallois, J.B. Bonnemaïson, R. Liang, D.A. Bonn, W.N. Hardy, N. Doiron-Leyraud, C. Proust, and L. Taillefer. *Nature*, **447**:565, (2007).
- [35] W.E. Hudson, S.H. Pan, A.K. Gupta, K.-W. Ng, and J.C. Davis. *Science*, **285**:88, (1999).
- [36] A. Yazdani, C.M. Howald, C.P. Lutz, A. Kapitulnik, and D.M. Eigler. *Phys. Rev. Lett.*, **83**:176, (1999).
- [37] S.H. Pan, W.E. Hudson, K.M. Lang, H. Eisaki, S.Uchida, and J.C. Davis. *Nature*, **403**:746, (2003).
- [38] I. Maggio-Aprile, Ch. Renner, A. Erb, E. Walker, and O. Fischer. *Phys. Rev. Lett.*, **75**:2754, (1995).
- [39] Ch. Renner, B. Revaz, A. Erb, K. Kadowaki, I. Aprile-Maggio, and O. Fischer. *Phys. Rev. Lett.*, **80**:3606, (1998).
- [40] S.H. Pan, E.W. Hudson, A.K. Gupta, K.-W. Ng, H. Eisaki, S. Uchida, and J.C. Davis. *Phys. Rev. Lett.*, **85**:1536, (2000).

- [41] M. Vershinin, S. Misra, S. Ono, Y. Abe, Y. Ando, and A. Yazdani. *Science*, **303**:1995, (2004).
- [42] T. Hanaguri, C. Lupien, Y. Kohsaka, D.-H. Lee, M. Azuma, M. Takano, H. Takagi, and J.C. Davis. *Nature*, **430**:1001, (2004).
- [43] K. McElroy, D.-H. Lee, J.E. Hoffman, K.M. Lang, J. Lee, E.W. Hudson, H. Eisaki, S. Uchida, and J.C. Davis. *Phys. Rev. Lett.*, **94**:197005, (2005).
- [44] V.J. Emery, S.A. Kivelson, and H.Q. Lin. *Phys. Rev. Lett.*, **64**:475, (1990).
- [45] C. Di Castro, C. Castellani, and M. Grilli. *Physica Scripta*, **T45**:81, (1992).
- [46] S. Pei, D.G. Hinks, L. Soderholm, B. Morosin, J.E. Schirber, E.L. Venturini, J.D. Jorgensen, B. Dabrowski, and D.S. Ginley. *Phys. Rev. B*, **38**:11337, (1988).
- [47] P.C. Hammel, A. P. Reyes, Z. Fisk, M. Takigawa, J. D. Thompson, R. H. Heffner, S-W. Cheong, and J. E. Schirber. *Phys. Rev. B*, **42**:6781, (1990).
- [48] K. Yamada, C.H. Lee, K. Kurahashi, J. Wada, S. Wakimoto, S. Ueki, H. Kimura, Y. Endoh, S. Hosoya, G. Shirane, R.J. Birgeneau, M. Greven, M.A. Kastner, and Y.J. Kim. *Phys. Rev. B*, **57**:6165, (1998).
- [49] T. Niemoeller, N. Ichikawa, T. Frello, H. Huennefeld, N. H. Andersen, S. Uchida, J. R. Schneider, and J. M. Tranquada. *cond-mat/9904383*.
- [50] S.R. White and D.J. Scalapino. *Phys. Rev. Lett.*, **81**:3227, (1998).
- [51] J. Hubbard. *Proc. Roy. Soc. London A*, **276**:238, (1963).
- [52] M.C. Gutzwiller. *Phys. Rev. Lett.*, **10** (5):159, (1963).
- [53] J. Kanamori. *Progr. Theor. Phys.*, **30**:275, (1963).
- [54] E.H. Lieb and F.Y. Wu. *Phys. Rev. Lett.*, **20**:1445, (1968).
- [55] H.J. Schulz. *Phys. Rev. Lett.*, **64**:1445, (1990).
- [56] T.A. Maier, M. Jarrell, T.C. Schulthess, P.R.C. Kent, and J.B. White. *Phys. Rev. Lett.*, **95**:237001, (2005).

- [57] P.W. Anderson. *Science*, **235**:1196, (1987).
- [58] F.C. Zhang and T.M. Rice. *Phys. Rev. B*, **37**:3759, (1988).
- [59] J.R. Schrieffer and P.A. Wolff. *Phys. Rev.*, **149**:491, (1966).
- [60] J. D. Reger and A. P. Young. *Phys. Rev. B*, **37**:5978, (1988).
- [61] S. Liang, B. Doucot, and P.W. Anderson. *Phys. Rev. Lett.*, **61**:365, (1988).
- [62] C.L. Kane, P.A. Lee, and N. Read. *Phys. Rev. B*, **39**:6880, (1989).
- [63] C. Gros and M.D. Johnson. *Phys. Rev. B*, **40**:9423, (1989).
- [64] G. Kotliar and J. Liu. *Phys. Rev. B*, **38**:5142, (1988).
- [65] F.C. Zhang, C. Gros, T.M. Rice, and H. Shiba. *Supercond. Sci. Technol.*, **1**:36, (1988).
- [66] Y. Hasegawa, Y. Suzumura, and H. Fukuyama. *J. Phys. Soc. Jpn.*, **57**:2768, (1988).
- [67] H. Yokoyama and H. Shiba. *J. Phys. Soc. Jpn.*, **57**:2482, (1988).
- [68] C. Gros. *Phys. Rev. B*, **38**:931, (1988).
- [69] P.W. Anderson. *cond-mat/0406038*.
- [70] F.C. Zhang, H.-X. Huang, and Y.-Q. Li. *Phys. Rev. B*, **71**:184514, (2005).
- [71] D. Poilblanc. *Phys. Rev. B*, **72**:060508, (2005).
- [72] S Zhou, C. Li, and Z. Wang. *Phys. Rev. B*, **73**:060501, (2006).
- [73] A.Himeda and M. Ogata. *Phys. Rev. B*, **60**:9935, (1999).
- [74] F.C. Zhang, G.J. Chen, R. Joynt, and C. Gros. *Phys. Rev. B*, **42**:2662, (1990).
- [75] T. Giamarchi and C. Lhullier. *Phys. Rev. B*, **43**:12943, (1991).
- [76] C.P. Chou, C.T. Shih, T.C. Chen, and T.K. Lee. *Phys. Rev. B*, **70**:220502, (2004).

- [77] M. Ogata. and A. Himeda. *J. Phys. Soc. Jpn.*, **72**:374, (2003).
- [78] D.A. Ivanov. *Phys. Rev. B*, **70**:104503, (2004).
- [79] M. Ogata, H. Tsuchiura, Y. Tanaka, and S. Kashiwaya. *J. Phys. Soc. Jpn.*, **68**:2510, (1999).
- [80] M. Ogata, H. Tsuchiura, Y. Tanaka, and S. Kashiwaya. *J. Phys. Soc. Jpn.*, **66**:3367, (1997).
- [81] M. Capello, F. Becca, M. Fabrizio, S. Sorella, and E. Tosatti. *Phys. Rev. Lett.*, **94**:026406, (2005).
- [82] J. Schmailian, J.Liu, and N. Trivedi. *Phys. Rev. Lett.*, **94**:127003, (2005).
- [83] Y. Tanaka, T. Watanabe, H. Yokoyama, and J. Inoue. *J. Phys. Soc. Jpn.*, **75**:074707, (2006).
- [84] C.S. Hellberg and E.J. Mele. *Phys. Rev. Lett.*, **67**:2080, (1991).
- [85] R. Valenti and C. Gros. *Phys. Rev. Lett.*, **68**:2402, (1992).
- [86] R. Jastrow. *Phys. Rev.*, **98**:1479, (1955).
- [87] B. Sutherland. *Phys. Rev. A*, **4**:2019, (1971).
- [88] F.D.M. Haldane. *Phys. Rev. Lett.*, **60**:635, (1988).
- [89] B.S. Shastry. *Phys. Rev. Lett.*, **60**:639, (1988).
- [90] W.L. McMillan. *Phys. Rev.*, **138**:A442, (1965).
- [91] L. Reatto and G.V. Chester. *Phys. Rev.*, **155**:88, (1967).
- [92] G. Gaglione, G.L. Masserini, and L. Reatto. *Phys. Rev. B*, **22**:1237, (1980).
- [93] P.A. Whitlock, D.M. Ceperley, G.V. Chester, and M.H. Kalos. *Phys. Rev. B*, **19**:5598, 1979.
- [94] T. MacFarland, S.A. Vitiello, L. Reatto, G.V. Chester, and M.H. Kalos. *Phys. Rev. B*, **50**:13577, (1994).

- [95] E. Dagotto, S. Yunoki, and S. Sorella. *Phys. Rev. Lett.*, **94**:037001, (2005).
- [96] S. Sorella, G.B. Martins, F. Becca, C. Gazza, L. Capriotti, A. Parola, and E. Dagotto. *Phys. Rev. Lett.*, **88**:117002, (2002).
- [97] E. Manousakis. *Rev. Mod. Phys.*, **63**:1, (1991).
- [98] Z. Liu and E. Manousakis. *Phys. Rev. B*, **40**:11437, (1989).
- [99] F. Franjic and S. Sorella. *Prog. Theor. Phys.*, **97**:399, (1997).
- [100] N. Metropolis, A. Rosenbluth, M. Rosenbluth, A. Teller, and E. Teller. *J. Chem. Phys.*, **21**:1087, (1953).
- [101] S. Sorella. *Phys. Rev. B*, **64**:024512, (2001).
- [102] S. Sorella. *Phys. Rev. B*, **72**:241103, (2005).
- [103] N. Trivedi and D.M. Ceperley. *Phys. Rev. B*, **41**:4552, (1990).
- [104] M. Calandra and S. Sorella. *Phys. Rev. B*, **57**:11446, (1998).
- [105] D.F.B. ten Haaf, H.J.M. van Bommel, J.M.J. van Leeuwen, W. van Saarloos, and D.M. Ceperley. *Phys. Rev. B*, **51**:13039, (1995).
- [106] S. Sorella. *cond-mat/0201388*.
- [107] S. Sorella and L. Capriotti. *Phys. Rev. B*, **61**:2599, (2000).
- [108] S.A. Kivelson, E.W. Carlson, V.J. Emery, and D. Orgad. *cond-mat/0206217*.
- [109] J.D. Axe, Y. Nakamura, J.M. Tranquada, B.J. Sternlieb, and S. Uchida. *Nature*, **375**:561, (1995).
- [110] N. Ichikawa, A.R. Moodenbaugh, Y. Nakamura, J.M. Tranquada, J.D. Axe, and S. Uchida. *Phys. Rev. Lett.*, **78**:338, (1997).
- [111] K. Machida. *Physica C*, **158**:192, (1989).
- [112] H. Nakanishi, M. Kato, K. Machida, and M. Fujita. *J. Phys. Soc. Jpn.*, **59**:1047, (1990).

- [113] D. Poilblanc and T.M. Rice. *Phys. Rev. B*, **39**:9749, (1989).
- [114] H.J. Schulz. *Phys. Rev. Lett.*, **64**:1445, (1990).
- [115] H. Yokoyama and H. Shiba. *J. Phys. Soc. Jpn.*, **56**:1490, (1987).
- [116] H. Yokoyama and H. Shiba. *J. Phys. Soc. Jpn.*, **56**:3582, (1987).
- [117] M.U. Luchini, W.O. Putikka, and T.M. Rice. *Phys. Rev. Lett.*, **68**:538, (1992).
- [118] C.S. Hellberg and E. Manousakis. *Phys. Rev. Lett.*, **78**:4609, (1997).
- [119] M. Kohno. *Phys. Rev. B*, **55**:1435, (1997).
- [120] Y.C. Chen, C.T. Shih, and T.K. Lee. *Phys. Rev. B*, **57**:627, (1998).
- [121] M. Calandra, F. Becca, and S. Sorella. *Phys. Rev. Lett.*, **81**:81, (1998).
- [122] W.O. Putikka and M.U. Luchini. *Phys. Rev. B*, **62**:1684, (2000).
- [123] C.S. Hellberg and E. Manousakis. *Phys. Rev. B*, **70**:11787, (2000).
- [124] S.R. White and D.J. Scalapino. *Phys. Rev. B*, **61**:6320, (2000).
- [125] F. Becca, L. Capriotti, and S. Sorella. *Phys. Rev. Lett.*, **87**:167005, (2001).
- [126] S.R. White and D.J. Scalapino. *Phys. Rev. Lett.*, **80**:1272, (1998).
- [127] F. Becca, M. Capone, and S. Sorella. *Phys. Rev. B*, **62**:12700, (2000).
- [128] A. Paramekanti, M. Randeria, and N. Trivedi. *Phys. Rev. Lett.*, **87**:217002, (2001).
- [129] D.A. Ivanov, P.A. Lee, and X.-G. Wen. *Phys. Rev. Lett.*, **84**:3958, (2000).
- [130] E. Plekhanov, F. Becca, and S. Sorella. *Phys. Rev. B*, **71**:064511, (2005).
- [131] E.S. Heeb and T.M. Rice. *Europhys. Lett.*, **27**:673, (1994).
- [132] F. Franjic and S. Sorella. *Mod. Phys. Lett. B*, **10**:873, (1996).

- [133] J.P. Bouchaud, A. Georges, and C. Lhuillier. *J. de Physique*, **49**:553, (1988).
- [134] J. Carlson, S.-Y. Chang, V.R. Pandharipande, and K.E. Schmidt. *Phys. Rev. Lett.*, **91**:050401, (2003).
- [135] M. Bajdich, L. Mitas G. Drobny, L.K. Wagner, and K.E. Schmidt. *Phys. Rev. Lett.*, **96**:130201, (2006).
- [136] C. Weber, A. Laeuchli, F. Mila, and T. Giamarchi. *Phys. Rev. B*, **73**:014519, (2006).
- [137] A.W. Sandvik. *Phys. Rev. B*, **56**:11678, (1997).
- [138] N. Furukawa and M. Imada. *J. Phys. Soc. Jpn.*, **62**:2557, (1993).
- [139] F.F. Assaad and M. Imada. *Phys. Rev. Lett.*, **76**:3176, (1996).
- [140] G. Kotliar, S. Murthy, and M.J. Rozenberg. *Phys. Rev. Lett.*, **89**:046401, (2002).
- [141] D. Poilblanc. *Phys. Rev. B*, **52**:9201, (1995).
- [142] C. Weber, D. Poilblanc, S. Capponi, F. Mila, and C. Jaudet. *Phys. Rev. B*, **74**:104506, (2006).
- [143] M. Raczkowski, R. Fresard, and A.M. Oles. *Phys. Rev. B*, **73**:174525, (2006).
- [144] A. Lanzara, P.V. Bogdanov, X.J. Zhou, S.A. Kellar, D.L. Feng, E.D. Lu, T. Yoshida, H. Eisaki, A. Fujimori, K. Kishio, J.-I. Shimoyama, T. Noda, S. Uchida, Z. Hussain, and Z.-X. Shen. *Nature (London)*, **412**:510, (2001).
- [145] G.-H. Gweon, S.Y. Zhou, M.C. Watson, T. Sasagawa, H. Takagi, and A. Lanzara. *Phys. Rev. Lett.*, **97**:227001, (2006).
- [146] Th. Maier, M. Jarrell, T. Pruschke, and M.H. Hettler. *Rev. Mod. Phys.*, **77**:1027, (2005).
- [147] D. Eichenberger and D. Baeriswyl. *arXiv:0708.2795 (unpublished)*.

- [148] P.W. Anderson, P.A. Lee, M. Randeria, T.M. Rice, N. Trivedi, and F.C. Zhang. *J. Phys.: Condensed Matter*, **24**:R755, (2004).
- [149] C. Gros. *Phys. Rev. B*, **42**:6835, (1990).
- [150] Y. Sidis, C. Ulrich, P. Bourges, C. Bernhard, C. Niedermayer, L.P. Regnault, N.H. Andersen, and B. Keimer. *Phys. Rev. Lett.*, **86**:4100, (2001).
- [151] J.A. Hodges, Y. Sidis, P. Bourges, I. Mirebeau, M. Hennion, and X. Chaud. *Phys. Rev. B*, **66**:020501(R), (2002).
- [152] H.A. Mook, P. Dai, S.M. Hayden, A. Hiess, J.W. Lynn, S.-H. Lee, and F. Dogan. *Phys. Rev. B*, **66**:144513, (2002).
- [153] E. Pavarini, I. Dasgupta, T. Saha-Dasgupta, O. Jepsen, , and O.K. Andersen. *Phys. Rev. Lett.*, **87**:047003, (2001).
- [154] K. Tanaka, T. Yoshida, A. Fujimori, D.H. Lu, Z.-X. Shen, X.-J. Zhou, H. Eisaki, Z. Hussain, S. Uchida, Y. Aiura, K. Ono, T. Sugaya, T. Mizuno, and I. Terasaki. *Phys. Rev. B*, **70**:092503, (2004).
- [155] T. Tohyama and S. Maekawa. *Phys. Rev. B*, **49**:3596, (1994).
- [156] S.R. White and D.J. Scalapino. *Phys. Rev. B*, **60**:753(R), (1999).
- [157] A. Himeda, T. Kato, and M. Ogata. *Phys. Rev. Lett.*, **88**:117001, (2002).
- [158] C.T. Shih, T.K. Lee, R. Eder, C.-Y. Mou, and Y.C. Chen. *Phys. Rev. Lett.*, **92**:227002, (2004).
- [159] C.T. Shih, Y.C. Chen, C.P. Chou, and T.K. Lee. *Phys. Rev. B*, **70**:220502(R), (2004).
- [160] S. Sorella. *Phys. Rev. B*, **71**:241103, (2005).
- [161] S. Yunoki and S. Sorella. *Phys. Rev. B*, **74**:014408, (2006).
- [162] D.M. Ceperley and B.J. Alder. *Phys. Rev. Lett.*, **45**:566, (1980).
- [163] A. Macridin, M. Jarrell, and Th. Maier. *Phys. Rev. B*, **74**:085104, (2006).

- 
- [164] N. Furukawa and M. Imada. *J. Phys. Soc. Jpn.*, **61**:3331, (1992).
- [165] S. Bieri and D. Ivanov. *Phys. Rev. B*, **75**:035104, (2007).
- [166] V.I. Anisimov, M.A. Korotin, I.A. Nekrasov, Z.V. Pchelkina, and S. Sorella. *Phys. Rev. B*, **66**:100502, (2002).
- [167] M. Raczkowski, M. Capello, D. Poilblanc, R. Fresard, and A.M. Oles. *arXiv:0708.0788 (unpublished)*.

